



UNIVERSITÀ DEGLI STUDI DI TRIESTE
e
UNIVERSITÀ CA' FOSCARI DI VENEZIA

XXXII CICLO DEL DOTTORATO DI RICERCA IN
CHIMICA

**Development of heterogeneous catalysts for fuel and
chemicals production**

Settore scientifico-disciplinare: CHIM/04

DOTTORANDA
CRISTINA PIZZOLITTO

COORDINATORE
PROF. BARBARA MILANI

SUPERVISORE DI TESI
PROF. MICHELA SIGNORETTO

CO-SUPERVISORE DI TESI
DOTT. FEDERICA MENEGAZZO

ANNO ACCADEMICO 2018/2019



UNIVERSITÀ DEGLI STUDI DI TRIESTE
e
UNIVERSITÀ CA' FOSCARI DI VENEZIA

XXXII CICLO DEL DOTTORATO DI RICERCA IN
CHIMICA

**Development of heterogeneous catalysts for fuel and
chemicals production**

Settore scientifico-disciplinare: **CHIM/04**

DOTTORANDA
CRISTINA PIZZOLITTO

COORDINATORE
PROF. BARBARA MILANI

SUPERVISORE DI TESI
PROF. MICHELA SIGNORETTO

CO-SUPERVISORE DI TESI
DOTT. FEDERICA MENEGAZZO

ANNO ACCADEMICO 2018/2019

Abstract

Substitution of a fossil sources-based society to renewable one is the main challenge of 21 century. This Ph.D. work is focused on the development of heterogeneous catalysts for biomass valorisation, considering both fuel and chemical production. H₂ and Levulinic acid (LA) were selected thanks to their promising properties and their production processes were investigated. The common denominator of the entire work is the study and the optimization of the most suitable catalyst for each process. The ideal catalyst for H₂ production must be robust and resistant to coke deposition. For this reason, optimisation of nickel-ceria and nickel-zirconia based catalysts was performed. In the case of LA, the best one must be sufficiently acid to direct the conversion of glucose. At the same time, it must suppress unwanted reactions such as humins formation. In this case, SBA-15, a silica mesoporous material, was properly modified introducing acid functionalities via grafting approach and by the addition of a promoter.

Considering H₂ production, it was demonstrated how support synthesis strongly influences the catalyst features and consequently, the catalytic activity. For ceria support, it was determined how the precipitation method allows obtaining a good catalyst with high surface area, a high degree of crystallinity and with a wide distribution of active phase. Moreover, these properties were successfully implemented introducing a promoter as lanthanum. It was found that lanthanum increases the redox ability of the Ni-ceria catalyst, guaranteeing high stability in ESR conditions. Moreover, these properties were widely enhanced when the lanthanum was added by co-precipitation. The effect of lanthanum was also investigated in nickel zirconia-based catalyst. In this case, its influence is completely different from the ceria case. Indeed, for zirconia, lanthanum properly modulates the acidic/basic features. Moreover, the best result was obtained with the catalyst prepared via the impregnation of the promoter on the support. Thanks to this study, it was possible to enormously implement the properties of the individual support, tuning its preparation method and introducing a promoter.

Considering LA production via hydrolysis, implementation of SBA-15 acidity was achieved with the introduction of both aluminium and sulfonic groups. It was found a new environmentally friendly and cost-effective method to graft sulfonic acid groups over silica surface and increase its Brønsted acidity. To implement the Lewis one, it was demonstrated that the addition of aluminium via evaporation-impregnation increases the number of medium and strong Lewis sites preserving

the SBA-15 morphological features. Therefore, this new material has promising properties to be used in converting more complex carbohydrate substrates.

Summary

<u>Chapter 1.</u>	<u>1</u>
1.1 Sustainable Future of Energy and Chemicals	1
1.2 Biomass as a renewable resource	3
1.3 Lignocellulosic biomass	3
1.4 H ₂ production via Ethanol Steam reforming	7
1.4.1 <i>Catalysts for H₂ production</i>	10
1.5 Levulinic acid production	13
1.5.1 <i>Catalysts for LA production</i>	15
<u>Chapter 2 . Microemulsion vs. Precipitation: Selecting the support synthesis of nickel-ceria based catalysts for ethanol steam reforming</u>	<u>19</u>
2.1 Experimental	19
2.1.1 <i>Catalyst preparation</i>	19
2.1.2 <i>Catalyst characterisations</i>	20
2.1.3 <i>Catalytic tests</i>	20
2.2 Results and Discussion	22
2.2.1 <i>Catalysts characterisations</i>	22
2.2.2 <i>Catalytic performance of Ni ceria catalysts</i>	25
2.3 Conclusions	30
<u>Chapter 3. Increase of ceria redox ability by lanthanum addition on Ni based catalysts</u>	<u>31</u>
3.1 Experimental	32
3.1.1 <i>Catalysts preparation</i>	32
3.1.2 <i>Catalyst Characterisations</i>	33
3.1.3 <i>Catalytic tests</i>	34
3.2 Results and Discussion	36
3.2.1 <i>Catalyst characterisations</i>	36
3.2.2 <i>Reactivity tests</i>	38
3.2.3 <i>Influence of lanthanum on nickel reducibility</i>	42
3.2.4 <i>Influence of lanthanum on catalyst structure</i>	43
3.3 Conclusions	47
<u>Chapter 4. Limiting Coke deactivation of Ni-ZrO₂ in ethanol steam reforming by promoting effect of lanthanum</u>	<u>48</u>
4.1 Experimental	48
4.1.1 <i>Catalyst preparation</i>	48
4.1.2 <i>Catalyst Characterisations</i>	49
4.2 Results and Discussion	51

4.2.1 <i>Catalyst characterisations</i>	51
4.2.2 <i>Catalytic tests</i>	55
4.3 Conclusions	65
<hr/>	
<u>Chapter 5. Effect of grafting solvent in the optimization of SBA-15 acidity for levulinic acid production</u>	<u>67</u>
5.1 Experimental	67
5.1.1 <i>Catalyst preparation</i>	67
5.1.2 <i>Catalyst characterisations</i>	68
5.1.3 <i>Catalytic test</i>	69
5.2 Results and discussion	70
5.2.1 <i>Catalyst characterisations</i>	70
5.2.2 <i>Reactivity tests</i>	76
5.2.3 <i>Acidic properties</i>	78
5.3 Conclusions	81
<hr/>	
<u>Chapter 6. Modification of physical-chemical and catalytic properties of SBA-15 by Al addition</u>	<u>82</u>
6.1 Experimental	82
6.1.1 <i>Catalyst preparation</i>	82
6.1.2 <i>Catalyst characterisations</i>	83
6.2 Results and discussion	85
6.2.1 <i>Influence of Alumina introduction method</i>	85
6.2.2 <i>Influence of aluminium amount</i>	89
6.2.3 <i>Reactivity</i>	95
6.2.5 <i>Incorporation of Brønsted acid sites</i>	97
6.3 Conclusions	99
<hr/>	
<u>Chapter 7. Conclusions</u>	<u>100</u>
<hr/>	
<u>Chapter 8. References</u>	<u>102</u>
<hr/>	
<u>Appendix</u>	<u>117</u>
<hr/>	
<u>A1. Supplementary information of Chapter 3</u>	<u>117</u>
<hr/>	
<u>A2. Supplementary information of Chapter 4</u>	<u>121</u>
<hr/>	
<u>Curriculum Vitae</u>	<u>122</u>
<hr/>	
<u>List of publications and conference presentations based on this thesis</u>	<u>123</u>
<hr/>	
<u>Other publications</u>	<u>125</u>

Chapter 1.

The industrial revolution brought wealth, prosperity and innovation for the society of the 19th century. From the beginning of industrialization up to now, the use of fossil sources has dominated the energy and chemical scenario covering 80 % of energy needs and 95 % of chemical feedstocks production. Despite the countless advantages, it has brought several economic, political and environmental concerns. For this reason, as reported by the International Energy Agency in the 2009 [1], the next industrial revolution will be characterised by the transition from fossil to renewable resources.

1.1 Sustainable Future of Energy and Chemicals

Due to the rising global population, the world's overall energy demand is continually growing. This increased need of energy and resources is strictly related to global warming threat since carbon dioxide (CO₂) emission has increased 53 % from 1995 to 2017, reaching a value of 33.4 GT in 2017 [2]. Indeed, the raised CO₂ level causes a surge in globally averaged temperature with disastrous consequences for the planet. Therefore, the global energy system deals with a dual challenge: the need for more energy and less carbon in atmosphere. Figure 1.1 reports CO₂ emissions divided by the principal producers' sectors. Transport and industry account for around a quarter of global anthropogenic emissions [3], while the power sector, which represents the main sector in CO₂ emissions, is the largest source of the increase in CO₂ emissions.

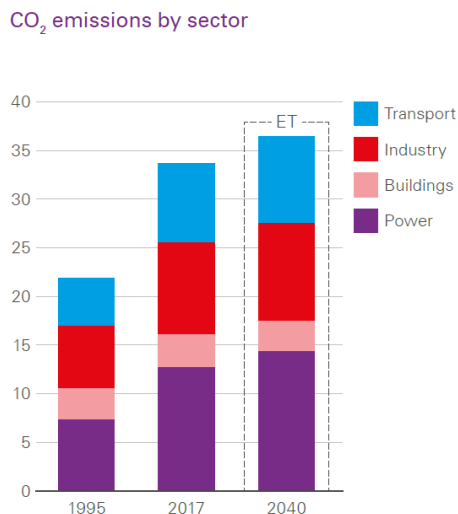


Figure 1.1. Increase of CO₂ emission divided by sectors.

This global primary energy demand is principally satisfied by exhaustible energy sources, such as coal, oil, natural gas, and nuclear [4]. All these aspects have addressed worldwide governments to promote the transition from fossil fuels to renewable alternatives, in combination with the reduction of CO₂ emission. For this reason, multiple accords were signed such as the Kyoto Protocol (2005), the Copenhagen Accord (2009) and the Paris COP 21 UN conference (2015) [5]. Considering the last one, the purpose of this agreement signed by 195 countries, is to maintain global warming under 2 °C compared to the pre-industrial level [6]. Moreover, total renewable energy consumption is expected to increase by almost 30 % over 2018-2023. In this scenario, biomass resources play an important role. Indeed, biomass valorisation is one of the strategic topics of Horizon 2020 (H2020), the European Union Framework Programme for Research and Innovation for 2014-2020 since it is an ideal alternative to fossil sources [7]. Biomass is a carbon neutral source as it binds carbon during the growth and releases it when it is used. Therefore, it does not contribute to greenhouse gases emission. Actually, around 115×10^9 tons of atmospheric C is transformed into biomass, producing 170-200 10^9 tons/y of biomass in the world [8]. Despite this huge availability, only 2 % of cell-wall-based biomass is employed. Moreover, biomass feedstocks are worldwide spread thus, the problem of geopolitical dependence between the regions with different fossil sources availability could be suppressed. For all these reasons, the development of new and efficient technologies to produce energy and chemicals from biomass is a rapidly evolving field of research.

1.2 Biomass as a renewable resource

Biomass is a complex matrix originated from vegetation plants and organic wastes, whose composition varies due to the origin and the nature of the raw material. Indeed, biomass is classified into several groups and sub-groups according to their similar source and origin: woody, herbaceous and agricultural, aquatic, animal and human waste and, industrial biomass waste [9]. Generally, the composition of biomass feedstock is very broad, and it is mainly made up of carbohydrates, lignin, lignocellulose macrostructure, extractives, protein, ash, and triglycerides [10].

During the last century, the use of biomass has raised ethical, social and economic issues as a result of the exploitation impact upon food supply and prices. For this reason, the first used biomass, such as sugar and corn, defined as first generation biomass, has been completely replaced by the second and third generations. The second one is defined as the inedible and waste biomass feedstocks, named lignocellulosic biomasses, which nowadays play a crucial role in the production of biochemical and biofuels [11]. The third type comes from algae and marginal land cultivations, as well as genetically modified microorganisms and plants grown and used for specific purpose [12]. In this research work, lignocellulosic biomass has been considered.

1.3 Lignocellulosic biomass

Lignocellulosic biomass is the most abundant inedible biomass; thus, it represents a promising source for biochemical and biofuel production. It is composed of three primary chemical fractions: cellulose, hemicellulose, and lignin. The most abundant part is the cellulose, which covers about 40-60 % of the feedstock. The hemicellulose and lignin fractions can be found on average among 15-30 % and 10-25 % respectively [13]. The remaining part is mainly composed of a smaller amount of fatty acids, ashes, tannins, vitamins, aromatic essence, inorganic salts, and lipids. Clearly, the percentage of each component depends on the species [14]. A schematic illustration of lignocellulosic material is represented in Figure 1.2.

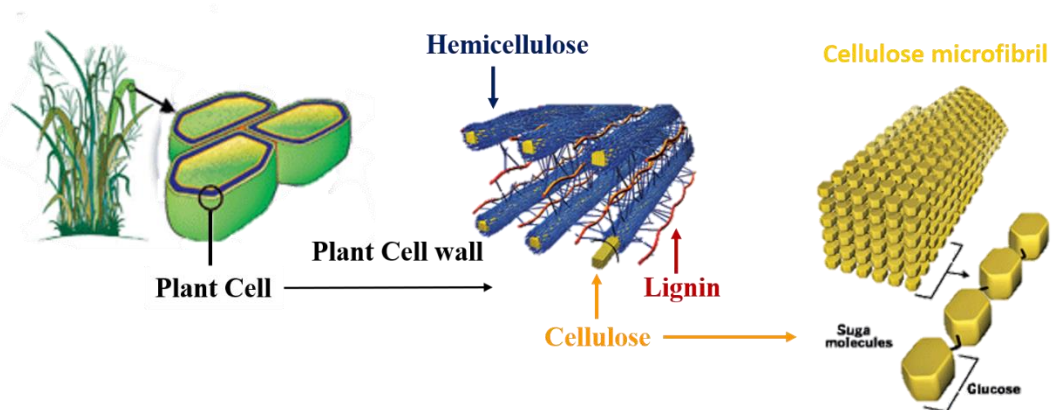


Figure 1.2 All fractions of lignocellulosic materials.

As visible in Figure 1.2, cellulose is a well-known homopolysaccharide form by C₆-glucose monomers linked by $\beta(1-4)$ glycosidic bond [15]. It is an important structural component of the cell-walls of plants and it is the most abundant biopolymer on earth. Hemicellulose has a crucial role in the mechanical properties of biomass. Indeed, it binds lignin and cellulose forming a network of cross-linked fibers. It is a heteropolymer composed of C₆ and C₅ sugar units, connected by different glycosidic bonds. Lignin envelops the entire structures of cellulose and hemicellulose as glue and allows the plants to have overall rigidity, strength and resistance to degradation. Unlike cellulose and hemicellulose, it is a non-carbohydrate and amorphous polymer consisting of a network of phenolic groups. P-coumaryl, coniferyl, and sinapyl alcohols are the main components of the lignin fraction.

The highly organized structure and the wide number of functionalities such as simple and complex sugars and aromatic compounds makes this material versatile towards the production of value-added products. Nevertheless, the very rigid and complex structure of the material requires a fractionation step to extract each component. As represented in Figure 1.3, the pretreatment step should be properly selected for the progressive biomass transformation. There are many processes involved in the conversion of woody biomasses into chemicals, energy, and fuels. These processes can be classified into two categories: thermochemical and biochemical processes. Combustion, pyrolysis, gasification and thermal liquefaction belong to the first category while fermentation and digestion are classified as biochemical reactions [8]. Figure 1.3 schematizes possible conversion technologies for the treatment of lignocellulosic materials.

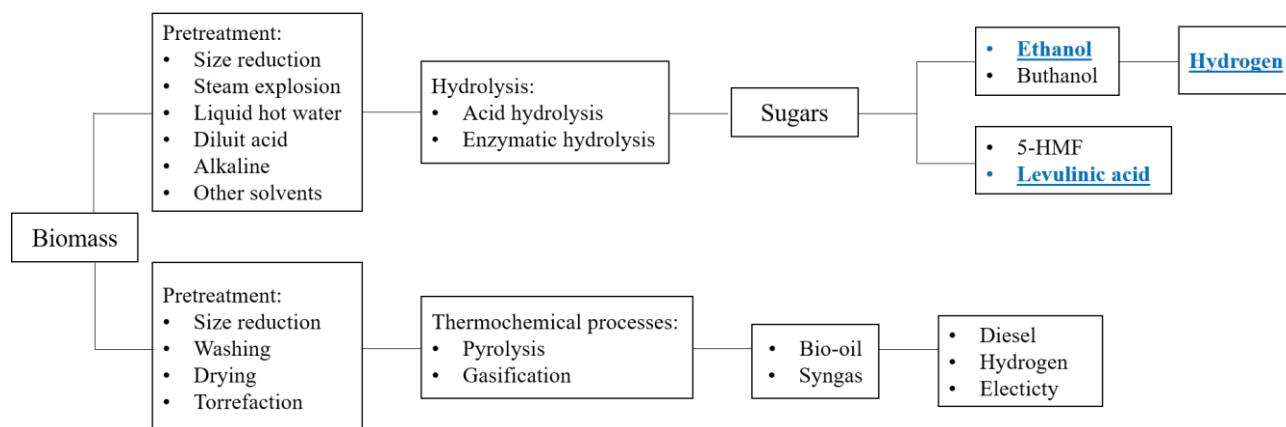


Figure 1.3 Schematic representation of conversion technologies for lignocellulosic materials.

Indeed, two main processes have been studied in this research work to valorize biomass and produce from it one fuel and one chemical respectively. Hydrogen (H₂) has been chosen as fuel since it is considered the future energy vector, while Levulinic acid (LA) has been identified as chemical due to its attractive properties as bio-based building block (the main reaction pathways involved are schematized in Figure 1.3). The common denominator of the addressed topics is the heterogeneous catalysis. Nowadays, all fuels and almost 85 % of chemicals that came out from petrochemical refineries have passed at least through one catalytic step. Of course, catalysis is expected to play a pivotal role also in the development of new processes and technologies in the 21st century within the biorefinery concept.

The work reported in this thesis can be divided into two parts united by the sustainability of the studied process and the production of biomass derivatives via heterogeneous catalysis. The first part relates to the development of solid, resistant and active heterogeneous catalysts for H₂ production. Ethanol steam reforming has been selected as the process for producing H₂ from biomass. In the second part, focused on LA production, glucose hydrolysis has been selected as the reaction and the attention has been focused on the formulation of heterogeneous acid catalysts. Figure 1.4 shows a schematic representation of all the developed topics. After that, it is reported a brief introduction on H₂ and LA production, paying attention to the optimal desired features of the catalyst and stressing how this work has tried to implement and develop the most suitable one for each process.

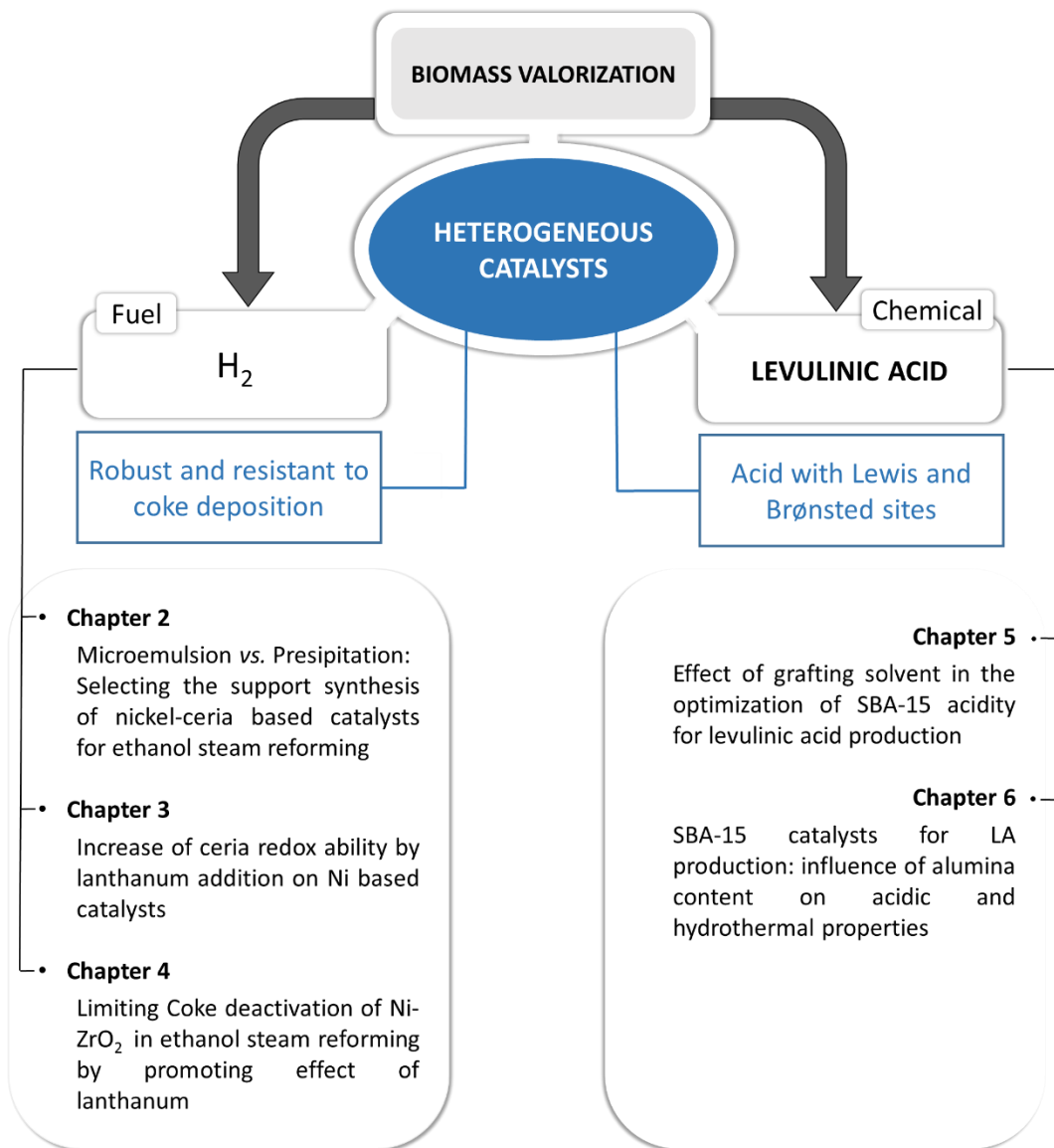
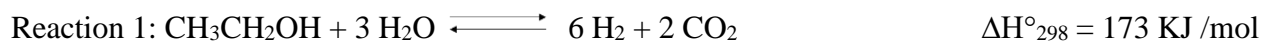


Figure 1.4 Schematic representation of all the developed topics

1.4 H₂ production via Ethanol Steam reforming

Hydrogen is one of the most abundant chemical-intermediate products and, as mentioned before, it is considered the future energy vector for its great potentiality for generating electricity in fuel cells [16,17]. Indeed, longer-term strategies of car manufacturers are devoted to developing and commercializing electric vehicles based on hydrogen fuel cells, and some of them have already put these cars into the open market [18]. Other advantages of hydrogen exploitation are its rapid burning speed, the high specific energy density (between 120 MJ/kg to 142 MJ/kg) which is 2.75 times higher than the other hydrocarbons and its nontoxic and clean nature [19]. However, hydrogen presents multiple sets of problems regarding its transport and storage. The infrastructures currently used for fossil fuel distribution are hardly adaptable for the H₂ suppliers. Therefore, safety and regulatory issues must be considered. Moreover, a critical theme in the use of hydrogen as a clean fuel is its production method. In fact, despite hydrogen is the most abundant element in the universe, it does not exist in the elemental form [20]. Therefore, it must be produced from hydrogen-containing sources. Nowadays, 96 % of the hydrogen produced worldwide derives from the reforming of natural gas [21]. The remaining part is generated by the water electrolysis, which works with electricity generated by the combustion of fossil fuels. Therefore, the transition to a hydrogen era can only be achieved transforming resources and production processes completely, using renewable substrate and environmentally friendly processes.

Nevertheless, one of the potentials of H₂ is the possibility of generating it from renewable sources. Among the most attractive processes, the steam reforming of light alcohols such as ethanol plays a key role [22]. Indeed, ethanol, as already described, can be generated by the fermentation of carbohydrate sources [19]. Moreover, in addition to the already mentioned use of renewable sources, the use of ethanol as a reagent for H₂ production has countless advantages: low cost, easy transportation in liquid form and the possibility to convert it into H₂ in relatively mild reaction conditions [23] and highly efficient and cost-effective process. For example, the conversion of ethanol into H₂ via steam reforming provides six moles of hydrogen per mole of ethanol (Reaction 1) [24]. Besides, it can give H₂ not only from ethanol but also from water.



Despite the multiple advantages, ethanol steam reforming is a complex process that includes reactions such as decomposition, ketonization, dehydrogenation, reforming and water-gas shift. The schematic representation of the composite reaction pathway is reported in Figure 1.5.

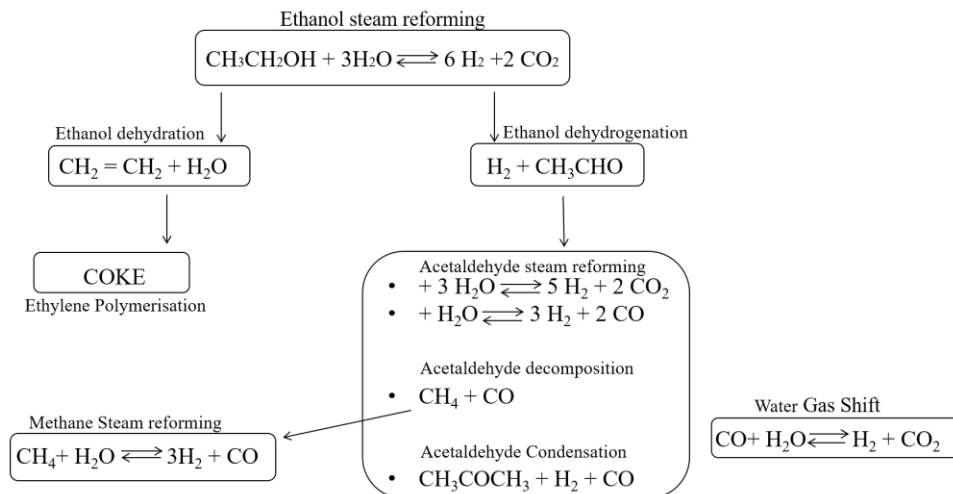
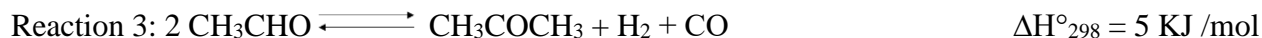


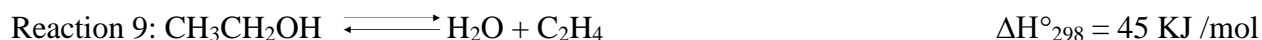
Figure 1.5 The schematic representation of the ethanol steam reforming pathway

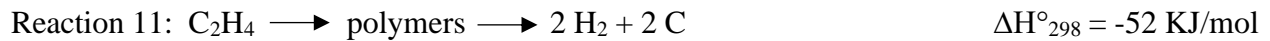
Thus, it involves the formation of several by-products such as CO, CH₄, ethylene, acetaldehyde and more complex carbon species [25]. Depending on the thermodynamic conditions, ethanol can follow two decomposition pathways: dehydrogenation to acetaldehyde and dehydration to ethylene. These products, themselves, can consequently be converted modifying the hydrogen yield and the efficiency of the entire process.

Ethanol dehydrogenation followed by acetaldehyde pathway can be summarized in the following reactions:

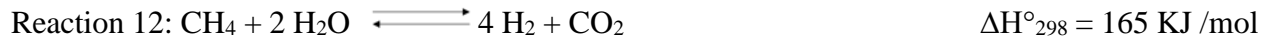


Dehydration of ethanol to ethylene involves the following reactions:





Moreover, methanation (Reaction 12), Water Gas Shift (WGS) (Reaction 13) and Boudouard reactions (Reaction 14) can take place in the process.



Considering the thermodynamic constants, reported at the end of each equation, it is clear how experimental conditions can strongly influence the progress of the reactions. The endothermic reforming reactions are favored at high temperatures, while WGS is depressed. Moreover, another important aspect that can drive the reaction to maximize hydrogen yield and suppress unwanted reaction is the catalyst. For this reason, the catalyst should be properly formulated to be functional for this purpose.

1.4.1 Catalysts for H_2 production

The industrial manufactories and most of the researchers focus on heterogeneous supported metal catalysts since they are the most stable against carbon deposition and thermal stress [26]. The most active metals for this kind of reaction are the noble ones, in particular, platinum, palladium, and rhodium [27]. However, due to their high cost, noble metals are less attractive for industrial applications. Nickel is the most interesting substitute due to the good compromise between cost and efficiency. Indeed it is the traditional active phase used for industrial methane steam reforming [28]. Despite nickel is extensively studied, it presents two main problems related to its nature: sintering and deactivation due to carbon deposition. Han *et al.* [29] explained how nickel aggregation is strongly related to the temperature work. In fact, above 230 °C crystallite migration takes place, leading to the formation of larger Ni particles. For this reason, the role of support in the stabilization of nickel active phase has a crucial importance. It must operate in synergy with the active phase, guaranteeing high stability, activity and resistance for the process [30]. Normally, the main characteristics of an ideal support are 1) high thermal and mechanical stability; 2) good interaction with the active phase; 3) large surface area and 4) robust resistance to coke deposition [30-32]. Alumina, silica, titania, ceria, and zirconia are typically used. Alumina is the most widely studied support for the steam reforming reaction. Indeed, due to its thermal stability and good interaction with the active phase, it is employed in the stabilization of nickel particles in the industrial methane steam reforming. At the same time, alumina has some limitations when ethanol is employed as a starting reagent. Indeed, its partially acid nature promotes the dehydration reaction (Reaction 9), leading to coke formation [33]. Basic promoters, such as calcium, barium, manganese, and strontium oxides have been added to alumina support to mitigate this behaviour and an increase in activity and stability has been achieved [34]. However, alumina has a restriction at low temperature conditions (300 °C- 400 °C) since it interacts lowly with water vapour, blocking OH- and H- division [35]. For energy savings, the operating reforming temperature has tried to be reduced as much as possible; therefore, the use of other supports has gradually spread out. Ceria and zirconia are typically used as promoters or co-supports in reforming applications. Indeed, they are applied to increase the stability and activity of the major one. Nevertheless, thanks to their redox nature, their use as pure support has increasingly become common [31,32]. For this reason, in this research work, they have been selected as supports for nickel-based catalysts and a deep implementation of their features has been performed.

Ceria is normally used in CO oxidation reaction, preferential oxidation (PROX) of CO for hydrogen purification and water gas shift (WGS) reaction since it can act as oxygen pump [36]. Indeed, its oxidative state could mutually change from 4+ to 3+, modifying the structural shape from CeO₂ to Ce₂O₃ [37]. In this way, the formation of oxygen vacancy can promote the oxidation of carbonaceous species on the surface, limiting coke deposition [38,39]. Moreover, ceria is also widely employed as anode inside fuel cells [40]. Another important aspect is that ceria redox ability can be modulated by careful control of structural defects: the highest is the number of defective sites, the most effective is the redox pump [41]. For this reason, many studies focused the attention on ceria modification. In this work, two main aspects have been considered to modify ceria properties: the synthetic approach and the introduction of promoter. The ceria synthetic approach influences its textural properties, such as specific surface area, crystallinity and stability and as a consequence, its catalytic activity [42]. Therefore, two different synthetic methods have been investigated for ceria preparation: precipitation and reverse microemulsion. Precipitation is the standard approach used for metal oxides preparation. With this method, it is difficult to control particle size distribution. On the contrary, reverse microemulsion can be an innovative way to modulate and control the morphological properties of new materials. Indeed, this approach is based on the formation of nanospherical micelles inside which the precipitation of the oxide takes place. In this way, as reported by Eriksson *et al.* [43] it can be generated a suitable environment for producing small nanoparticles of narrow size distribution. The results of this study are reported in Chapter 2. In the other case, after the determination of the best synthetic approach for ceria preparation, a deeper modification of morphological, structural, and chemical properties has been performed using a promoter. Laguna *et al.* described how oxygen vacancies population is increased by introducing Fe³⁺ inside ceria lattice [44], while Andana *et al.* used Cu²⁺ [45]. Lanthanum oxide could be an innovative promoter in this sense. La³⁺ could substitute Ce⁴⁺ on support lattice, increasing its redox ability [45]. The similar dimension of ionic radii (La³⁺ = 1.16 Å and Ce⁴⁺ = 0.97 Å) could facilitate the interaction between the two elements. Moreover, lanthanum oxide is a structural promoter, with high mechanical strength that could increase ceria stability at high temperatures [46]. The results of this work are reported in Chapter 3.

Zirconia is really attractive for its acidic, basic, oxidizing and reducing properties [47]. It presents high mechanical and thermal stability and redox ability that are used to catalyse a wide range of reactions such as hydrogenation of olefins, isomerization of olefins and epoxides, and

dehydration of alcohols [48]. Furthermore, considering the reforming application, it is an optimal support since it can easily adsorb and then dissociate water, thus enhancing the adsorption of steam on the catalyst surface and activating the gasification of hydrocarbons and the water gas shift reaction [49,50]. Moreover, it strongly interacts with nickel particles, preventing metal sintering [51,52]. Despite the huge potentiality of zirconia supports, it has a partial Lewis acidity that, as for alumina, can favour dehydration reaction [53]. The addition of basic promoters such as alkali and alkali-earth metals should reduce the acidity of support thus preventing unwanted reactions. Therefore, different researchers emphasised the use of promoters, such as calcium, magnesium, and potassium in the activity of acidic supports [33,34]. For instance, Nichele *et al.* reported the effect of CaO on zirconia in reducing the Lewis acidity of support and inhibiting coke formation. Thus, CaO produces oxygen vacancy on the support, activating CO₂ and H₂O, thus favouring the gasification of coke [54]. Besides the metals alkaline and alkaline earthy, the lanthanides were studied as basic promoters. As it is described by Osorio-Vargas *et al.*, lanthanum oxide addition in nickel-alumina catalyst reduces the selectivity to ethylene decreasing support Lewis acidity [55,56]. At the same time, lanthanum oxide, compared to other basic materials, can interact with the carbonaceous species deposited on metal, freeing the surface. P. Osorio-Vargas *et al.* reported this effect for Ni/Al₂O₃ catalyst [55]; La₂O₃ react with CO₂ to form lanthanum oxycarbonate species (La₂O₃ + CO₂ ⇌ La₂O₂CO₃), that therefore can react with carbon-metal species to produce CO (C-Me + La₂O₂CO₃ ⇌ 2 CO + Me + La₂O₃) [57,58]. Indeed, in line with the ceria case, the effect of promoter, as lanthanum, has been studied also for nickel zirconia catalyst. The results of this study are reported in Chapter 4.

1.5 Levulinic acid production

LA (4-oxopentenoic acid: 5-ketovaleric acid) is a short-chain fatty acid composed of five carbons with two different functional groups, a carboxylic unit and a keton one that make it versatile for numerous potential uses such as succinic acid [59], γ -valerolactone [60], valeric acid [61], pentanoic acid and esters [62], ethyl levulinate [63] and 2-methyltetrahydrofuran [64],[65],[66]. For this reason, in 2004 it was defined by Werpy and Petersen (USA Department of Energy) as one of the top twelve bio-based building blocks [67]. Hence, it was calculated in 2014 that the universal market demand of levulinate compounds was 32.4 tons (valued as \$ 8.8 Millions) and it is expected that it could reach a value of 49.1 tons (valued as \$ 11.8 Millions) by 2022 [68]. Given the powerful demand for these products, in recent years the research has strongly focused on studying green and feasible methods for LA production. Historically, LA was produced by fossil sources via maleic anhydride [69]; nevertheless, from the second half of 20th century, the production of levulinic acid has been developed using biomasses as feedstocks [70]. Bernard and Guy patented a way of producing LA starting from furfuryl alcohol, water, and strong acid, which was also applied in industry. However, the use of furfuryl alcohol was easily replaced by much widespread biomass substrate [71]. Indeed, the commercial production of LA from starch began in the United States in the 1940s [72] and from that moment, the LA production from biomass has been intensified. Researchers started to study all the parameters that could affect the efficiency of the process such as the catalysts, the properties of raw material and the reaction conditions [73]. LA production is based on the conversion of the polysaccharide via acid hydrolysis [74]. Through biomass conversion, hemicellulose and cellulose can be hydrolysed into their monomer units. Among them, glucose, the most common monosaccharide existing in nature, is a highly attractive substrate for LA production due to the abundantly and cheap availability. In Figure 1.6 it is reported a schematic representation of the glucose hydrolysis. It includes glucose isomerization to fructose (step 1) followed by dehydration of the ketose monomer to 5-(Hydroxymethyl)furfural (5-HMF) (step 2) and the subsequent rehydration of the furfural compound to form LA and an equivalent of formic acid (FA) [75] (step 3).

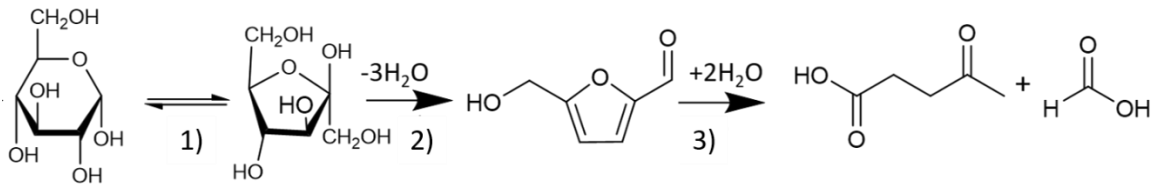


Figure 1.6 Reaction scheme of glucose hydrolysis.

The overall reaction network is complicated due to side reactions, as schematised in Figure 1.7. Glucose reverse reaction leads to the formation of cellobiose and levoglucosan, while glucose degradation and glucose epimerisation produce mannose and fructose. All these compounds can be decomposed by forming highly polymerized carbonaceous species called humins, which decrease the efficiency of the entire process [76].

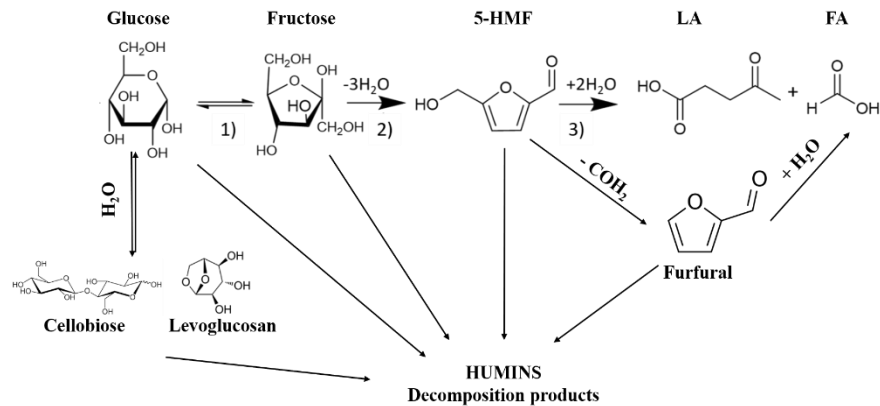


Figure 1.7 Composite reaction pathway of glucose hydrolysis

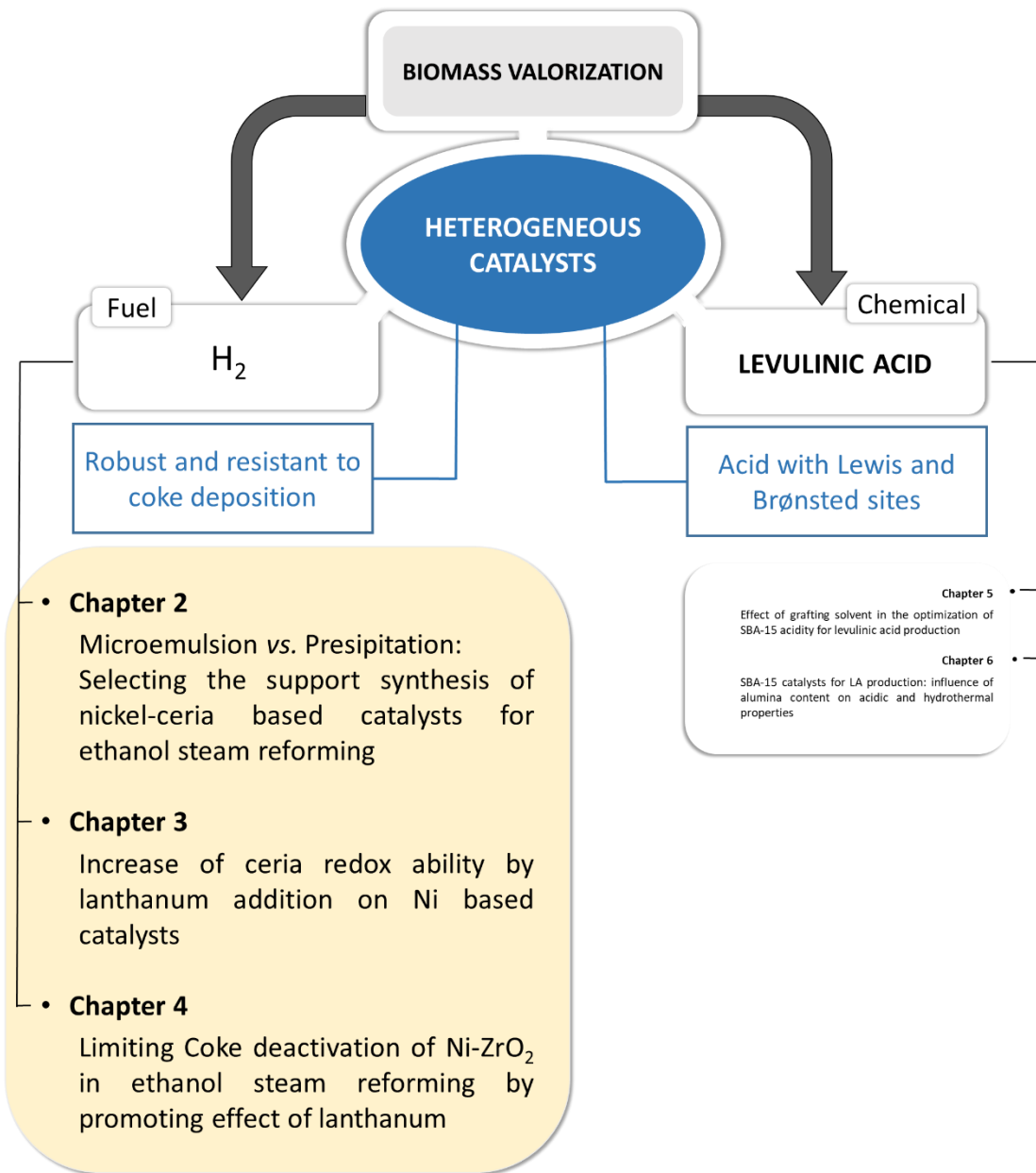
Kinetic studies reveal that the energy barrier of glucose isomerisation to fructose ($E_a = 88.6$ kJ/mol) is 17% lower than that to mannose ($E_a = 107.3$ kJ/mol), suggesting that fructose can be the major isomeric product under appropriate kinetic control [77]. Nevertheless, in order to guarantee the formation of LA, the catalyst has a pivotal role in the reaction pathway. In particular, acid catalysts are fundamental in this transformation. Lewis acids catalyse the first isomerization step from glucose to fructose; dehydration of fructose to 5-hydroxymethylfurfural (5-HMF) is catalysed by both Lewis and Brønsted acid sites, and the rehydration of 5-HMF to LA and FA is catalysed by Brønsted acid sites [68],[78,79].

1.5.1 Catalysts for LA production

Chemocatalytic conversion of glucose into LA can be classified in homogeneous and heterogeneous reactions [80]. Industrially, strong mineral acid such as H_2SO_4 , HCl , HNO_3 , and HClO_4 are employed [81]. Indeed, dilute sulphuric acid is the catalyst used in the Biofine process, the most advanced and commercially available technology for LA production [82]. It comprises of two acid catalyzed steps developed into two different reactors, to avoid side products formation [83]. In the first reactor, hexose sugars are converted into 5-HMF at 200-230 °C and 20-25 bar. After this step, the intermediate is transferred into a second reactor in which the hydrolyzation to LA happens at 190-220 °C and 10-15 bar. This process is the most efficient one, leading to the highest value of LA yield reported in the literature, 70-80 mol% [84]. Nevertheless, despite the high efficiency and low cost, strong mineral acids present various fences in their application such as rig corrosion, difficulty in products and catalyst separation and high waste generation. For this reason, researchers are focusing on the development of more sustainable and recyclable heterogeneous systems [85,86]. Several solid acid materials have been investigated for LA production starting from ion-exchange resins, zeolite, sulfated zirconia, ion-exchange heteropolyacids, and sulfonated solids [87–90]. Sulfonated ion-exchange resins are copolymers of styrene and divinylbenzene functionalised with sulfonic acid sites (i.e., $-\text{SO}_3\text{H}$ groups). Amberlyst, Nafion and Dowex have been widely applied for sugar conversion reactions. Nonetheless, two of the main limitation of these materials are poor thermal stability (~ 150 °C) and insufficient acidity. Indeed, sulfonated ion-exchange resins are characterised of Brønsted acid sites only [91,92]. Unlike the ion exchange resins, zeolites are characterized by the presence of both acidic functionalities, Brønsted and Lewis respectively. They are microporous crystalline aluminosilicates, formed by tetrahedral TO_4 (T = Si, Al, etc.) units linked by shared O corners [93]. The coordinatively unsaturated cations in zeolite act as Lewis acid sites, while the hydroxylic groups provide the Brønsted sites [94]. Indeed, thanks to their strong acidity, high hydrothermal stability and define pore structure, they are commonly applied as solid acid in the chemical industry for cracking, hydrocracking, isomerisation, reforming and other industrial important topics[95]. Moreover, their acidity can be further enforced by the introduction of unsaturated cations; Rampli *et al.*[96] impregnated FeCl_3 on HY zeolite increasing the number of acid sites and enlarging the pore size. With this method, they implemented the LA yield in comparison to the not promoted material, reaching the value of 62% [97]. Xia *et al.* [98] reported the increase of glucose conversion

by the addition of Sn on Beta zeolite. However, the tiny and narrow pore dimension of zeolites restricts their reactivity and efficiency in LA production due to the limited access and diffusion of reagents to the active sites [99]. For all these aspects, zeolites are suitable acid catalysts for sugar conversion but hinder their use in raw biomass feedstock conversion. On the contrary, metal oxide from Group IV and V are interesting materials due to unsaturated coordination of metal species as water-tolerant Lewis acid sites [76]. Exposed oxygen-deficient cations of metal oxides act as Lewis acid centres, while hydroxyl groups are responsible for the Brønsted acid sites [100]. Moreover, these solid materials such as γ -Al₂O₃, SiO₂/Al₂O₃, TiO₂, ZrO₂, ZrO₂/TiO₂ are generally sulfonated to increase their catalytic performance in the glucose hydrolysis reaction. Nonetheless, the study of metal oxides as catalysts has been limited caused by their relatively low surface area. Indeed, acidity and surface porosity are the most important parameters that must be carefully adjusted to obtain a good selectivity and yield of LA. For this reason, in Chapter 5 and 6, SBA-15, an ordered mesoporous silica material, has been studied. Indeed, it has been selected as the catalyst support owing to its high surface area, large pore volume and appreciable thermal and hydrothermal stability [101]. Since Lewis and Brønsted acid sites are required for sugar conversion to LA, modification of SBA-15 surface features has been performed. Implementation of Brønsted acidity is reported in Chapter 5, while enhancement of Lewis acidity is discussed in Chapter 6. The implementation of Brønsted acidity has been performed via functionalization with sulfonic acid groups. Different methods can be used to introduce sulfonic sites and the various approaches can involve direct synthesis, mainly consisting of co-condensations methods or post-synthesis techniques. The direct synthesis method in many cases leads to loss of the mesoscopic order of the pore architecture, due to the strong synthetic conditions [102,103]. Considering the post-synthesis approach, the introduction of sulfonic groups is usually performed in concentrated sulfonic acid by heating process, which is dangerous and unsustainable [104]. An effective alternative to the direct sulfonation method is the surface alkoxy silanes grafting. It consists of a post-synthesis strategy, by which the active functionalities are anchored on the support surface via covalent bonds. This process is generally carried out in the presence of a grafting agent, such as 3-mercaptopropyltrimethoxysilane (MPTMS), the silica matrix and the solvent [157]. The traditional one is toluene, which is flammable, toxic and not environmentally friendly [105]. For this reason, a safer solvent could be an attractive alternative to make this process more sustainable. In Chapter 5, it is presented the effect of solvent in the efficiency of grafting procedure. Moreover, to

implement the Lewis acidity of this material, further modifications have been performed. Many works have been reported in the literature regarding the synthesis of various silica-metal SBA-15 type composites [106]. Szczodrowski *et al.* reported the doping effect of Al, Ti, Zr in the hydrothermal stability and acidity of SBA-15 [107] in which they emphasised the main difficulties in the incorporation of Heteroatoms due to the weak Heteroatom-O-Si bond and the differences in hydrolysis precursor velocity. For this reason, aluminium has been selected as the promoter of SBA-15 due to the similarities of atom size with silicon and the ability to easily enter into silicon skeleton [108]. Chapter 6 presents the study of the optimization of support hydrothermal stability and the implementation of Lewis acidity by the addition of alumina as co-support.



Chapter 2 . Microemulsion vs. Precipitation: Selecting the support synthesis of nickel-ceria based catalysts for ethanol steam reforming

The work reported in this chapter was performed at the CSIC - Instituto de Catálisis y Petroleoquímica in Madrid under the supervision of Prof. Vicente Cortés Corberán.

As mention before, it was investigated the effect of ceria preparation method on activity, stability and regeneration of nickel-ceria based catalysts for H₂ production via ethanol steam reforming. Precipitation and Microemulsion methods were evaluated. It was observed that the preparation method strongly affects the structural and chemical properties of those materials. Considering their catalytic performances in ethanol steam reforming the catalyst prepared via precipitation shows higher catalytic activity and stability, while the catalyst prepared via microemulsion deactivates faster. The correlation between the synthetic method with structural and morphological properties was explored using characterisation techniques as N₂-physisorption, SEM, XRD, and H₂-TPR.

2.1 Experimental

2.1.1 Catalyst preparation

- *Precipitation method:* the support (denoted as Ce P) was synthesized by precipitation from (NH₄)₂Ce(NO₃)₆ (Sigma Aldrich) with urea at 100 °C in aqueous solution. The solution was mixed and boiled for 6 h at 100 °C, the precipitate was washed in deionized water and dried at 110 °C for 18 hours. The material was then calcined under air flow (30 mL/min) at 650 °C for 3 h.
- *Reverse microemulsion method:* the support (denoted as Ce M) was synthesized by preparing two different microemulsion systems: A) saline microemulsion composed by n-heptane 99%, 1-hexanol 98%, Triton X-100 and 0.5 M Ce(NO₃)₃ 6H₂O solution and B) basic microemulsion composed by n-heptane 99%, 1-hexanol 98%, Triton X-100 and 0.5 M (CH₃)₄N(OH) solution. Both microemulsion were stirred at 100 rpm for 1 h. Then, solution B) was added to solution A) and kept stirring at 100 rpm for 24 h. The precipitated was centrifugated and washed with methanol, dried at 120 °C for 18 h and calcined in air at 650 °C for 3 h.

- *Introduction of nickel oxide:* nickel was introduced on the support by incipient wetness impregnation with a proper amount of $\text{Ni}(\text{NO}_3)_2 \cdot 6\text{H}_2\text{O}$ aqueous solution in order to obtain 8 wt % of nickel on the material. After drying at 110 °C for 18 hours, calcination was performed in air at 650 °C for 4 hours. The samples were labelled NiCe P and NiCe M.

2.1.2 Catalyst characterisations

Specific surface areas and pore size distributions were evaluated by N_2 adsorption/desorption isotherms at -196 °C using a Tristar II Plus Micromeritics. Surface area was calculated using B.E.T. equation [109] method while pore size distribution was determined by the B.J.H. method [110], applied to the N_2 desorption branch of the isotherm.

SEM were conducted using a Hitachi Tabletop Microscope TM3000.

X-ray diffractograms were obtained on a Seifert XRD 3000P diffractometer using nickel-filtered $\text{Cu K}\alpha$ radiation operating at 40 kV and 40 mA, using a 0.02° step size and 2 s counting time per step. Analysis of the diffraction peaks was done with the software ANALYZE Rayflex Version 2.293.

Temperature programmed reduction (TPR) measurements were carried out in a lab-made equipment: samples (100 mg) were heated with a temperature rate of 10 °C/min from 25 °C to 900 °C in a 5% H_2/He flow (40 mL/min). The effluent gases were analysed by a TCD detector.

2.1.3 Catalytic tests

Catalysts were tested for ESR at 500 °C and atmospheric pressure, with a feed of molar composition water:ethanol:He = 18.4:3.1:78.5 and W/F = 0.12 gcat.h/mol ethanol, in a stainless steel, fixed bed tubular reactor placed in an equipment Microactivity Reference model MAXXXM3 (PID Eng & Tech). Prior to the reaction, fresh catalyst samples were activated under flow of 10% O_2 diluted in He, at 650 °C for 1 h. Catalytic stability tests were conducted at 500 °C for 5 h. After the first run, the catalyst was cooled down and flushed under inert flow, and then reactivated using the same procedure of the initial activation, heating up to 650 °C at 10 °C/min and keeping this temperature for 1 h, under a flow of 10% O_2 in He. Then, after cooling down to 500 °C in inert flow, a second run was conducted with the regenerated samples under the same conditions of the first run. Tests for each sample were reproducible within experimental error. Reactants and products were analyzed on line by GC on a Varian Star 3400 CX instrument equipped with two columns, molecular sieve and Porapak Q. Thermal conductivity was used as

detector. After the analysis, conversion of ethanol and hydrogen yield were calculated using the following equations:

Conversion of ethanol:

$$\text{conversion (\%)} = \left[\frac{f_{in}(\text{EtOH}) - f_{out}(\text{EtOH})}{f_{in}(\text{EtOH})} \right] * 100$$

H₂ yield:

$$\text{yield (\%)} = \frac{f_{H_2 \text{ out}}}{6 * f_{EtOH \text{ in}}} * 100$$

where f is the flow in mol/min.

2.2 Results and Discussion

2.2.1 Catalysts characterisations

One of the most important parameters in the design of heterogeneous catalysts is the specific surface area: a high surface area greatly improves the dispersion of active phase [28,111]. Figure 2.1 reports N₂-physisorption isotherms in section a) and BJH pore size distribution in section b), while in Table 2.1, specific surface area, pore radius and pore volume are reported.

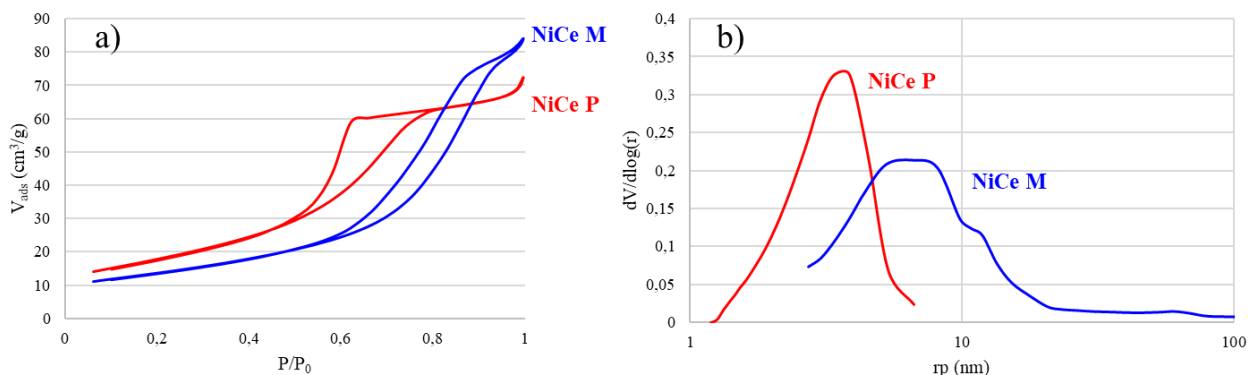


Figure 2.1 N₂-physisorption isotherms (section a) and BJH pore size distribution (section b) of NiCe P and NiCe M

Both samples exhibit IV-type isotherms with H2 hysteresis loop, according to IUPAC classification [112]. This isotherm shape is typical of mesoporous materials with not well defined pores. However, the shape of both isotherms and the hysteresis loops are quite different. The N₂ adsorbed volume on NiCe P is higher than on NiCe M, suggesting a higher specific surface area, as evidenced by their B.E.T. values reported in Table 2.1. Moreover, for NiCe P the hysteresis loop starts at lower P/P₀ value than for NiCe M. Indeed, looking at the pore radius distribution reported in section b) of Figure 2.1, it can be noted that pore size distribution is sharper and at smaller values for NiCe P than for NiCe M. NiCe M presents a broad distribution that reaches the limit of macroporosity.

Table 2.1 Physico-chemical properties of NiCe P and NiCe M. a) Specific surface area calculated via BET, b) Average pore radius and c) Pore volume calculated via BJH method and d) crystallite dimension calculated via Scherrer equation via XRD.

Samples	A _{sup} (m ² /g) ^a	r _{pore} (nm) ^b	V _{pore} (cm ³ /g) ^c	NiO Particle size (nm) ^d	Ceria particle size (nm) ^d
NiCe P	64	2.8	0.11	14	9
NiCe M	48	5.9	0.12	9	7

The particles morphology and size of these materials were determined using microscopy techniques. Figure 2.2 shows SEM images of the samples. The appearance of the two materials is notably different. NiCe P is made of spherical agglomerated particles of 1.8-2 μm , while NiCe M presents a wrinkled surface covered by small superficial cubic particles.

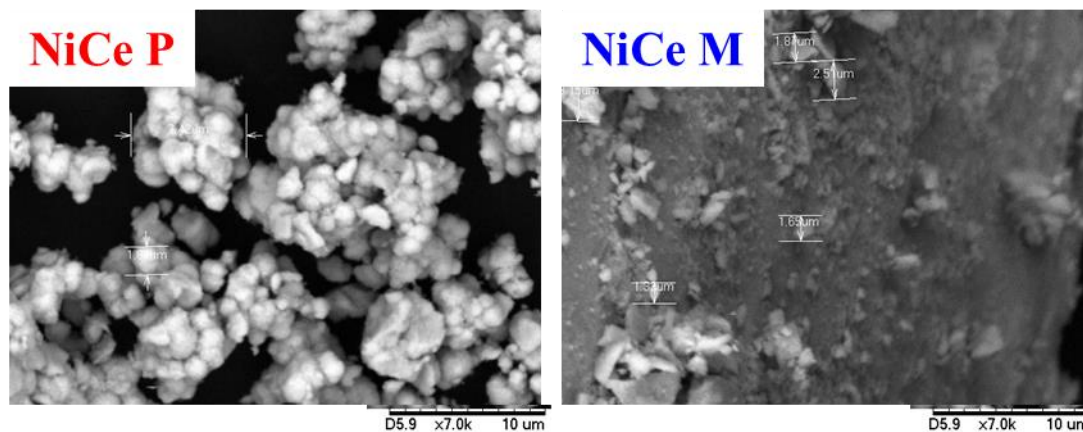


Figure 2.2 SEM images of NiCe P and NiCe M

XRD analysis using Scherrer refinement were carried out to determine the crystal size of the support and the metal phases in the samples. Figure 2.3 compares the XRD patterns of NiCe samples prepared via different support preparation methods.

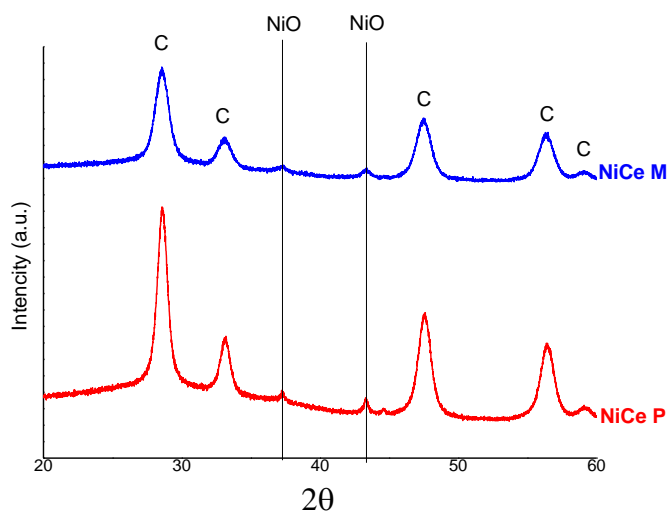


Figure 2.3 XRD patterns of NiCe P and NiCe M

Both XRD profiles show a fluorite-type phase of ceria with characteristic reflections at 2θ 28 °, 33 °, 47 °, 56 ° and 59 ° associated with (111), (200), (220), (311) and (222) planes of cubic phase, respectively [113]. Regarding the active phase, the occurrence of NiO is clearly detected, with the characteristic peaks at 2θ 37 and 43.4 ° [114]. Catalysts were charged into the reactor without pre-reduction; therefore, it is expectable the presence of nickel in the bunsenite phase. Table 2.1 shows the crystals size of NiO and cerianite phase, calculated from the analysis of the most intense diffractions, corresponding to 2θ 28 ° and 43.4 °, respectively. The pattern of the precipitated sample shows sharper and more intense peaks, meaning that the particles of ceria and NiO are bigger and more crystalline than for the catalyst prepared via microemulsion, as reported in Table 2.1. These preliminary characterisations indicate that the support preparation method strongly affects morphological and structural features of the final catalysts. Therefore, further characterisations were performed. TPR technique was used to identify the different NiO species on the ceria surface and their reduction features and to determine the support reduction temperature. The most evident difference between the two catalysts TPR profiles of Figure 2.4 was the number of NiO species interacting with the support. NiCe P thermogram presents three reduction peaks associated with NiO reduction at 204, 249 and 329 °C, while NiCe M, only one sharp peak centered at 470 °C. The broad maxima at higher temperatures are related to the supports, as ceria can be reduced from Ce^{4+} to Ce^{3+} at temperature above 700 °C. Considering the precipitated support, one small peak appears at 800 °C, while for microemulsion support there are two peaks at 750 and 1000 °C, respectively.

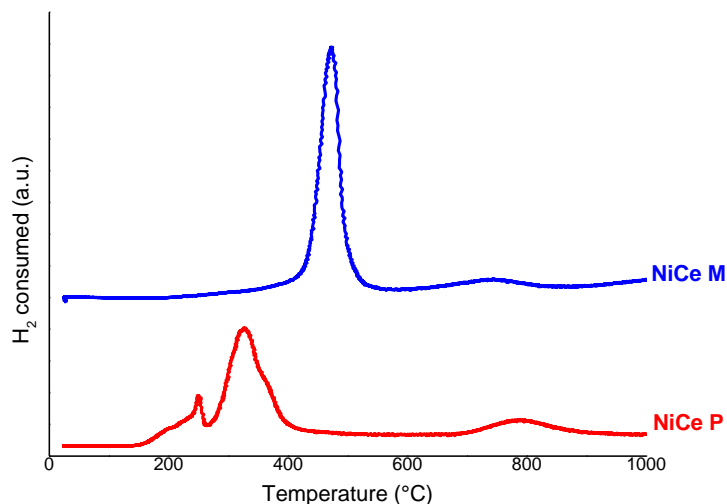


Figure 2.4 TPR profiles of NiCe P and NiCe M catalysts.

From these preliminary characterisations, remarkable differences between the two catalysts have arisen. NiCe P presents high surface area, well define spherical shaped particles and high crystallinity while NiCe M shows small NiO dimensions and a individual NiO interaction with the support. Therefore, it can be affirmed that the support preparation method strongly influences morphological, structural and chemical properties of the final catalysts.

2.2.2 Catalytic performance of Ni ceria catalysts

Catalytic tests were carried out at 500 °C. Figure 2.5 reports ethanol conversion (straight line) and hydrogen yield (dotted lines) along 5 h on stream. The two catalyst presented a high initial activity: nearly complete ethanol conversion and 60 % of hydrogen yield were achieved. Nevertheless, they suffered a progressive deactivation in different degrees along 5 h on stream. Thus, after 2.5 h NiCe M lost its activity for H₂ production, and thereafter it maintained a very low conversion. In the other case, the catalyst prepared via precipitation was the most active with 50 % conversion after and 30 % hydrogen yield after 5 h on stream.

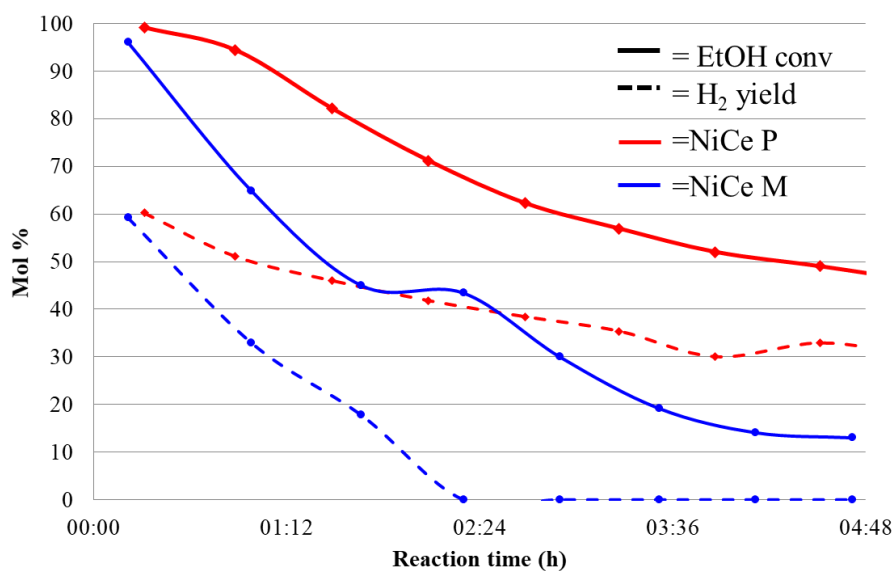


Figure 2.5 Ethanol steam reforming on NiCe P and NiCe M catalysts at 500 °C: ethanol conversion (straight line) and hydrogen yield (dotted lines)

In order to understand the reasons for these catalytic performances, characterisations of used catalysts were also performed. SEM analyses of samples are reported in Figure 2.6. As it can be seen, the catalyst prepared via microemulsion, NiCe M, was completely covered by carbon. On the other hand, the sample prepared by precipitation, NiCe P, still showed a very clear surface, despite it has some dark agglomerates associated with carbon deposits.

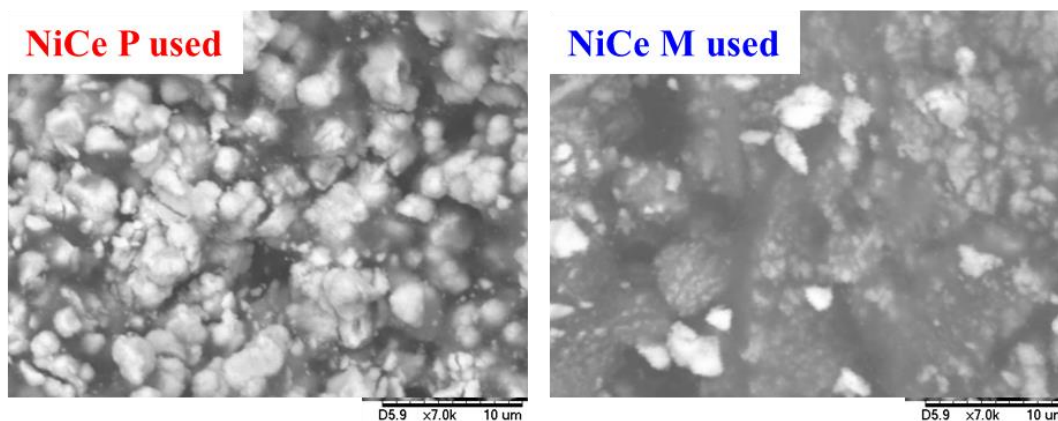


Figure 2.6 SEM images of used catalysts, in ethanol steam reforming tests.

To further understand the reason of this discrepancy in catalytic behaviour, X-Ray diffractions were also carried out on the used catalysts. It should be noted that these materials were not reduced before the reaction test and it is relevant to verify the reducing power of ethanol, as demonstrated by Pizzolitto *et al.* [115]. Figure 2.7 compares the XRD patterns of fresh and used catalysts for both prepared materials.

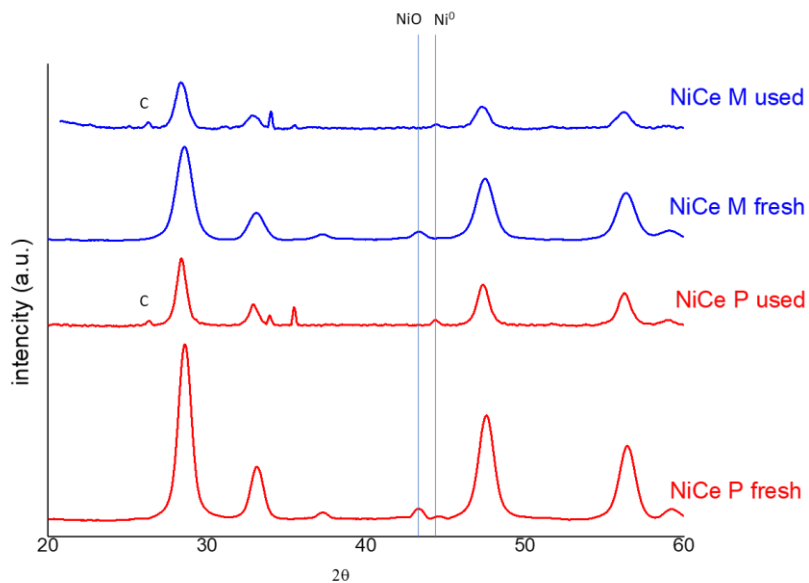


Figure 2.7 XRD patterns of fresh and used catalysts.

The patterns of used samples present reflections attribute to carbon species, at 2θ 26.4 °[116], probably with a graphite-like structure. For the used catalysts, the crystal particle size of CeO₂ increases, as reported in Table 2.2, and the reflections attributed to metallic Ni appear at 2θ 44.5 °, while those of NiO disappear. This evidences that the reaction mixture allows the reduction to the metal phase, thus activating the catalysts for the reaction.

Table 2.2 Particle size of CeO₂, NiO and Ni calculated via Scherrer equation from reflections 28, 43.7, 44 ° respectively.

Samples	CeO ₂ particle size (nm)	NiO particle size (nm)	Ni particle size (nm)
NiCe P fresh	9	14	-
NiCe P used	11	-	22
NiCe M fresh	7	9	-
NiCe M used	10	-	10

Moreover, another important parameter is the dimension of Ni particles. Table 2.2 summaries CeO₂, NiO and Ni crystallite sizes of fresh and used catalysts. As already seen for the oxide phase, the particle size of Ni is bigger for the NiCe P sample than for NiCe M. It should be noted, however, that the XRD analyses were carried out with the samples discharged after 5 h under reaction conditions, which may have been sintered along this period. It is difficult to determine the size of the just reduced particles. Indeed, to determine the possible sintering effect, reactivation of used catalysts was carried out, followed by a second catalytic test. Figure 2.8 compares ethanol conversion and hydrogen yield on fresh and used catalysts for both materials. After the regeneration in air, the initial H₂ yield on NiCe P, the most active one, was 10 percentage points lower than on the fresh sample and decreased similarly down to 17 % after 5 h of the reaction (instead of 30% for the fresh sample). In this way, it is noteworthy that catalyst regeneration did not allow its complete reactivation. This means that the hypothesis of possible sintering of the catalyst is highly probable. In the case of NiCe M, it was completely reactivated after the regeneration step, as the curve of ethanol conversion of the regenerated sample is almost totally

overlapping the fresh one. Considering H₂ yield, a slight faster deactivation is visible, with no H₂ production after just 2 h.

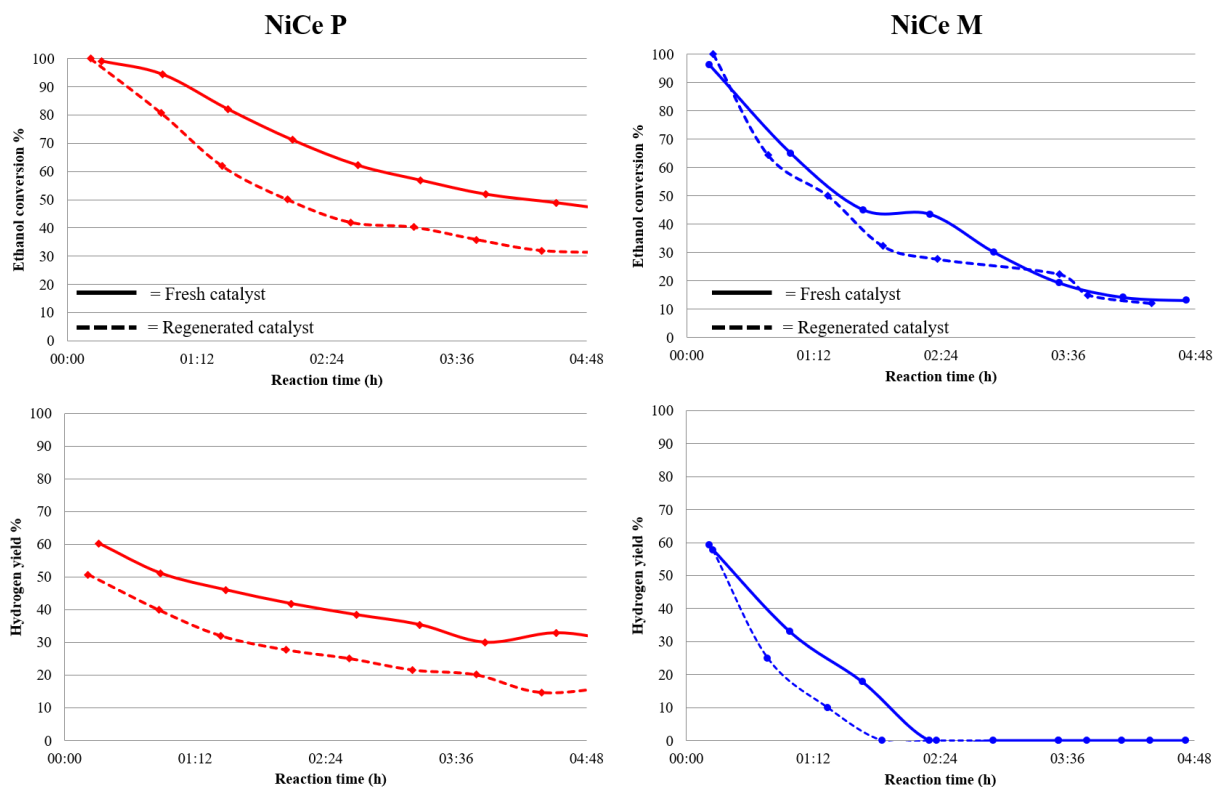


Figure 2.8 Ethanol steam reforming on fresh (straight lines) and reactivated (dotted lines) catalysts. Ethanol conversion and hydrogen yield vs reaction time.

As a matter of fact, the causes of catalysts deactivation are quite different. In fact, the catalyst prepared via microemulsions, despite the faster deactivation with time, is completely reactivated during the regeneration step. Therefore, one can hypothesize that the high amount of carbon deposits over its surface may have caused this behaviour. On the contrary, the catalyst prepared via precipitation is more stable over time, but it cannot be fully regenerated in air. Hence, sintering of the active phase has probably occurred. As already seen by TPR technique, NiCe P presents two peaks at lower temperature than the temperature peak of, suggesting a lower interaction between support and active phase.

2.3 Conclusions

In this Chapter, the effect of the preparation method on nickel ceria-based catalysts has been evaluated. Precipitation and microemulsion synthesis were studied. As expected, the microemulsion approach allows preparing material with small NiO dimensions and a defined interaction between NiO and support that, in comparison with the precipitated material, is stronger. At the same time, the sample prepared via precipitation has a high surface area, a well define spherical shaped particles and a high crystallinity. Therefore, the preparation method strongly affects the structural and chemical properties of those materials. Considering their catalytic performances in ethanol steam reforming, it was observed that the catalyst prepared via precipitation shows higher catalytic activity and stability in time, while the catalyst prepared via microemulsion deactivates faster. Nevertheless, after the regeneration test, NiCe P sample does not fully regain its properties, while NiCe M is completely reactivated. The causes of catalysts deactivation are quite different. In NiCe P, the interaction between the active phase and the support, the high degree of crystallinity and the high surface area allowed a good activity in ESR with 30 % of hydrogen yield after 5 hours of reaction. Therefore, the cause of the deactivation in this material is precisely due to the sintering of the nickel particles. On the contrary, NiCe M has a strong interaction between active phase and support which preserves the material from sintering. However, the reduced surface area and the low degree of crystallinity led to a rapid deactivation of the material caused by coke deposition.

As a result of this evaluation, the microemulsion approach was abandoned due to the poor catalytic performances of the material and the high cost of the synthetic approach. Therefore, in the following studies, the most traditional method of precipitation has been employed.

Chapter 3 . Increase of ceria redox ability by lanthanum addition on Ni based catalysts

The effects of promoter addition in Ni/CeO₂ catalysts were investigated using lanthanum. The influence of synthetic procedures, namely impregnation or co-precipitation of lanthanum and cerium oxide, were evaluated. Materials were analysed by BET, AAS, DRIFT-MS, TPR, OSC, XRD and SEM-EDX. Samples were tested in Ethanol Steam Reforming (ESR). Both lanthanum-promoted samples exhibited a higher stability in time than non-promoted catalyst. Nonetheless, catalytic behaviour is strongly affected by the introduction method. TPR, OSC and XRD analyses showed that co-precipitation method allowed the best interaction between ceria and lanthana, leading to an increased redox ability and best catalytic performances as a result. A catalyst with a support prepared via co-precipitation method showed ethanol conversion of 90% and hydrogen selectivity higher than 70% even after 60 hours of reaction. The results reported in this chapter are published as: “*Increase of Ceria Redox Ability by Lanthanum Addition on Ni Based Catalysts for Hydrogen Production*”, C. Pizzolitto, F. Menegazzo, E. Ghedini, G. Innocenti, A. Di Michele, G. Cruciani, F. Cavani, M. Signoretto, ACS Sustainable Chem. Eng. 6 (2018) 13867-13876.

3.1 Experimental

3.1.1 Catalysts preparation

- *Support preparation method:* Ceria support (denoted as C) was synthesized by precipitation from $(\text{NH}_4)_2\text{Ce}(\text{NO}_3)_6$ (Sigma Aldrich) by urea at 100 °C in aqueous solution. The solution was mixed and boiled for 6 h at 100 °C, the precipitate was washed in boiling deionized water and dried at 110 °C for 18 hours. The material was then calcined in air flow (30 mL/min) at 550 °C for 3 hours.
- *Introduction of lanthanum via incipient wetness impregnation:* the support prepared via promoter incipient wetness impregnation was denoted as *LaCimpr*. The proper amount of $\text{La}(\text{NO}_3)_3 \cdot 6\text{H}_2\text{O}$ was added to the calcined support in order to obtain 5 wt% of lanthanum on the final catalyst. The material was dried at 110 °C in the oven and then calcined in flowing air (30 mL/min) at 550 °C for 3 hours.
- *Introduction of lanthanum via coprecipitation:* the support prepared via co-precipitation of promoter was denoted as *LaCcopr*. Also in this case, the proper amount of $\text{La}(\text{NO}_3)_3 \cdot 6\text{H}_2\text{O}$ was dissolved together with the support precursor to obtain 5 wt% of lanthanum on the final catalyst and the synthetic methodology was the same of non-promoted ceria.
- *Introduction of nickel oxide:* the metal introduction on the support was performed by incipient wetness impregnation with a proper amount of $\text{Ni}(\text{NO}_3)_2 \cdot 6\text{H}_2\text{O}$ aqueous solution in order to obtain 8 wt% of nickel on the material. After drying at 110 °C for 18 hours, calcination was performed under air flow (30 mL/min) at 550 °C for 4 hours.

The samples were labelled:

1. NiC
2. NiLa*Cimpr* introduction of lanthanum via impregnation method.
3. NiLa*Ccopr* introduction of lanthanum via co-precipitation method.

3.1.2 Catalyst Characterisations

N₂-physisorption and TPR measurements were carried out using the same methods reported in section 2.1.2 of Chapter 2.

Nickel amount was determined by atomic adsorption spectroscopy (AAS) after microwave disaggregation of the samples (100 mg) using a Perkin-Elmer Analyst 100.

DRIFT-MS analyses were carried out in the Lab. of Prof. Fabrizio Cavani in the University of Bologna. IR apparatus Bruker Vertex 70 equipped with a Pike DiffusIR was used. Spectra were recorded using a MCT detector after 128 scans and 4 cm⁻¹ resolution. The mass spectrometer was an EcoSys-P from European Spectrometry Systems. The samples were pretreated at 500 °C in He flow (8 ml/min) for 60 min, and then the bare catalyst IR spectra were collected every 50 °C from 500 °C to room temperature (RT). Afterwards, ethanol was fed at 0.6 μL min⁻¹ and, as the ethanol mass signal started to raise, the RT spectrum was recorded. Sample temperature was then increased by 5 °C/min and spectra were collected every 50 °C. The adsorbed species spectra were obtained at each temperature by subtracting the catalyst spectrum at the proper temperature.

Oxygen Storage Capacity (OSC) analyses were carried out in the same lab-made equipment used for TPR. 50 mg of sample were pre-treated in H₂ flow (40 mL/min) until 550 °C and maintained at this temperature for 1 hour. Then the sample was purged in He flow and cool down to 25 °C. Pulses of a 5% O₂/He mixture were carried out until TCD signal saturation.

X-ray powder diffraction (XRD) patterns were measured in the Lab. of Prof. Giuseppe Cruciani at the University of Ferrara by a Bruker D8 Advance diffractometer equipped with a Si(Li) solid state detector (SOL-X) and a sealed tube providing Cu K radiation. The Rietveld refinement method as implemented in the Bruker TOPAS programme was used to obtain the refined unit cell parameters, crystal size, and the quantitative phase analysis for the supports and metal phases in the samples. The crystal size determination is achieved by the integral breadth based calculation of volume weighted mean crystallite sizes assuming intermediate crystallite size broadening modelled by a Voigt function. The samples were reduced in H₂ flow for 1 h at 550 °C before the analysis and then passivated in air flow at 25 °C.

FE-SEM images were carried out in the Lab. of Dr. Alessandro Di Michele at the University of Perugia using a Field Emission Gun Electron Scanning Microscopy LEO 1525 ZEISS, after metallization with Chromium. The images were acquired by InLens detector while elemental composition was determined using Bruker Quantax EDS (resolution of 2 nm at 20 kV).

3.1.3 Catalytic tests

The catalytic tests were performed with a PID microactivity-Effi reference reactor (Process Integral Development Eng&Tech) coupled to a gas-chromatograph (HP 6890), Scheme 3.1. Microactivity-Effi reactor is an automatic and computerized catalytic reactor which includes valves and process layout inside a hot box to avoid possible condensation of volatile products, while also preheating the reactants efficiently. Using a HPLC pump (Gilson 303) the mixture of water and ethanol (molar ratio 6:1) was flowing and helium was used as carrier. The total amount of molar flow was 0,615 mol/h considering a molar ratio composition of 91,75% of He, 1,20 % of Ethanol and 7,23 % of Water. The typical reaction temperature was 550 °C. Preliminary tests were performed without the catalyst and using the bare supports. No evident ethanol conversion has been observed in these experiments at the typical reaction temperature. To have a homogenous catalyst, tablets of samples were prepared and pressed and grained to obtain the ideal grain size range (0,3-0,4mm). Afterwards the catalyst (150 mg) was mixed with siliciumcarbide (SiC, VWR, ratio catalyst:SiC=1:4 by volume). The catalysts were not reduced before reaction. This allows skipping one step, turning out to be more economically convenient for industrial applications. In fact, the catalyst is reduced in situ by the reactive mixture as it was demonstrated by DRIFT technique[115]. After the analysis, conversion of ethanol, product distribution and hydrogen yield were calculated using the following equations:

Conversion of ethanol:

$$\text{Conversion (\%)} = 100\% - (f_{\text{out}}(\text{EtOH}) / f_{\text{in}}(\text{EtOH})) * 100\%$$

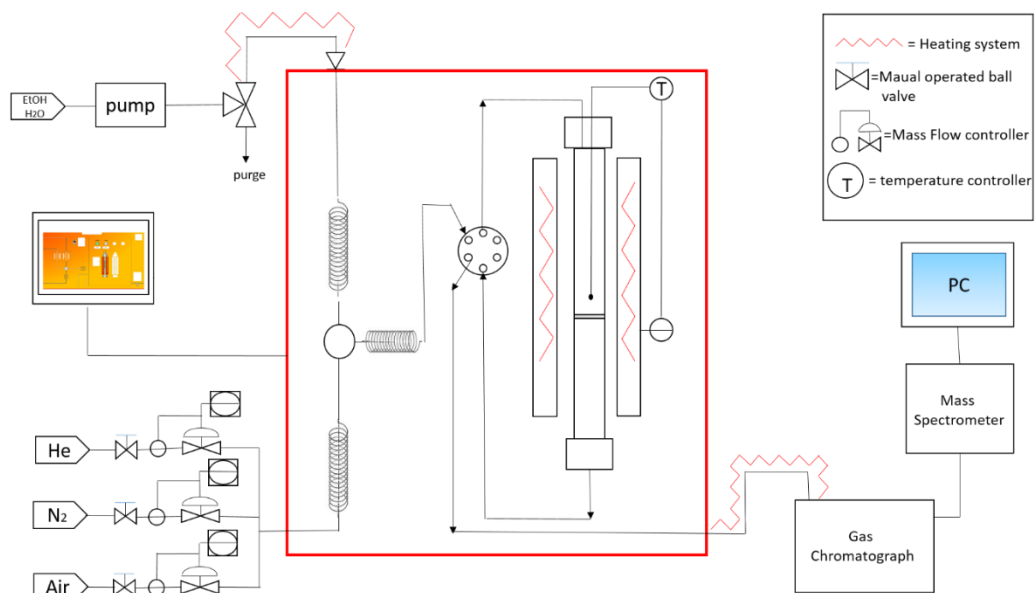
Product distribution:

$$\text{Product distribution (\%)} = (f_{i \text{ out}}) / (\sum [f_{i \text{ out}}]) * 100\%$$

Hydrogen yield:

$$\text{Hydrogen yield (\%)} = (f_{\text{H}_2 \text{ out}}) / (6 * f_{\text{EtOH in}}) * 100\%$$

where f is the flow in mol/min.



Scheme 3.1 Lab set-up for ESR catalytic tests

3.2 Results and Discussion

3.2.1 Catalyst characterisations

Two synthetic methodologies were selected to investigate if lanthanum introduction method can affect physicochemical properties, activity and stability of the final catalyst. In particular, lanthanum impregnation over ceria (NiLaCimpr) and lanthanum co-precipitation together with ceria (NiLaCcopr) were studied. First, preliminary characterizations were performed. N₂ adsorption-desorption measurements were carried out in order to quantify the specific surface area and pore size distribution of the catalysts and in order to evaluate the possible effects of lanthanum addition on surface properties of final material. This aspect is of crucial importance in heterogeneous catalyst since it is known that a high surface area greatly improves the dispersion of the active phase and the interaction between metal and reagents [117]. Figure 3.1 represents the adsorption-desorption isotherms and BJH distributions of NiC, NiLaCimpr and NiLaCcopr catalysts, while Table 3.1 summarizes the corresponding data.

Table 3.1 Specific surface area, pore size distribution and pore volume for NiC, NiLaCimpr and NiLaCcopr catalysts.

	NiC	NiLaCimpr	NiLaCcopr
Surface area (m ² /g)	106	66	76
Mean pore size (nm)	6	5	4
Pore Volume (cm ³ /g)	0.10	0.02	0.03

The three samples exhibit a IV-type isotherm, according to IUPAC classification, with the characteristic hysteresis loop typical of mesoporous materials. For NiC catalyst, this loop is located at higher V_{ads} values than for NiLaCimpr and NiLaCcopr, indicating the higher surface area.

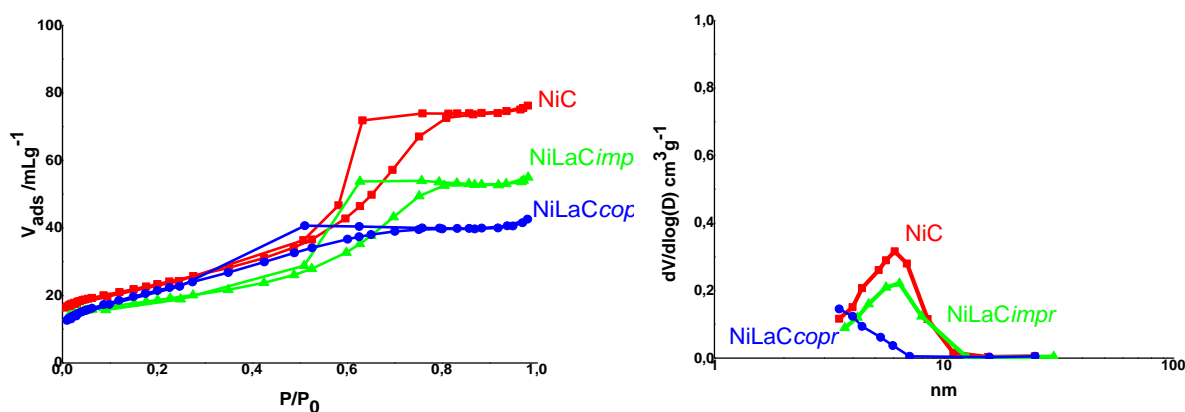


Figure 3.1. N₂ adsorption-desorption isotherms (left) and BJH curves (right) of NiC (■), NiLaCimpr (▲) and NiLaCcopr (●) catalysts.

Both samples containing lanthanum have lower surface area values, calculated by BET method, and lower pore volumes than non-doped ceria catalyst. Such result is in agreement with data obtained for lanthanum promotion on SBA-15 [118]. The decrement in surface area of ceria material after the addition of lanthanum can result from two different effects. In the case of NiLa*Cimpr* sample, lanthanum is introduced into CeO₂ after the calcination process in which ceria structure is already built. For this reason, the shape of the hysteresis is the same of the not promoted sample and the lower surface area is the only difference. This decrement is due to the block of pore by the introduction of lanthanum and nickel via impregnation method. On the contrary, in the case of NiLa*Ccopr*, lanthanum and ceria are co-precipitated together. This means that the structure of ceria is influenced by the presence of lanthanum during precipitation. For this reason, both the shape and the position of the hysteresis are different from the previous catalysts.

Atomic adsorption analyses were carried out in order to quantify the effective nickel amount in the catalysts. As expected, since nickel was introduced by incipient wetness impregnation, all catalysts present the nominal metal amount, which is 8 wt %.

3.2.2 Reactivity tests

ESR tests were conducted monitoring reaction mixture for 16 hours. Figure 3.2 reports ethanol conversion against time of reaction for the three catalysts. The corresponding products distribution, ethanol conversions, and hydrogen yields after 16 hours of reaction are reported in Table 3.2. Figure 3.2 (section b) reports also the stability test of 60 hours for the best sample, which is NiLaCcopr catalyst.

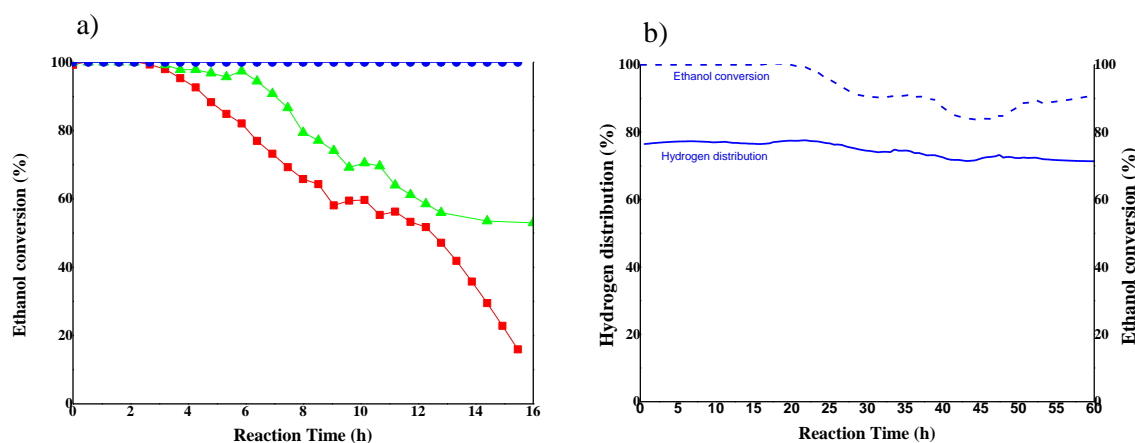


Figure 3.2 Ethanol conversion for NiC (■), NiLaCimpr (▲) and NiLaCcopr (●) (section a); Stability test of NiLaCcopr catalyst for 60 hours (section b).

It should be highlighted that none of the three catalysts shows carbon monoxide in the products (Table 3.2). This result has a crucial importance: the absence of CO means that water gas shift reaction is favoured ($\text{CO} + \text{H}_2\text{O} \rightleftharpoons \text{CO}_2 + \text{H}_2$); in fuel cell applications, CO is commonly a poison, even if SOFCs are more tolerant to this gas because they can oxidize it to CO_2 at the anode ($\text{CO} + \text{O}^{2-} \rightleftharpoons \text{CO}_2 + 2\text{e}^-$). At the same time, at low temperature CO could lead to coke formation, through the Boudouard reaction ($2\text{CO} \rightleftharpoons \text{C} + \text{CO}_2$). For this reason, direct oxidation of CO to CO_2 in SOFCs is important to limit coke deposition [119] and therefore a low or even null CO production is a promising result. Considering catalytic behaviour over time (Figure 3.2), non-doped NiC catalyst presents a steady decrease in ethanol conversion, reaching the value of 25 % after 16 hours of reaction. The sample presents a high hydrogen yield only for the first hours of reactions, showing a gradual decrease from 70 % to 20 % through 16 hours. As it is possible to see from the catalytic results, by lanthanum incorporation into ceria, there is an increase of both hydrogen yield and ethanol conversion after 16 hours of reaction. However, catalytic results strongly indicate that preparation method deeply affects the development of a stable and active catalyst: the same promoter does not lead to the same catalytic performance. The best one was obtained when lanthanum oxide was added via co-precipitation method (Figure 3.2 and Table 3.2). Such sample maintains an ethanol conversion of 100 % for at least 16 hours of reaction, due to the experimental conditions used.

Table 3.2 Hydrogen yield, ethanol conversion and product distribution of Ni-Ce, Ni-La-Ce and co- Ni-La-Ce after 16 hours of reaction.

	NiC	NiLaCimpr	NiLaCcopr
EtOH conv (%)	33	55	>99 %
H ₂ yield (%)	18	37	70
H ₂ distribution (%)	70	69	76
CH ₄ distribution (%)	2	10	3
CO ₂ distribution (%)	28	21	21
CO distribution (%)	0	0	0

Total conversion is not significantly relevant to understand the behaviour of a catalyst, so to further prove the increment in the redox effect and, consequently, in the stability of NiLaCcopr catalyst, a prolonged test was performed (60 hours). In Figure 3.2 (section b) ethanol conversion and hydrogen distribution of NiLaCcopr are presented. It is possible to see that, during this prolonged time on stream, conversion > 99 % is maintained for first twenty hours only; thereafter, a small and gradual decrease takes place. Therefore, a light deactivation effect is shown, despite the conversion is still 90 % at the end of the sixtieth hour. At the same time, hydrogen distribution is almost constant for all the time on stream.

Another important aspect is the reducibility of the catalysts in the reaction environment. In order to have a deep knowledge of the interaction between ethanol and the catalytic surface, DRIFT-MS technique was performed.

Figure 3.3 shows DRIFTS spectra of pure support (C), NiC and NiLaCcopr recorded while exposing the catalysts continuously to pure ethanol at different temperatures. The spectrum of pure support is used as reference and a more deepened description of the spectrum it is reported in the appendix (Appendix A1). In the case of NiC and NiLaCcopr catalysts, not significant differences are visible at RT, and even the trends shown when the temperature was raised were similar in the two cases. Indeed, bands differed only slightly in terms of wavenumber ($\Delta\nu < 5 \text{ cm}^{-1}$) for the two samples. As far as NiC sample is concerned, ethanol was adsorbed on the catalyst surface at RT as both undissociated molecule and ethoxide [120,121]. The presence of H-bonded ethanol is corroborated by two broad bands, one from 3100 to 3500 cm^{-1} and the other centered at 1236 cm^{-1} . The ethoxy is adsorbed in two different modes, as bidentate (1060 cm^{-1}) and monodentate (1104 cm^{-1}) [122]. The bands at 2970, 2926, 2898, 2869, 1445 and 1381 cm^{-1} are related to ethoxy $\nu(\text{CH}_3)$, $\nu(\text{CH}_2)$, $\nu(\text{CH}_2)$, $\nu(\text{CH}_3)$, $\delta(\text{CH}_3)$ and $\delta(\text{CH}_3)$, respectively. The catalyst terminal OH group were characterized by the negative $\nu(\text{OH})$ at 3660 cm^{-1} . As far as the band at 1236 cm^{-1} is concerned, the assignation is not

unambiguous since the other H-bonded ethanol characteristic band is detected up to 150 °C. Ethanol was continuously fed, hence, it might be reasonable to hypothesize that some un-dissociated ethanol might interact with the catalyst surface even at higher temperatures but it is possible to find the η^2 -acetaldehyde $\nu(\text{C-O})$ at the same wavenumber [120]. The presence of the latter is corroborated, for NiLaCopr sample, by the shoulder at 1150 cm^{-1} assignable to η^2 -acetaldehyde $\nu(\text{C-C})$ visible even at RT. Unfortunately, it is not possible to distinguish unambiguously any shoulder in the NiC spectra (nor at RT neither at higher temperatures) and hence for this sample the assignation can be only uncertain. At 150 °C, the acetates $\nu\alpha\sigma(\text{COO})$ and $\nu\sigma(\text{COO})$ started to be completely detectable at 1562 cm^{-1} and 1429 cm^{-1} , respectively. The acetate band intensities increase raising the temperature and at 200 °C the acetate $\delta(\text{CH}_3)$ appeared at 1338 cm^{-1} [123]. A further temperature increase led to the appearance of some bands due to bridged and bidentate carbonates (928 cm^{-1} and 1021 cm^{-1} , respectively) [124].

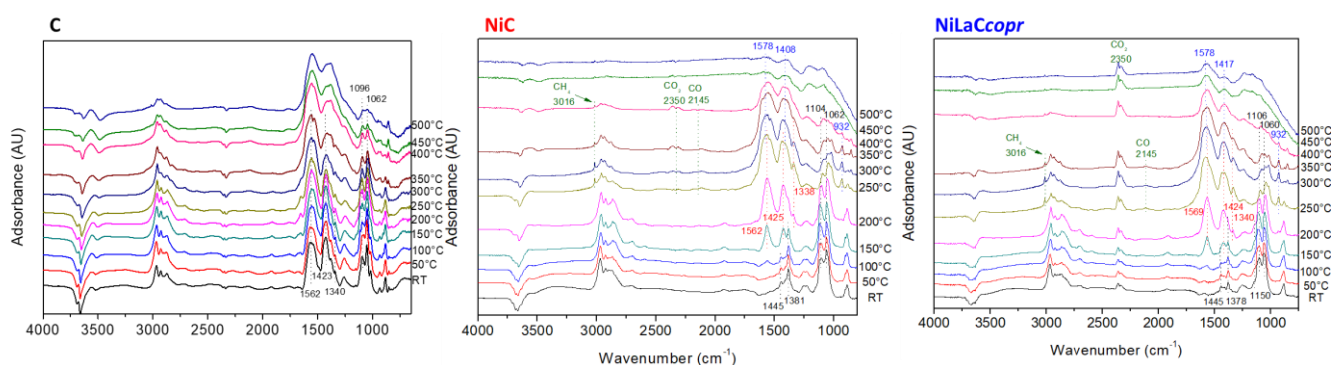


Figure 3.3 DRIFTS analyses of Ce, Ni-Ce and co-Ni-La-Ce samples feeding ethanol at different temperatures.

The broadening of COO acetates bands is due to their convolution with the carbonates ones until 400 °C. From 250 °C to 400 °C three gas phase bands were detected at 3018 cm^{-1} , 2338 cm^{-1} and 2140 cm^{-1} assignable to CH₄, CO₂ and CO respectively. In correspondence of these bands appearance, the MS experiment showed a maximum in CO, CH₄, H₂ and acetaldehyde (the MS trends are reported in Figure A.2 in the Appendix). Xu *et al.* [123] detected a decrease of the acetate band intensities and observed the disappearance of ethoxy species at high temperatures. In our case, we do not see such a decrease in acetate or ethoxy surface species due to their continuous formation from the ethanol stream. It is also important to notice that Xu *et al.* correlated NiO reduction by ethanol with high temperatures (250 °C-400 °C) using XRD analysis. Moreover, in those experiments the spectrum base line underwent to a dramatic drop down under 1500 cm^{-1} from 400 °C to 500 °C, associated to NiO reduction [125]. It is possible to state that ethanol reduces NiO ($\text{CH}_3\text{CH}_2\text{OH} + \text{NiO} \rightarrow \text{CH}_3\text{CHO} + \text{Ni}^0 + \text{H}_2\text{O}$) since no H₂ was produced before 250 °C. In fact, its production started along with the vanishing of η^2 -acetaldehyde peaks. Indeed, CO and CH₄ showed an absolute maximum between

250 °C and 350 °C since they are the products of acetaldehyde decomposition, whose MS trend did not show a definite maximum. The fact that water trend reached its minimum during the NiO reduction, while it should be coproduced, might be due to the catalyst H₂O adsorption as indicated by the small broad band clearly detected at 3579 cm⁻¹ from 250 to 350 °C associated with the formation of new O-H bond. Furthermore, the water release decrement, in this temperature range, might be due to its consumption in the steam reforming reaction that started at 250 °C as shown by the ethanol MS trend. The water trend increases after 350 °C might be due to the release of water by the catalyst surface as suggested by the OH band diminution. Further information given by the MS analysis are reported in the Appendix part. Overall, it was possible to demonstrate that in the reaction conditions herein reported a catalyst pre-reduction is not necessary, since ethanol, acting as a reducing agent, is able to rapidly activate the catalytic system.

3.2.3 Influence of lanthanum on nickel reducibility

TPR analyses were performed in order to identify how lanthanum influences NiO and ceria reducibility (Figure 3.4, continuous and dotted lines respectively). Focusing on catalysts' TPR profiles (continuous line), NiC's profile shows a peak centred at 260 °C which is ascribable to the NiO species that weakly interact with ceria, and another one at 340 °C, due to more strongly interaction between them. It can be underlined that the introduction of lanthanum via impregnation method leads to a shift of the peaks to higher temperatures (by 20 °C and 40 °C respectively), indicating an increase in metal-support interaction strength. On the contrary, lanthanum introduction via co-precipitation method slightly affects the interaction strength between ceria and NiO. Therefore, no evident differences for this sample are visible. Moreover, TPR analyses are even more important for the interpretation of ceria reducibility. For this reason, H₂-TPR analysis of bare supports have been performed (Figure 3.4 underlined line). Two different peaks can be observed: the first one, centred around 500 °C, is associated with the reduction of surface ceria from Ce⁴⁺ to Ce³⁺; the second peak, located around 800 °C is connected with the reduction of the bulk support [126,127]. Since the reaction must be performed at 550 °C, the first peak assumes a fundamental importance to understand the reducibility of the system under reaction conditions. As regards the lanthanum doped samples, it is possible to underline a shift, for both peaks, to lower temperatures. Such shift is an indication that the introduction of lanthanum makes ceria more reducible, which can help to improve oxygen mobility during the reforming reaction, as reported by Dong *et al.* [128]. Such difference in ceria reducibility is the first tool to understand the catalytic results and explain the higher stability of lanthanum doped samples. Mobile oxygen species take part to the oxidation of carbon species, limiting coke deposition over catalyst surface and implementing its stability during the reaction.

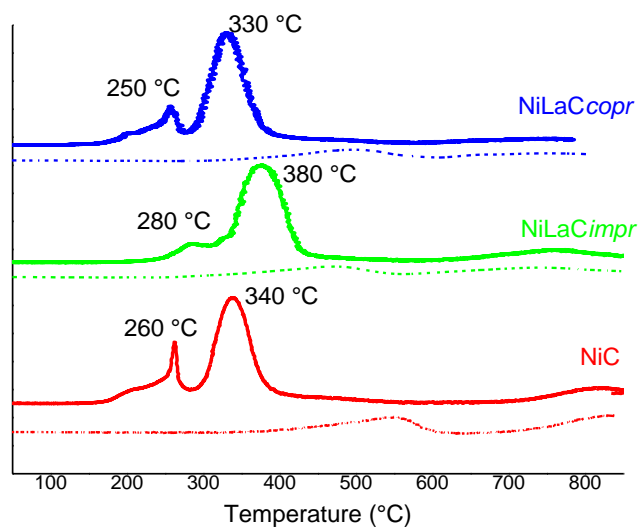


Figure 3.4 TPR profile of pure supports (underline lines) and NiC, NiLaCimpr and NiLaCcopr (continuous lines)

3.2.4 Influence of lanthanum on catalyst structure

FE-SEM analyses of fresh catalysts and the corresponding EDX analyses are shown in Figure 3.5 (left). It is possible to affirm that nickel is well and homogeneously dispersed on ceria surface of the three samples as it's visible in the nickel mapping reported in the top part of Figure 3.6.

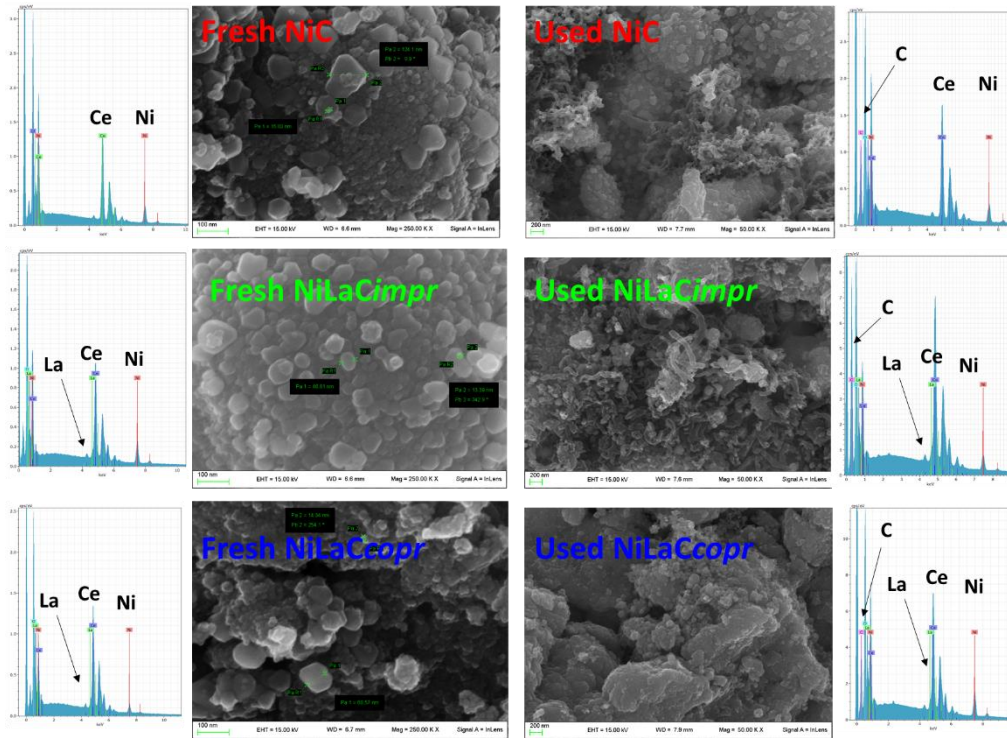


Figure 3.5 SEM and EDX analyses of fresh (left) and used (right) ceria supported catalysts.

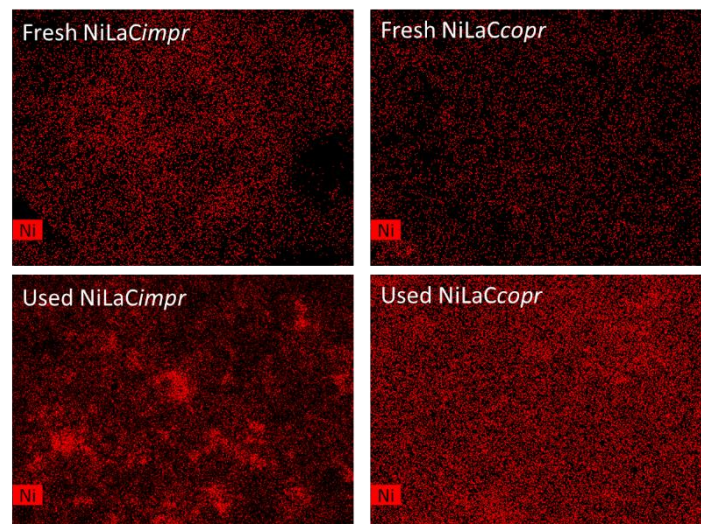


Figure 3.6 Representative Nickel mapping images by EDX-SEM of Ni-La-Ce fresh and used (left) and co-Ni-La-Ce fresh and used (right)

The dimension of ceria particles is around 90 nm. A rough determination of nickel particle size shows that the three samples exhibit nickel nanoparticles in the range 10-15 nm. XRD analyses were carried out in order to identify the ceria crystal phase, the nickel phase and to determine more carefully the

nickel mean size (Figure 3.7). These analyses were conducted in the reduced samples in order to get as much closer to reaction conditions as possible, despite the reduction of NiO is carried out by the oxidation of ethanol to acetaldehyde in the reaction environment, as it has been demonstrated by DRIFT technique. In the three catalysts, a fluorite-type structure of ceria is present with characteristic peaks at 2 theta 28 °, 33 °, 47 °, 56 ° and 59 ° associated with (111), (200), (220), (311) and (222) of cubic phase, respectively [129,130].

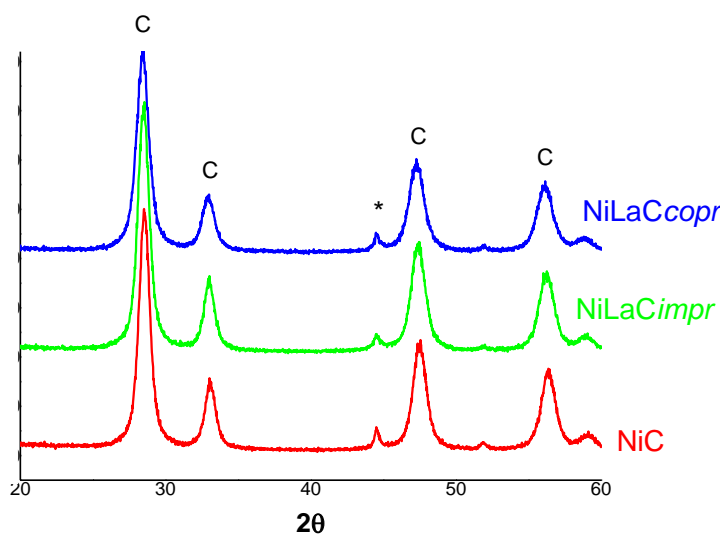


Figure 3.7 XRD analysis of reduced ceria supported samples (C is the ceria crystal phases and * is Ni⁰ species).

The characteristic peak at 2 theta 43,4 ° and 52,0 ° indicates that nickel is present in its metallic phase and they are respectively associated with (111) and (200) Miller Indexes of fcc nickel [131]. By means of the Rietveld method, it was calculated the mean size of Ni⁰: 17 nm for NiC, 10 nm for NiLaCimpr and 14 nm for NiLaCcopr. Lanthanum in this case influences the nickel particle size, leading to a slight decrement of its dimension. Usually, in this kind of reactions, the smallest is the size, the highest is the catalyst stability [132,133]. In fact, the most active catalysts for this reaction are those promoted with lanthanum, which have a smaller nickel particle size than non-doped sample.

Furthermore, the XRD technique was used to analyse the ceria cell parameters to investigate the lanthanum effect on ceria support. Table 3.3 reports cell parameters for the catalysts where a_0 and V_0 refer to the unit-cell constant and the unit-cell volume, respectively, of the NiC sample. For the two lanthanum-doped samples, it can be seen an increase in unit-cell constant and unit-cell volume, in particular for the catalyst synthesized with the co-precipitation method. The increase in the unit-cell volume can be taken as a strong evidence that lanthanum is fully hosted as La³⁺ ions (ionic radii 1.16 Å) replacing Ce⁴⁺ ions (ionic radii 0.97 Å) in the ceria lattice. This is also in perfect agreement with the absence of any diffraction peak related to metallic lanthanum or lanthanum oxide(s) in the XRD patterns of NiLaCimpr and NiLaCcopr samples (see Figure 3.7). A likely explanation is that the

substitution of two Ce^{4+} with two La^{3+} atoms can be balanced with an oxygen vacancy. This could bring to an increase in redox ability. This property could improve the ability to oxidize carbonaceous species on the surface, limiting the deactivation due to coke formation and stabilizing the catalyst. In fact, we have shown that *NiLaCcopr* is the best performing catalyst and presents a very good stability.

Table 3.3 Variation of lattice parameters of the catalysts and oxygen storage capacity of supports.

		Ni-Ce	Ni-La-Ce	co-Ni-La-Ce
XRD	V/V ₀	1	1,006	1,012
	a/a ₀	1	1,002	1,004
		Ce	La-Ce	co-La-Ce
OSC	mmol O ₂ /g	0,13	0,58	0,77

The redox ability of a material can be accurately assessed using the Oxygen Storage Capacity method (OSC). In this case, the three supports, and not the final catalysts, were analysed. The method allows understanding the capacity of support in adsorbing oxygen, and this is directly proportional to its redox abilities. Ceria adsorbed the lowest amount of oxygen (mmol of O₂ per grams), while there is an increment of O₂ adsorption passing from the impregnated support (*LaCimpr*) to the co-precipitated one (*LaCcopr*) (Table 3.3). This characterization technique demonstrates the effects on ceria redox ability of both lanthanum addition and synthetic methodology. In fact, promoter addition, by co-precipitation particularly, leads to an increase of OSC, which means an increase in ceria redox ability and therefore an increase in stability towards coke poisoning.

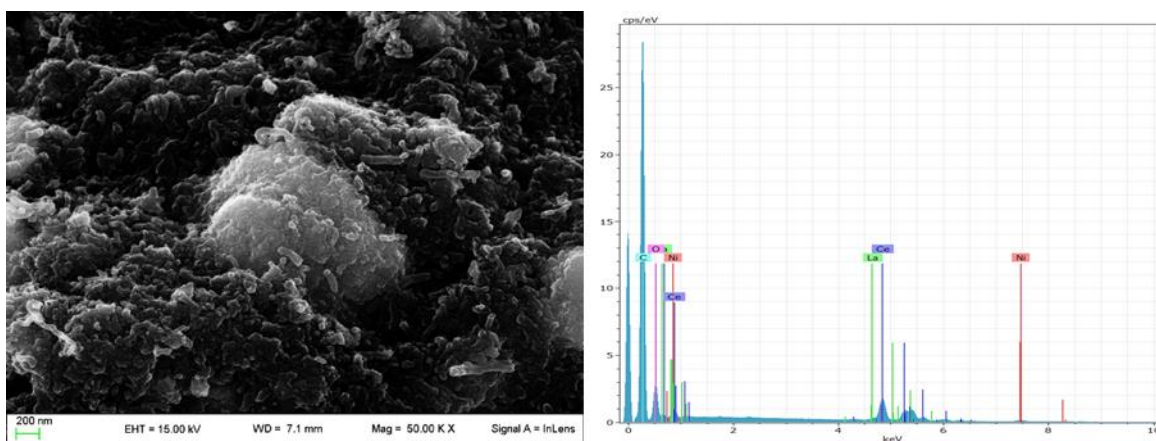


Figure 3.8 SEM and EDX analyses of *co-Ni-La-Ce* spent after 60 hours of reaction.

To further confirm the results, SEM analyses of used catalyst have been made. Figure 3.5 (right) shows SEM images and EDX analyses of catalysts after 16 hours of reaction, while Figure 3.8 reported SEM image and EDX analysis of NiLaCcopr after 60 hours of reaction. Looking at Figure 3.5, the differences between used samples are evident. Used NiC surface is completely covered by small nanotubes, while used NiLaCimpr shows few nanotubes with diameter size around 44 nm. As for NiLaCcopr catalyst, no nanotube species are detected on the surface of used sample, and only small percentage of carbonaceous species (5-6%) is depicted by EDX analysis. The same catalyst was tested for 60 hours and, looking at SEM and EDX analyses of spent catalyst (Figure 3.8) it is possible to observe the presence of coke on the catalyst surface. However, coke does not cover the whole surface and it is still possible to observe the Ni nanoparticles. This could explain the good activity of the catalyst after 60 hours of reaction but also its partial deactivation.

Furthermore, Figure 3.6 represents nickel mapping images of used promoted samples (after 16 hours of reaction) in order to highlight the reasons for their different deactivation. Used NiLaCcopr presents a homogeneous distribution of nickel particles while for used NiLaCimpr, sporadic particle agglomeration is evident. As reported in introduction, lanthanum insertion into ceria could enhance the support redox ability and both mechanical and thermal stability. For NiLaCimpr catalyst, the preparation method strongly affects its mechanical and thermal stability and the lesser La³⁺ substitution in ceria lattice gives lower redox ability at the system in comparison with NiLaCcopr. The combination of these two effects does not allow the stabilization of nickel particle on the surface and, as it is evident for used NiLaCimpr in Figure 3.6, nickel sintering is visible. This result agrees with the data previously discussed.

3.3 Conclusions

The effects of lanthanum addition in nickel ceria samples were investigated in order to find a stable, active and resistant catalyst for ethanol steam reforming. This chapter highlights how lanthanum introduction method strongly affects the catalytic performances. Lanthanum co-precipitation guarantees a stronger interaction between La^{3+} and Ce^{4+} than impregnation, and this is evident by Rietveld unit cell refinements. This strongest interaction leads to the highest oxygen mobility in ceria bulk, as observed by OSC analysis and TPR. Therefore, it was observed how this property has a beneficial effect on the oxidation of carbonaceous species during the reaction and leads to a prolonged stability of the catalyst during the reaction. In fact, lanthanum added via co-precipitation leads to the best performances, 100 % ethanol conversion and 70 % hydrogen distribution after 16 hours of reaction. No nanotube species are depicted in SEM images of used catalyst. Moreover, no nickel sintering is visible. In addition, for this catalyst it was performed a prolonged test. It is found that, after 60 hours, ethanol conversion is still 90% and hydrogen distribution is higher than 70%. Such catalytic system, based on nickel, ceria and lanthanum, could be very interesting also for many other catalytic applications, such as glycerol steam reforming and dry reforming.

Chapter 4. Limiting Coke deactivation of Ni-ZrO₂ in ethanol steam reforming by promoting effect of lanthanum

In this chapter, promoting addition of lanthanum on Ni-zirconia catalyst was evaluated. As in the previous chapter, strong attention was focused on the lanthanum introduction method: incipient wetness impregnation and co-precipitation of the promoter with support were studied. Promoting effect of lanthanum was evident; higher ethanol conversion and hydrogen yield were obtained. Best catalytic results were obtained with the catalyst prepared via promoter's impregnation that, according to CO₂-TPD technique, was material with the most basic features. DRIFT analysis was used to understand the effect of basic sites in the reaction pathway. Indeed, according to SEM analysis and Raman spectroscopy, higher stability and activity of lanthanum impregnated sample were related to its higher basicity that suppressed unwanted reactions such as ethylene formation and coke polymerization. The results reported in this chapter have been submitted as "*Limiting Coke deactivation of Ni-ZrO₂ in ethanol steam reforming by promoting effect of lanthanum*" C. Pizzolitto, F. Menegazzo, E. Ghedini, G. Innocenti, A. Di Michele, M. Mattarelli, G. Cruciani, F. Cavani and M. Signoretto*.

4.1 Experimental

4.1.1 Catalyst preparation

- *Support preparation method:* Zirconia support (Z) was prepared by precipitation from ZrOCl₂·8H₂O (Sigma Aldrich) with NH₃ at constant pH= 8.5 and then aged at 90 °C for 20 hours. The precipitate was washed and dried at 110 °C for 18 hours. Then zirconium hydroxide was calcined under flowing air (30 mL/min) at 550 °C for 3 hours.
- *Introduction of lanthanum via incipient wetness impregnation:* the support prepared with this method is labelled LaZimpr. A proper amount of La(NO₃)₃·6H₂O was added to the calcined zirconia support in order to obtain 6 wt % of La₂O₃ on the final catalyst. The material was dried at 110 °C for 18 hours and then calcined again under flowing air (30 mL/min) at 550 °C for 3 hours.
- *Introduction of lanthanum via coprecipitation:* the support prepared with this method is labelled LaZcopr. A proper amount of La(NO₃)₃·6H₂O was dissolved together with the zirconia precursor in order to obtain 6 wt% of lanthanum in the final catalyst. The synthetic methodology was the same previously described for plain zirconia.
- *Introduction of nickel oxide:* Nickel was introduced on the supports (Z, LaZimpr, and LaZcopr) by incipient wetness impregnation using a proper amount of Ni(NO₃)₂·6H₂O aqueous solution in order to obtain 8.5 wt% of nickel on the material. After drying at 110 °C

for 18 hours, a calcination was performed under flowing air (30 mL/min) at 550 °C for 4 hours.

The samples were labelled as:

NiZ

NiLaZimpr (introduction of La₂O₃ via impregnation method)

NiLaZcopr (introduction of La₂O₃ via co-precipitation method)

4.1.2 Catalyst Characterisations

N₂-physisorption and TPR analysis were performed as reported in section 2.1.2 of Chapter 2, while XRD, SEM and DRIFT-MS were carried out as reported in section 3.1.2 of Chapter 3.

Temperature programmed desorption of CO₂ (CO₂-TPD) were carried out in the same lab-made equipment used for TPR. 50 mg of calcined sample was heated in He (30 mL/min) to 500 °C and left at this temperature for 1 h to clean the surface. The temperature was then decreased at 25 °C. Before heating with a temperature rate of 10 °C/min from 25 °C to 800 °C in He flow (40 mL/min), the sample was exposed to five CO₂ pulses of 0.7 mL each in order to obtain over saturation of the samples.

The Ni amount was determined by atomic absorption spectroscopy (AAS) after microwave disaggregation of the samples (100 mg), using a Perkin-Elmer Analyst 100. The La amount was determined by MP-AES (Microwave Plasma Atomic Emission Spectroscopy) technique after microwave disaggregation of the samples (100 mg), using MP-AES 4210 (Agilent).

4.1.3 Catalytic test

The catalytic tests were carried out in the same equipment described in Scheme 3.1. In this case, the reactor was charged with 0,075 g of catalyst and SiC (Carborundum VWR Chemicals, 0,500 mm) in 1:4 volume ratio. Using a HPLC pump (Gilson 303) the mixture of water and ethanol (molar ratio 6:1) was flowing with 0,02 mL/min and helium (230 ml/min) was used as carrier (W/F ratio = 1,44 g*h/gmol). No pre-treatment of catalyst was performed. The typical reaction temperature was 550 °C. Preliminary blank tests have shown the absence of conversion at this temperature. After the analysis, the following data were calculated:

Conversion of ethanol:

$$\text{conversion (\%)} = \left[\frac{n_{in}(\text{EtOH}) - n_{out}(\text{EtOH})}{n_{in}(\text{EtOH})} \right] * 100$$

Conversion of water:

$$\text{conversion (\%)} = \left[\frac{n_{in}(H_2O) - n_{out}(H_2O)}{n_{in}(H_2O)} \right] * 100$$

Product distribution:

$$i \text{ distribution (\%)} = \frac{f_i \text{ out}}{\sum f} * 100$$

H₂ yield:

$$\text{yield (\%)} = \frac{f_{H_2 \text{ out}}}{6 * f_{EtOH \text{ in}}} * 100$$

C balance:

$$C (\%) = \left(\sum [f_i \text{ out} * \chi_i] \right) / f_{EtOH \text{ in}} * 100$$

With $n_{in/out}$, number of moles that goes in/out; χ_i = number of C atoms in the i -th molecule and f , the flux in mL/min.

4.2 Results and Discussion

4.2.1 Catalyst characterisations

Lanthanum was introduced in the material by two different synthetic approaches to study not only its doping effects, but also how the preparation method influences the catalyst's properties. Lanthanum incipient wetness impregnation over zirconia (*LaZimpr*) and lanthanum co-precipitation with zirconia (*LaZcopr*) were investigated. First, N_2 adsorption-desorption measurements were carried out in order to quantify their specific surface area and pore size distribution. The surface area, the pore volume and the mean pore size of the three zirconia samples are reported in the Table 4.1. The corresponding isotherms are shown in the Figure 4.1. According with IUPAC classification, the three catalysts exhibit a type IV isotherm containing a H_3 hysteresis loop, typical of mesoporous materials that don't have a well-defined mesoporous structure. In detail, *NiZ* and *NiLaZimpr* present almost the same isotherms shape and BJH distribution, meanwhile for *NiLaZcopr*, the surface area is slightly higher, the pore size distribution is broader, and the hysteresis shape is wider. Thus, it's possible to suppose that lanthanum added via co-precipitation method slightly affects the structural properties of zirconia material. On the contrary, in the case of impregnation method, this effect has not been indicated because zirconia structure has already been formed during the first calcination step; only a small decrement in BET surface area value due to the introduction of nickel via impregnation method is observed.

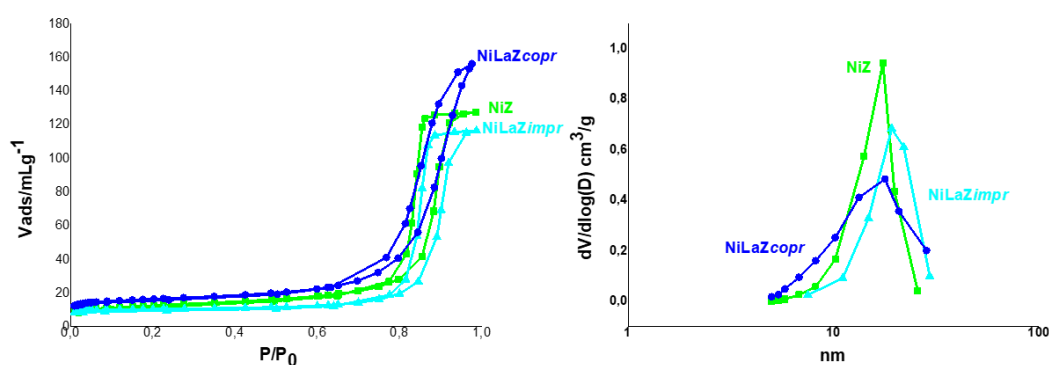


Figure 4.1 N_2 adsorption/desorption isotherms and BJH curves (inset) of *NiZ* (■) *NiLaZimpr* (▲) and *NiLaZcopr* (●) catalysts.

Table 4.1 Physical and chemical properties of catalysts

	NiZ	NiLaZimpr	NiLaZcopr
Surface area (m ² /g)	45 ± 3	40 ± 3	55 ± 3
Mean pore size (nm)	17	18	15
Pore Volume (cm ³ /g)	0.19	0.18	0.22
Nickel amount (wt %)	8.5	8.2	8.6
Lanthanum amount (wt%)	0	4	4.4

Regarding nickel and lanthanum amount, reported in Table 4.1 and calculated via atomic adsorption and MP-AES respectively, it is almost the same for all the sample and it agrees with the nominal amount.

TPR measurements were carried out for the identification of NiO species over the supports according to their reduction temperature (Figure 4.2). Since nickel presents only one oxidation state transition, from 2+ to 0, and zirconia and lanthanum don't show any reduction peak between 25 °C and 900 °C, the presence of more than one peak suggests different interactions between support and active phase [134–136]. NiZ sample exhibits two different peaks: a small one at 360 °C and a bigger one at 520 °C respectively. The first one is ascribable to nickel lowly interacting with the support and the second one to nickel that strongly interplays with it [137]. In the case of NiLaZimpr, these two peaks are shifted to lower temperatures, respectively to 280 °C and 400 °C. This result indicates that lanthanum added via impregnation method affects the interactions between nickel and zirconia, reducing their strength and therefore the reduction temperature of the catalyst [114]. In the case of NiLaZcopr, the TPR profile is completely different. One broad peak with three different *maxima* is present between 350 °C and 550 °C. This means that there are at least three different NiO species interacting with the support; moreover, most of nickel interacts weaker with the support than NiZ since the higher maximum is associated with the peak located at lower temperature. Besides, based on TPR profiles, it's possible to assert that nickel is completely reduced before 550 °C for all the three zirconia catalysts. This is relevant for the ESR reaction conditions that will be discussed later.

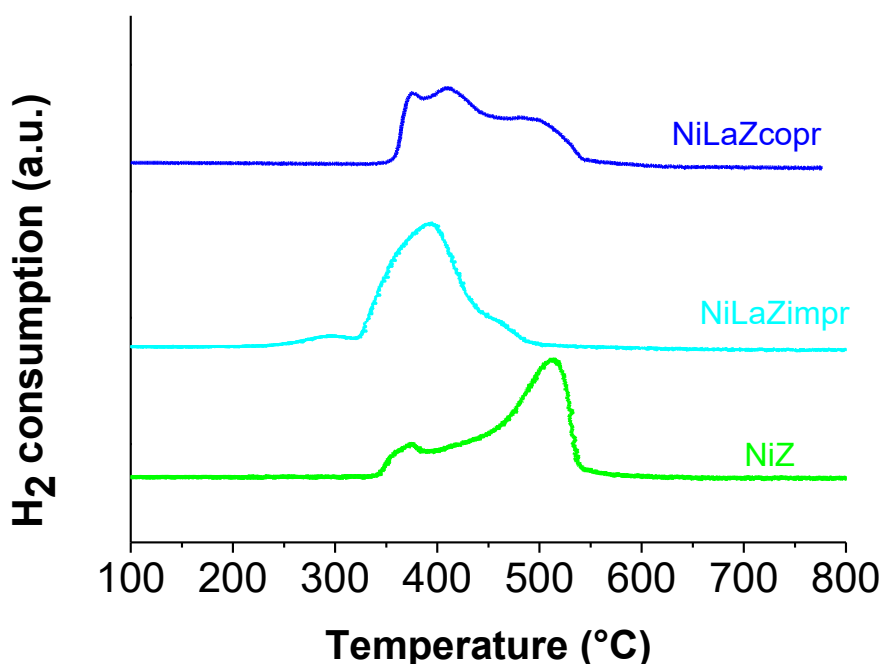


Figure 4.2 TPR profiles of NiZ, NiLaZimpr and NiLaZcopr samples.

XRD analyses were performed to identify zirconia polymorph and Ni particle size, using Rietveld refinements. As for the support, looking at Figure 4.3, it is clear that for NiZ and NiLaZimpr, zirconia is present in two different phases: monoclinic and tetragonal, respectively at 2θ 24.3, 28.0, 31.55, 34.2, 40.8, 44.9, 45.5, 49.4, 54.0, 55.4 ° for monoclinic phase and 2θ 30.2, 35.5 and 50.3 ° for tetragonal phase [138]. The addition of lanthanum led to a slight increase of the tetragonal/monoclinic ratio. By contrast, in the case of NiLaZcopr only tetragonal phase is detected at 2θ 30.2, 35.5 and 50.3 °. Therefore, it seems that lanthanum added on the support via co-precipitation method stabilizes the zirconia tetragonal phase. Tetragonal phase is a zirconia phase that is stable at 1170 °C. Nevertheless, the structure of tetragonal phase of zirconia can be stabilized at room temperature by the incorporation of metal cations. In fact, this has been widely studied for ceramic applications [139]. For example, the stabilisation of metastable zirconia tetragonal phase with the addition of yttria [140] and with the use of sulfated zirconia [141] have been proven. In this work we have verified the stabilization of zirconia by lanthanum addition via co-precipitation. It's important to underline that only with this method it is possible to tune the morphological and structural feature of the material, therefore this can be a clear indication that the synthetic approach could strongly affect the final catalysts. In the case of nickel, for all the samples exposed to reduction treatment, it appears only in the metallic form (peak at $2\theta = 44.5$ °). This demonstrates that the reduction treatment at 550 °C is

effective for reducing all Ni^{2+} to Ni^0 , according to TPR profiles previously discussed. At the same time, nickel particle size hasn't been affected by lanthanum addition. In particular, the average crystallites size of 13-15 nm has been calculated by Rietveld refinements, respectively NiZ (14 nm), NiLaZimpr (13 nm) and NiLaZcopr (15 nm). These data agree with SEM results that are shown in Figure 4. Moreover, it is visible an homogeneous distribution of nickel particles over zirconia surface.

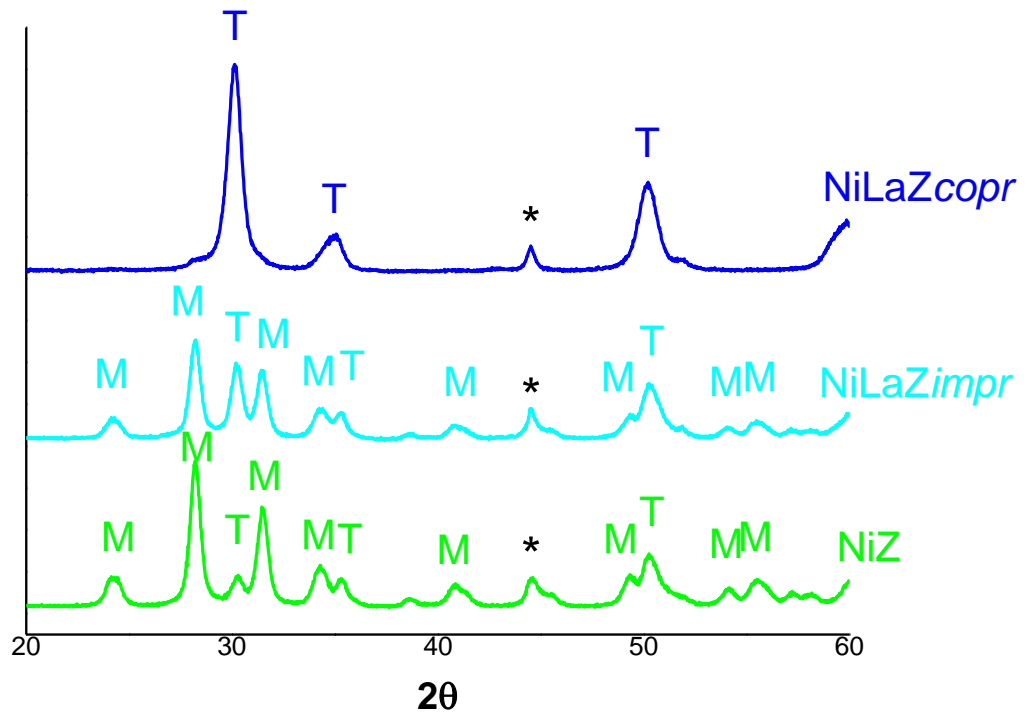


Figure 4. 3 XRD analyses of reduced NiZ, NiLaZimpr and NiLaZcopr samples (* is the Ni^0 species, M is the zirconia monoclinic phase and T is the zirconia tetragonal phase).

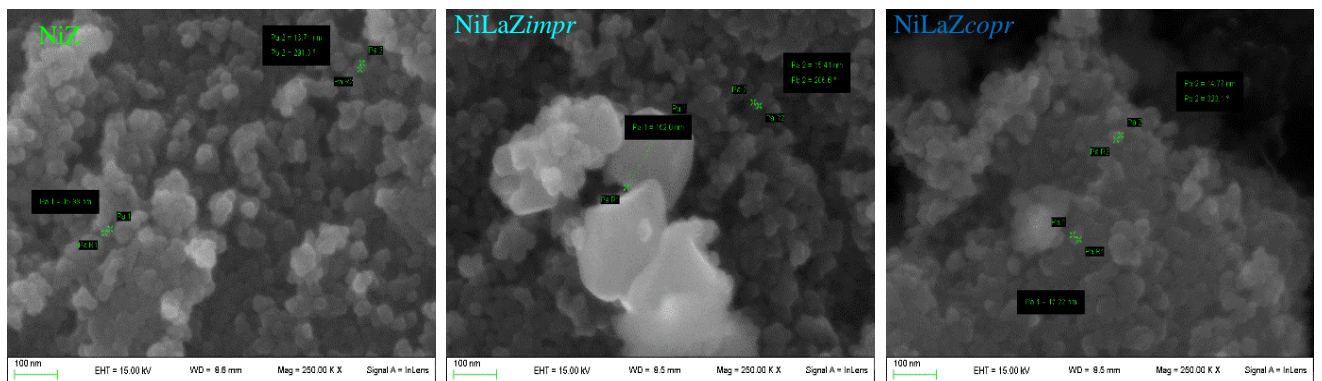


Figure 4.4 SEM images of as prepared NiZ, NiLaZimpr and NiLaZcopr samples.

From these preliminary characterizations, it can be concluded that lanthanum added by incipient wetness impregnation (NiLaZimpr) doesn't affect the structural and morphological properties of the material, leaving similar surface area, pore size distribution and zirconia phases. Only an enhancement of nickel reducibility has been evidenced, even if metal particle size is the same of NiZ catalyst. By contrast, addition of lanthanum by coprecipitation (NiLaZcopr) stabilized the tetragonal phase of zirconia, increased the surface area of the support and determined more different nickel species interacting with the support; in this case it was increased the amount of nickel that weakly interacts with the support.

4.2.2 Catalytic tests

Catalytic tests for ESR were performed for these materials. Figure 4.5 shows ethanol conversion vs time of stream, meanwhile in Table 4.2, hydrogen yield and products distribution registered after 16 hours of reaction are reported. As regard as ethanol conversion, a strong promoting effect of lanthanum addition is evident. NiZ sample demonstrates a decrement in ethanol conversion after only two hours of reaction, reaching the value of 44 % on the 16th hour. On the other hand, in the case of both lanthanum promoted samples, ethanol conversion is quite stable till the 4th hour of reaction following with a gradual decrease till 16th hour. Impregnation of lanthanum over calcined zirconia (NiLaZimpr) allows to keep 80 % of ethanol conversion, meanwhile for NiLaZcopr higher deactivation is visible. The same trends were obtained for hydrogen yield. For NiZ sample, 50 % of yield is registered in the first hours, getting to 7 % after 16 hours; meanwhile, for the promoted catalysts, higher H₂ yield is maintained. NiLaZrcopr gets 15 % of H₂ yield meanwhile NiLaZrimpr presents the highest activity at the end of the reaction with 25 % of H₂ yield. In the case of products distribution, no differences between the three samples are observed. Carbon monoxide, carbon dioxide and hydrogen are the only products depicted, and their distribution values are maintained constant for 16 hours of the reaction. No other products, such as acetaldehyde, ethylene or acetone have been evidenced for the three catalysts.

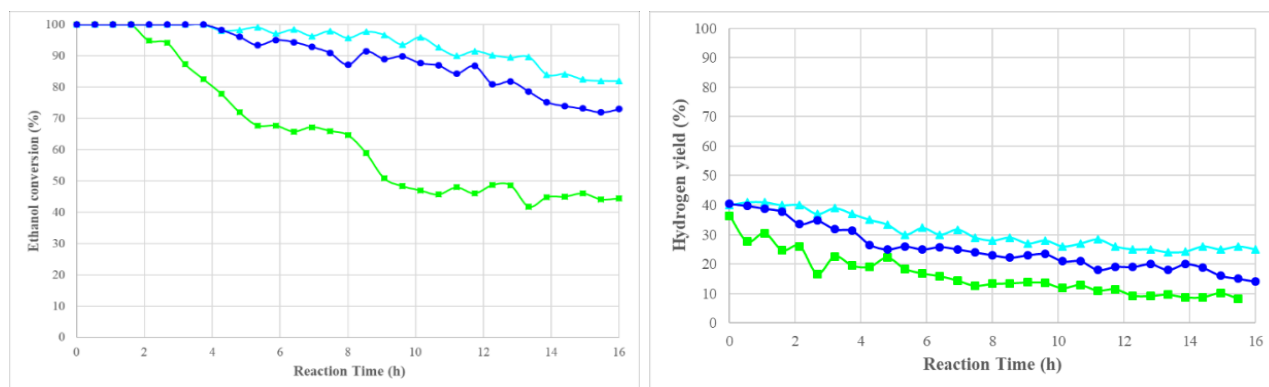


Figure 4.5 Ethanol conversion (left) and hydrogen yield (right) for NiZ (■), NiLaZimpr (▲) and NiLaZcopr (●) during test at 550 °C.

In conclusion, lanthanum addition has strongly affected the catalytic behaviour of NiZ sample. Nevertheless, it didn't affect the distribution of the products. In any case, the synthetic procedure used for lanthanum addition influences the catalytic results.

Table 4.2 Hydrogen yield, products distribution, ethanol and water conversion for NiZ, NiLaZimpr and NiLaZcopr after 16 hours of reaction at 550 °C.

	NiZ	NiLaZimpr	NiLaZcopr
H ₂ yield (%)	7	25	15
H ₂ distribution (%)	74	69	70
CO ₂ distribution (%)	25	27	25
CO distribution (%)	1	3	6
EtOH conversion (%)	44	81	73
H ₂ O Conversion (%)	8	15	20
C Balance (%)	65	55	47

It is difficult to understand the rapid deactivation of NiZ, as the distribution of the products is the same for all three catalysts. Therefore, to gain insight on the effect of lanthanum, DRIFT-MS analyses were performed only to NiZ and NiLaZrcopr, since the two promoted samples showed similar catalytic performances.

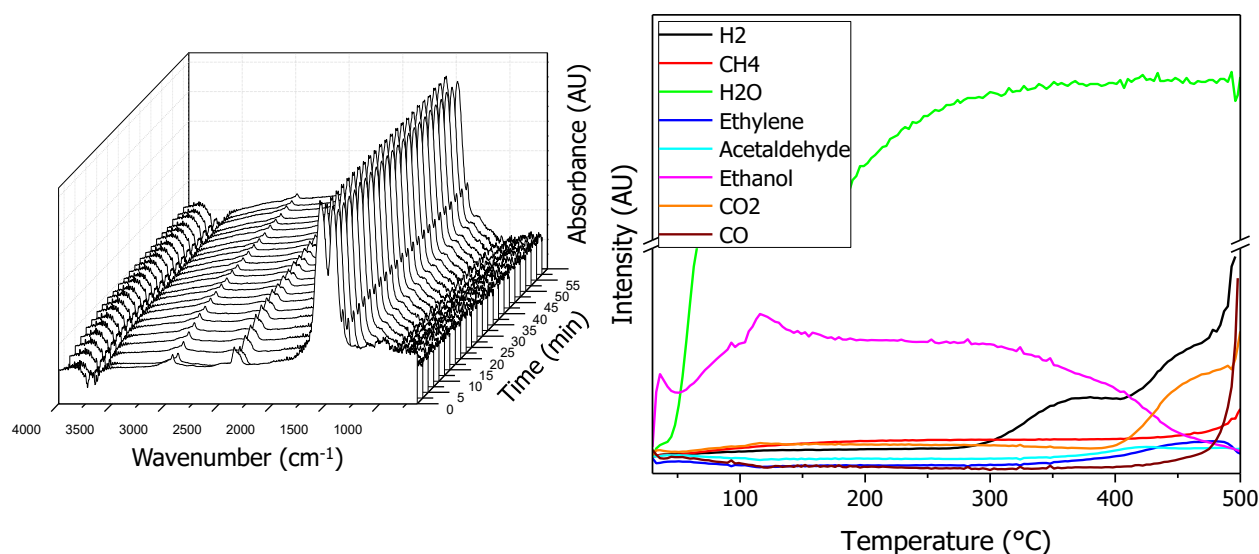


Figure 4.6 DRIFT spectra recorded at 500 °C and MS spectra from RT to 500 °C feeding EtOH/H₂O on NiZ

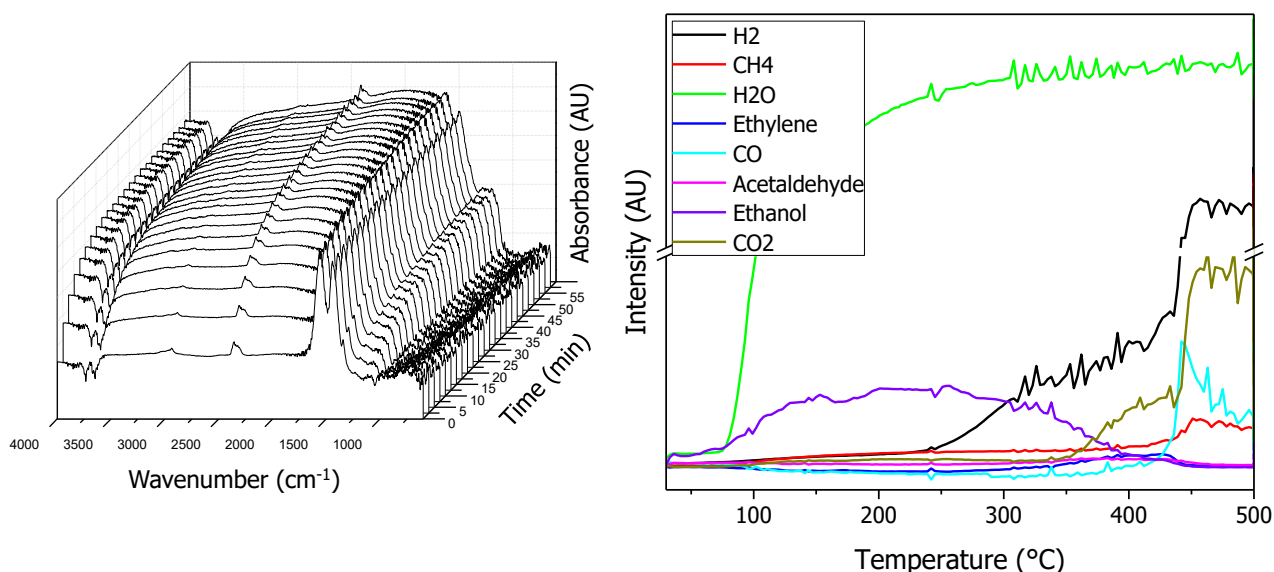
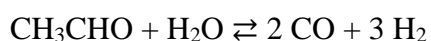


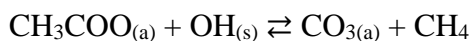
Figure 4.7 DRIFT spectra recorded at 500 °C and MS spectra from RT to 500 °C feeding EtOH/H₂O on NiLaZcopr

The spectra of the catalysts recorded in presence of EtOH/H₂O mixture at 500 °C are reported on the left-side hand of Figure 4.6 and Figure 4.7 for NiZ and NiLaZcopr, respectively. It is possible to observe that the base line of the spectra is changing over the time, and this change is different for the two samples. In detail, NiZ base line is not changing over 60 minutes while the NiLaZcopr one is dramatically changing. This change can be ascribed to NiO reduction into Ni [125]. These results support the H₂-TPR ones, which showed that NiLaZcopr possess higher reducibility than NiZ. Remarkably, ethanol/water mixture is not able to completely reduce NiLaZcopr in an hour while the same sample when exposed to pure ethanol is already completely reduced in the very first spectrum at 500 °C, as reported on the right-hand side in Figure A.5 in the Appendix A2. This observation seems to support the idea that ethanol is the reducing agent. The MS ethanol signal increased for both samples until 100 °C, as reported in Figure 4.6 and 4.7. All the product signals are strongly influenced by ethanol below 300 °C, and it is not possible to obtain useful information about their formation. At 300 °C the catalyst started to be active in converting ethanol as evidenced by its decreasing slope. At the same temperature, acetaldehyde and ethylene intensities increased along with H₂, suggesting that ethylene and acetaldehyde were produced by ethanol dehydration and oxidative dehydrogenation, respectively. In contrast, CO and CO₂ trends started to increase at 400 °C. Their production was attributed to acetaldehyde decomposition in presence of water:



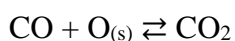
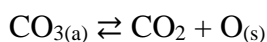
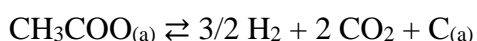
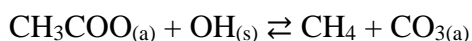


In fact, η^2 -acetaldehyde bands were detected on the catalyst surface, as reported in Figure A.4 in the Appendix A2. These bands at 400 °C started to decrease supporting the hypothesis of acetaldehyde decomposition reactions. At slightly higher temperature, CH₄ started to be formed probably by decomposition of acetates on the catalyst surface to carbonates:



Where (s) indicates a catalyst moiety while (a) a specie adsorbed on the catalyst surface.

At 400 °C ethylene and acetaldehyde reached their maximum in intensity while CO, CH₄, CO₂ and H₂ intensity slopes became steeper. This increment might be due not only to the decomposition reaction or the side reaction of ethylene, acetaldehyde and ethanol but to all the reaction that might be involved in the ESR process, such as methanation, WGS and Boudouard, combined with the following surface reactions:



The main difference was the ethylene acetaldehyde ratio between the two samples. In fact, NiZ acetaldehyde trend is almost flat suggesting a low production while ethylene trend showed a maximum between 400 °C and 500 °C. In contrast, ethylene and acetaldehyde trends were almost comparable with NiLaZcopr. A slight increase in acetaldehyde trend from 300 °C seems to suggest that the oxidative dehydrogenation of ethanol might be favoured with respect to dehydration.

From this analysis it is evident how there is a difference in products distribution between non-promoted and promoted samples even though this difference cannot be depicted during the catalytic tests. The greater production of ethylene for the non-promoted catalyst may be the cause of its deactivation. In fact, the presence of ethylene can bring to polymerization reaction that lead to coke formation. Ethylene production is favoured by the presence of acid sites that catalysed the ethanol dehydration reaction [142]. For this reason, acidic surface analysis was performed using CO₂-TPD technique. In Figure 4.8 it is reported the CO₂ evolution in function of temperature and in Table 4.3 there are reported the amounts of basic sites obtained by the integration of desorption peaks. In particular, as reported by D. Wierzberg *et al.* [143], three different regions are observed related

respectively to weak (50-250 °C), medium (300-600 °C) and strong (600-800 °C) basic sites. In Table 4.3 it is also reported the total amount of basic sites. For the promoted sample, such value is an order of magnitude higher than for non-promoted one. Knowing that the temperature of the peaks is correlated with the nature of the sites [144], it can be highlighted how the number of medium and strength basic site does the difference. Therefore, the introduction of lanthanum on the support increases its basic properties and limits ethanol dehydration, leading to less formation of carbonaceous species consequently. Moreover, basic sites guarantee CO₂ adsorption and disproportion into carbon monoxide and oxygen that could increase the elimination of carbon deposits [145]. For these reasons, both lanthanum doped samples have higher stability and higher hydrogen yield.

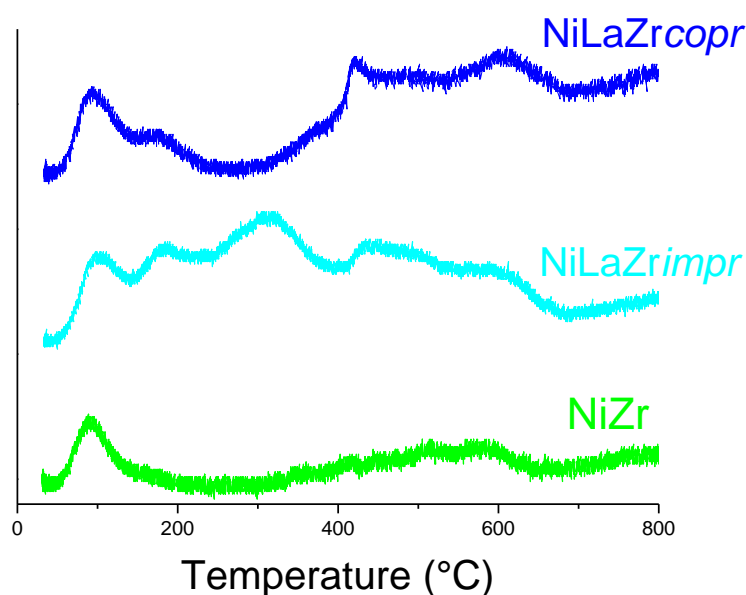


Figure 4.8 CO₂-TPD of NiZ, NiLaZimpr and NiLaZcopr catalysts.

Table 4.3 Distribution of basic sites for NiZr, NiLaZrimpr and NiLaZcopr samples.

	Total basicity ($\mu\text{mol/g}$)	Weak basic sites ($\mu\text{mol/g}$)	Medium strength basic sites ($\mu\text{mol/g}$)	Strong basic sites ($\mu\text{mol/g}$)
NiZ	108	32	13	63
NiLaZimpr	350	114	34	202
NiLaZcopr	309	77	63	169

Nevertheless, the different catalytic activity of the promoted samples can also be attributed to the higher basicity of NiLaZimpr, which maintains a greater conversion of ethanol and higher hydrogen yield over 16 hours of reaction. To confirm the promoter effect of lanthanum in avoiding dehydration reaction and understand the differences in its introduction methods, coke analysis of used samples were performed via SEM, TG and Raman spectroscopy. It is known in literature that catalyst deactivation is not only due to the amount of coke deposited over its surface but by the nature of this coke principally [146]. In the case of steam reforming process over nickel, two different kind of coke can be produced: amorphous coke, accountable of the obstruction of metal sites, and filamentous coke, that doesn't affect the metal activity but blocks the entrance of the reagents. Moreover, nature, size, length and thickness of the coke are important parameters that influence the kind of deactivation [146]. The kind of coke depends on the reaction more involved in the process. Montero *et al.* reported that filamentous coke is produced by CH₄ decomposition reaction and Boudouard reaction meanwhile, amorphous coke is produced by ethylene and others oxygenated products condensation [147]. SEM images of used catalysts are showed in Figure 4.9. Looking at the image at low resolution (left), it is evident how filamentous coke is formed in prevalence only in the catalysts NiZ and NiLaZcopr while in the catalyst NiLaZimpr it is possible to observe a minor presence of carbon coke deposition. This result is confirmed by EDX analysis (Figure 4.10) in which for NiLaZimpr, carbon peak is lower than for the other catalysts.

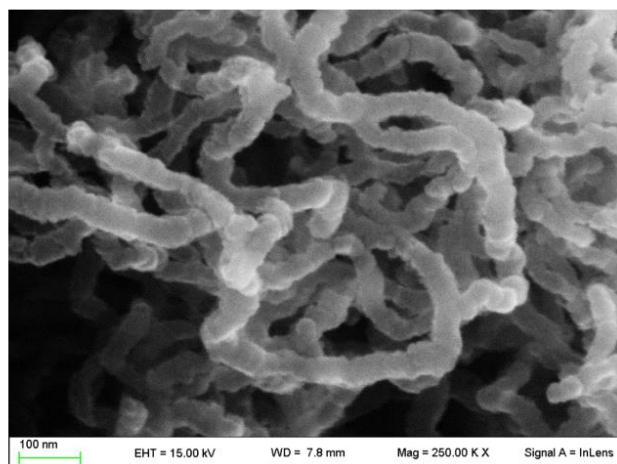
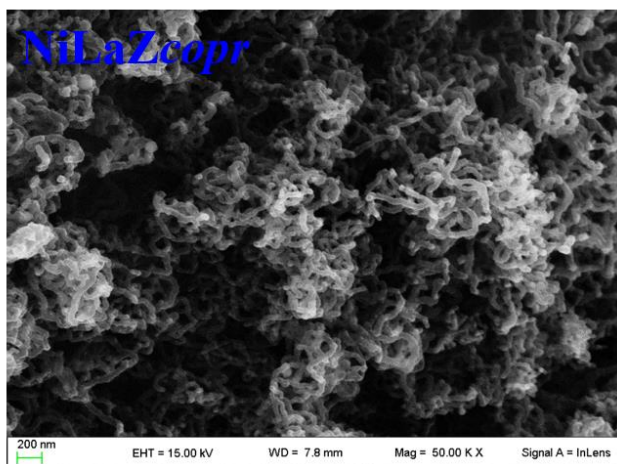
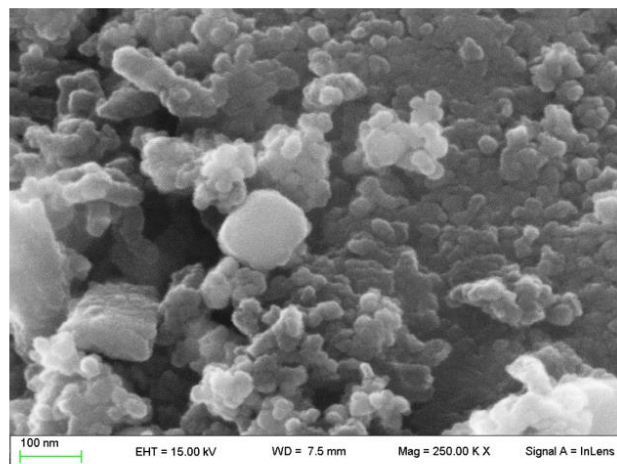
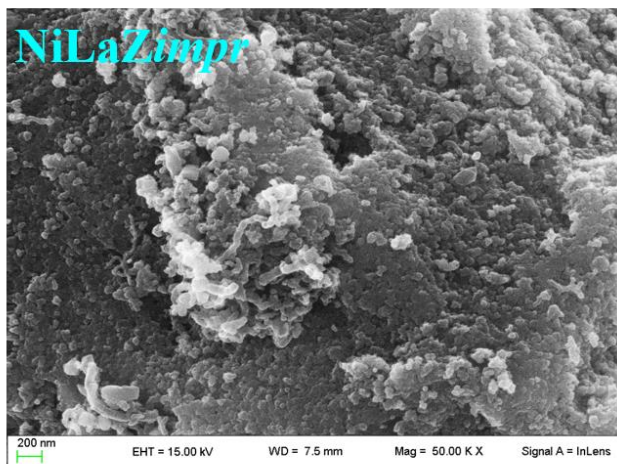
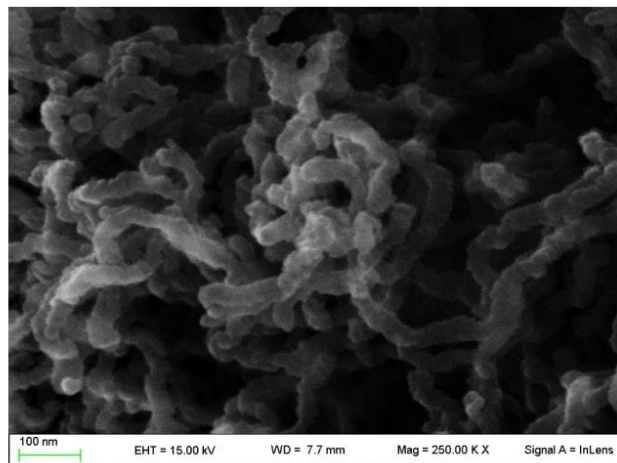
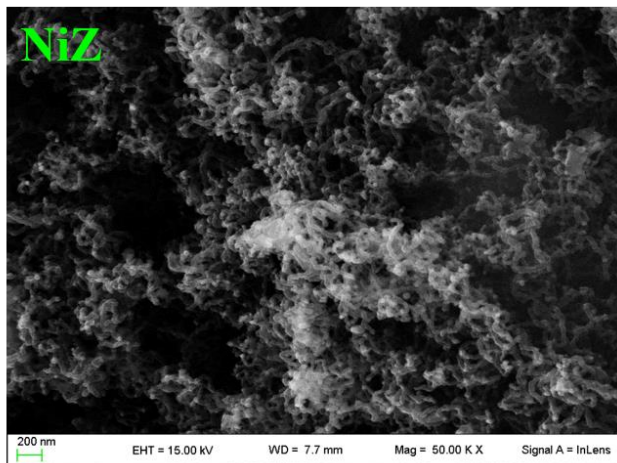


Figure 4.9 SEM images of NiZ (top), NiLaZimpr (middle) and NiLaZcopr (bottom) samples after catalytic test.

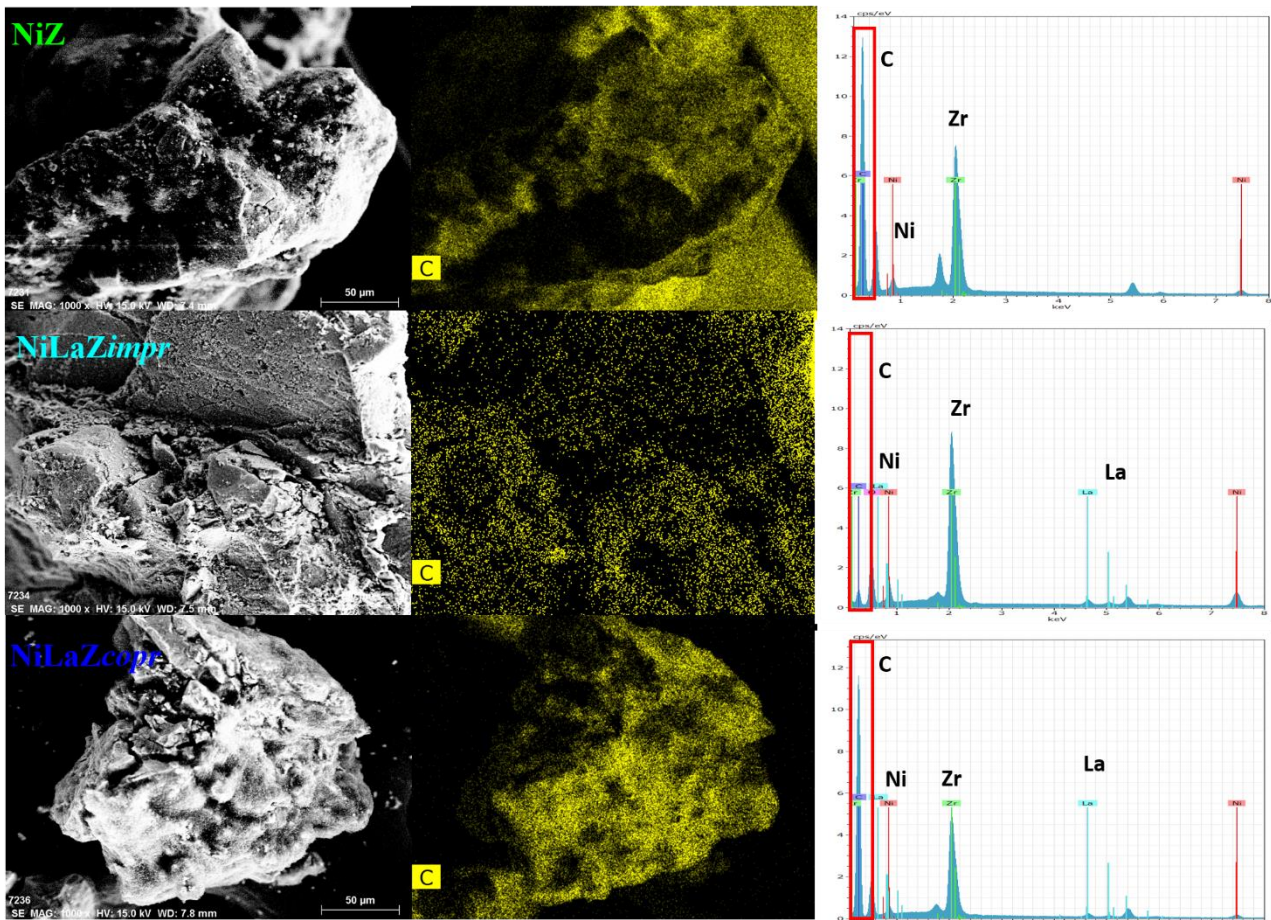


Figure 4.10 EDX analyses and Carbon mapping images of NiZ (top), NiLaZimpr (middle) and NiLaZcopr (bottom) samples after catalytic test.

To further understand the nature of carbon sediment on the catalyst, Raman spectroscopy was performed [148]. The main features of the spectra (Figure 4.11) are the Raman bands of carbon structures at about 1350 cm^{-1} and 1600 cm^{-1} , conventionally called D (Defect) and G (Graphite) bands, respectively. The G band is associated with the tangential stretching of C-C bonds with sp^2 hybridization, typical of ordered graphite but also of small sized chains, while D band is associated with the breathing vibrations of carbon atoms rings activated by defects. The presence of a very intense D band and the shift of the G peak from 1580 to 1600 cm^{-1} indicates that for all the samples, the sediments are mainly in the form of nanocrystalline graphite. Multiwall carbon nanotubes (MWCNTs) appear not dominant. In fact, a rough concentration assessment can be obtained from the ratio of the I_D/I_G peaks, assuming a minor contribution of interlayer defects [149]. As the I_D/I_G ratio is ~ 0.8 in NiZ and NiLaZcopr samples and ~ 1 in NiLaZimpr, it can be estimated that the MWCNTs concentration is about 20 % in the former samples, while it is below the measurability threshold in NiLaZimpr. Finally, the different morphology of the deposit carbon structures in NiZ samples is further testified by the presence of a small shoulder at 1200 cm^{-1} typical of aliphatic C-H band, which is

reduced in the co-precipitated sample and practically absent in the impregnated one. These results prove that, even if coke is produced during the reaction for all the catalysts, lanthanum addition, in particular via impregnation, reduces the formation of aliphatic coke by ethylene polymerization, since it enhances basic properties of the material.

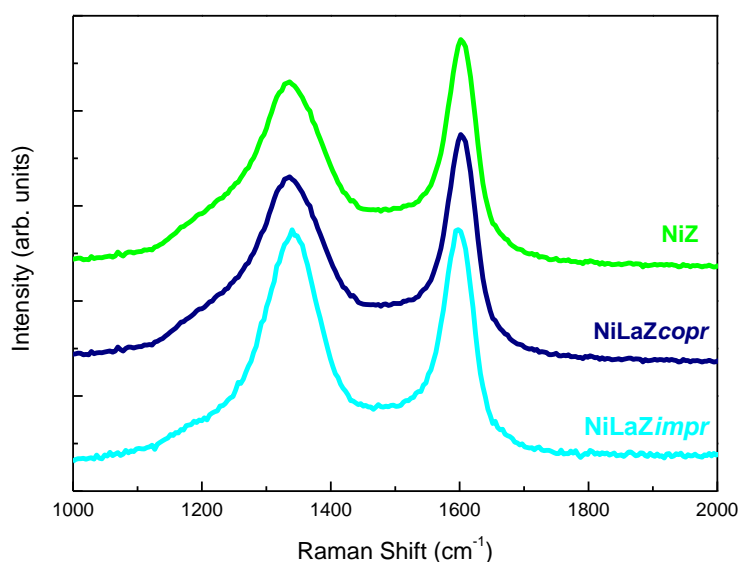


Figure 4.11 Raman spectra of NiZ, NiLaZimpr and NiLaZcopr.

To properly quantify the amount of carbon deposits over the used catalysts, TG analyses were carried out. In figure 4.12, percentage weight loss in function of temperature is represented. In line with other characterizations, not promoted sample shows the highest weight loss of 15 %, meaning the sample has undergone a greater coke coating. This data justifies its faster deactivation. In the case of promoted sample, lower weight loss is visible, 6 wt% for NiLaZcopr and 2 % for NiLaZimpr.

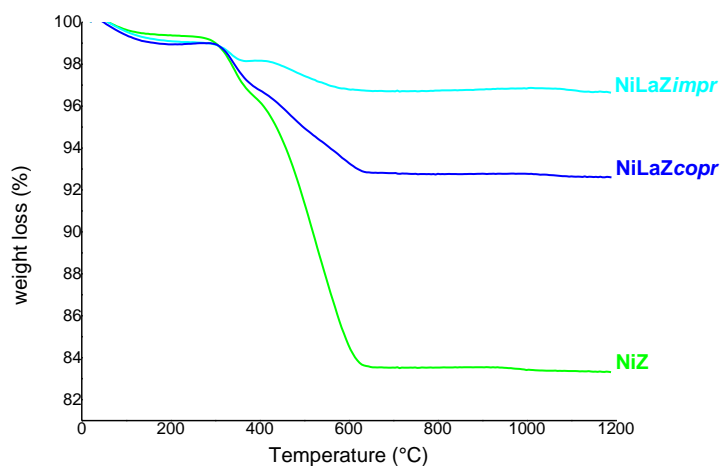


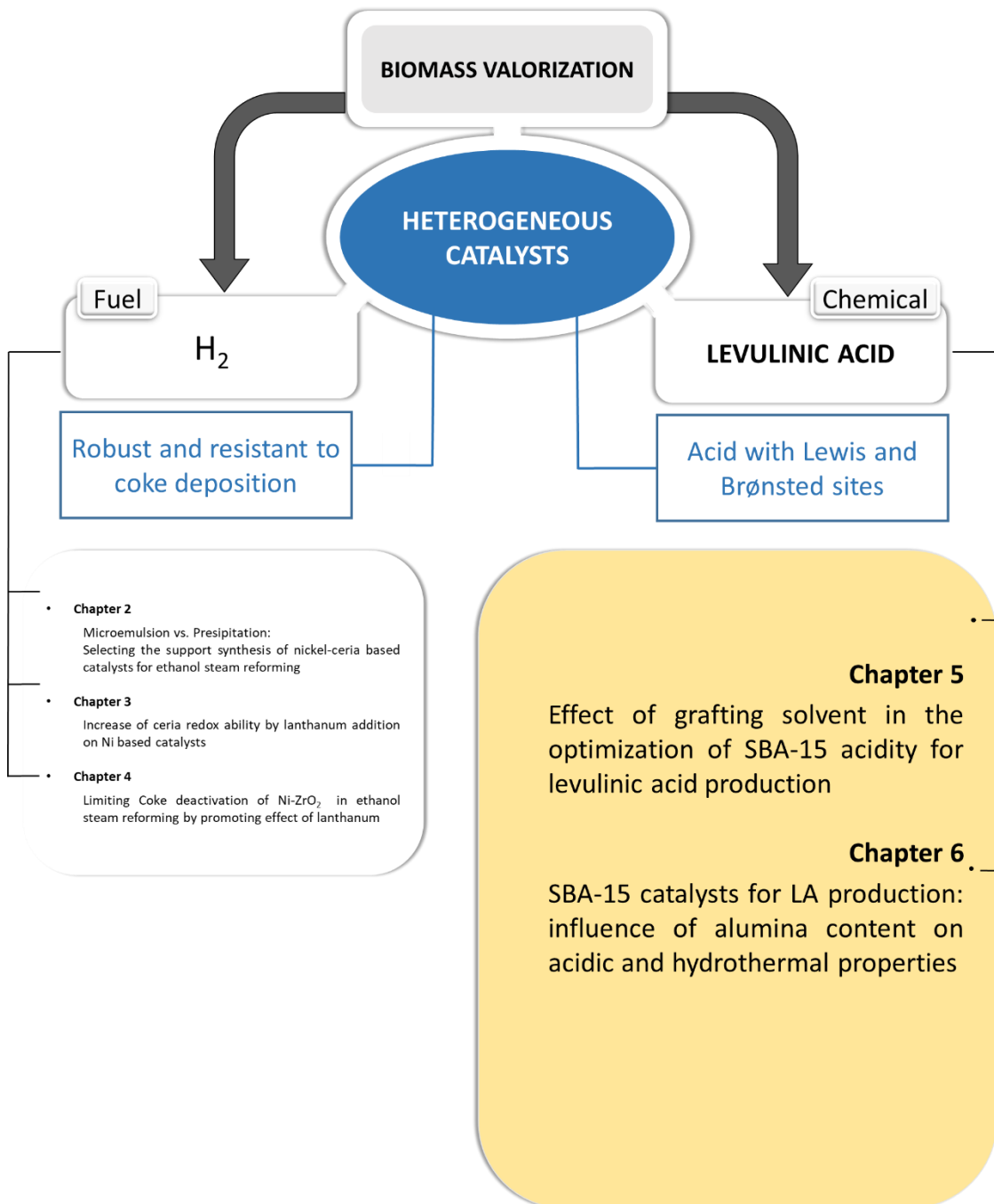
Figure 4.12 Thermogravimetric analyses of used NiZ, NiLaZimpr and NiLaZcopr.

Therefore, with this technique a better correlation between the amount of carbon and the stability of the catalyst was obtained. The most active catalyst presents the lowest amount of carbon deposits. Comparing all the data of hydrogen yield, C balance, carbon deposition and products distribution, it can be analyzed the behavior of all the samples. NiZ is the less efficient one, since the acidity of the sample is too strong and it facilitates the dehydration reaction, forming carbon nanotubes over the surface and deactivating the catalyst. Indeed, the amount of coke deposited over the surface is the highest one. Comparing the promoted sample, the impregnated one is the most active material since it presents the highest amount of medium and strong basic sites. Therefore, its deactivation is slower over time than the other 2 samples with higher carbon balance and higher hydrogen yield. In the case of the coprecipitated sample NiLaZ*copr*, it presents a lower conversion of ethanol than NiLaZ*impr* with consequently lower hydrogen yield. At the same time, the lower ethanol conversion doesn't justify such a low hydrogen yield value. Indeed, taking into consideration the DRIFT results, the carbon balance, the carbon deposits and the water conversion, NiLaZ*copr*, after some hours of reaction, prefers the dehydration route than the reforming pathway. As a demonstration of that, the value of water conversion for NiLaZ*copr* is slightly higher than the value of NiLaZ*impr*.

4.3 Conclusions

The influence of lanthanum addition on nickel-zirconia catalyst was evaluated. As already seen for ceria support in Chapter 3, lanthanum's effect strongly depends on the introduction method. Addition by incipient wetness impregnation doesn't affect the structural and morphological properties of the material, leaving a similar surface area, pore size distribution and zirconia phases. Quite the opposite, the addition of lanthanum by co-precipitation stabilizes the tetragonal phase of zirconia and increases the surface area of the material. Catalytic performances for ESR were evaluated at 550 °C; improvement in stability and hydrogen distribution for lanthanum doped catalysts with respect to the not doped catalyst was observed. No promoted sample is the less efficient one, since the acidity of the sample is too strong and it facilitates the dehydration reaction, forming carbon nanotubes over the surface and deactivating the catalyst. Indeed, the amount of coke deposited over the surface is the highest one. Comparing the promoted materials, the acidity has been decreased by the addition of lanthanum, as demonstrated by DRIFT analysis. The impregnated sample is the most active material since it presents the highest amount of medium and strong basic sites. Therefore, its deactivation is slower over time with higher carbon balance and hydrogen yield. In the case of the coprecipitated sample *NiLaZcopr*, it presents a lower conversion of ethanol than *NiLaZimpr* with consequently lower hydrogen yield. Moreover, water conversion of the coprecipitated material is higher than the impregnated one, suggesting that its faster deactivation can be related to the preference of ethanol dehydration route than the reforming pathway, after some hours of reactions. Indeed, it presents a higher amount of carbon deposits over its surface as demonstrated by SEM, TG and Raman spectroscopy.

Concluding, it is to highlight that the lanthanum effect changes with the support features. Indeed, for ceria, lanthanum increases the redox ability of the catalyst, while for zirconia, it properly modulates the acidic/basic features.



Chapter 5. Effect of grafting solvent in the optimization of SBA-15 acidity for levulinic acid production

In this Chapter, the attention has been focused on the formulation of an acid active catalyst for the hydrolysis of glucose to LA. Therefore, a deep modification of SBA-15 with sulfonic groups using post-synthesis grafting method was performed. In particular, this work focuses on the role of different grafting solvents. The traditional solvents are toluene or hexane, which are flammable and toxic. For this reason, investigation on a safer and more environmentally friendly solvent, a mixture of water and NaCl, was carried out. It was found that the nature of the solvent highly affects morphological and chemical features of the materials; the best catalytic results were obtained with the catalyst prepared in water and NaCl, as this mixture allows to guarantee the best distribution of sulfonic groups over the surface, leading to the most balanced acid catalyst. The results reported in this chapter are published as: “Effect of grafting solvent in the optimisation of SBA-15 acidity for levulinic acid production”, C. Pizzolitto, E. Ghedini, F. Menegazzo, M. Signoretto, A. Giordana, G. Cerrato, G. Cruciani, *Catal. Today*, doi.org/10.1016/j.cattod.2019.11.012, in press.

5.1 Experimental

5.1.1 Catalyst preparation

- *SBA-15 synthesis*: Mesoporous SBA-15 was synthesized according to Zhao *et al.*[150] using TEOS (Tetraethyl orthosilicate) as a silica source and, P123 (EO₂₀-PO₇₀-EO₂₀) as a template in acid solution. The mixture was continuously stirred for 24 h at 25 °C and crystallized in a Teflon autoclave at 90 °C for 42 h. The mixture was then filtered, washed, dried at 80 °C for 20 h and finally calcined in air (50 mL/min) at 500 °C for 6 h.
- *Grafting sulfonic groups* A post-grafting method was used to functionalize the above SBA-15 material. (3-Mercaptopropyl)trimethoxysilane (MPTMS, 95 % Merck) was used as grafting agent meanwhile three different solutions were used as reaction solvent:
 - 1) Toluene: 1 g of SBA-15 was dissolved in 30 mL of toluene. MPTMS was added in the mixture exhibiting 2:1 molar ratio of SiO₂ to MPTMS. The obtained suspension was refluxed at 120 °C for 24 h. After filtration of the resulting thiol-functionalized solid, it was washed with methanol (three portion of 20 mL) and dried for 18 h at 70 °C. After this step, thiol groups were converted to -SO₃H moieties by mild oxidation with 30 wt% H₂O₂ using 2:0.11 molar ratio of SiO₂ to H₂O₂, stirring for 24 h at 30 °C. The sulfonated solid was filtered, washed with methanol and dried at 25 °C for 18 h. The final catalyst was labeled SBA-TO.

- 2) Hexane: 1 g of SBA-15 was dissolved in 30 mL of hexane. As before, MPTMS was added in the mixture exhibiting 2:1 molar ratio of SiO₂ to MPTMS. The suspension was refluxed at 70 °C for 24 h. After filtration of the resulting thiol-functionalized solid, it was washed with methanol (three portion of 20 mL) and dried for 18 h at 70 °C. Then, mild oxidation with 30 wt% H₂O₂ using 2:0.11 molar ratio of SiO₂ to H₂O₂, was performed, stirring for 24 h at 30 °C. The sulfonated solid was filtered, washed with methanol and dried at 25 °C for 18 h. The final catalyst was labeled SBA-HEX.
- 3) Saline solution: 1 g of SBA-15 was dissolved in 30 mL of saline (NaCl) solution 0.2 M. MPTMS was added in the mixture exhibiting 2:1 molar ratio of SiO₂ to 1MPTMS and the mixture was stirred for 24 h at 90 °C. The solid was then washed in water (three portion of 20 mL) and dried for 18 h at 70 °C. Then, mild oxidation with 30 wt% H₂O₂ using 2:0.11 molar ratio of SiO₂ to H₂O₂ was performed stirring for 24 h at 30 °C. The sulfonated solid was filtered, washed with methanol and dried at 25 °C for 18 h. The final catalyst was labeled SBA-NaCl.

5.1.2 Catalyst characterizations

N₂-physisorption was performed as reported in section 2.1.2 of Chapter 2, while XRD was carried out as reported in section 3.1.2 of Chapter 3.

TEM images were carried out in the Lab. of Prof. Giuseppina Cerrato in the University of Turin using a JEOL 3010-UHR Instrument equipped with a LaB₆ filament (acceleration potential 300 kV) and fitted with an Oxford INCA Energy TEM 200 energy dispersive X-ray (EDX) detector. Samples were dry dispersed onto Cu grids coated with “lacey” carbon film before the analysis.

Fourier transform infrared (FTIR) spectra were carried out in the Lab. of Prof. Giuseppina Cerrato in the University of Turin with a Bruker Vector 22 spectrometer equipped with a MCT detector, at 2 cm⁻¹ resolution and accumulating 128 scans. The solid samples, in form of self-supported pellets (~10 mg cm⁻²), were inserted in a conventional quartz vacuum cell equipped with KBr windows connected to a glass vacuum line (residual pressure < 10⁻⁵ Torr) that allows to perform in situ adsorption/desorption runs. Prior to adsorption/desorption experiments of 2,6-dimethylpyridine (2,6-DMP), all samples were activated at 300 °C in an oxidizing atmosphere. 2,6-DMP adsorption/desorption tests were carried out at 25 °C. First a relatively large amount of base (~ 4 Torr) was allowed on the samples and left in contact for 2 min in order to reach a complete 2,6-DMP

monolayer formation, and then the 2,6-DMP excess was evacuated for increasing times in the 1-15 min range in order to put into evidence only the more strongly held fraction.

Thermal analyses (TG/DTA) were performed in the Lab. of Prof. Giuseppe Cruciani in the University of Ferrara using a NETZSCH STA 409 PC/PG instrument in air flux (20 mL/min) using a temperature rate set at 5 °C/min in the 25–800 °C temperature range.

Raman spectra were recorded on pure samples using with a FT-Raman Instrument (Bruker Vertex 70 spectrometer, equipped with the RAMII accessory) by exciting with a 1064 nm laser, recording 3000 scans with a resolution of 4 cm⁻¹.

Total acid sites were determined by the following titration method: 50 mg of catalyst was added to a 20 mL sodium hydroxide aqueous solution (0.002 M) and the mixture was stirred for 1 h at RT. After solid filtration, the solution was titrated using a hydrochloric acid aqueous solution (0.002 M). The number of acid sites was estimated from the difference between the total amount of base and acid used during the titration, respectively.

5.1.3 Catalytic test

The catalysts were tested for glucose and fructose hydrolysis in a batch stainless still autoclave equipped with mechanical stirring and an electric heater. Before the reaction, 500 mg of substrate, 100 mL of water and 200 mg of catalyst were loaded into the reactor and then heated to 180 °C under 10 bar of N₂. The initial time of the reaction is taken once the reaction temperature is reached. The reaction was carried out for 5 hours at 1000 rpm. After this time, the mixture was cooled down to 25 °C and separated by filtration. Reaction mixture was analyzed by high performance liquid chromatography (HPLC) Agilent Technology 1260 Infinity II, equipped by an Aminex HPX-87H column kept at 50 °C. The mobile phase was 5 mM H₂SO₄ with a flow rate of 0.6 mL/min. UV-Vis detector ($\lambda = 195$ nm) was used for analytes' identification and quantification.

Reactivity parameters were calculated as follows:

$$\text{Conversion (\%)} = \frac{(\text{mmol sub in}) - (\text{mmol sub out})}{\text{mmol sub in}} \cdot 100$$

$$\text{Yield (\%)} = \frac{\text{mmol } i \text{ out}}{\text{mmol sub in}} \cdot 100$$

Where *i* represents a general product of reaction.

5.2 Results and discussion

5.2.1 Catalyst characterisations

Figure 5.1 shows the low angle XRD patterns of pristine SBA-15 and the corresponding sulfonated materials. SBA-15 evidences three diffraction peaks: the main one at 0.95° and two smaller ones at 1.64° and 1.85° , associated with (100), (110) and (200) planes, respectively. This diffraction profile is associated with the 2D-hexagonal $p6mm$ pore structure of SBA-15 materials. The presence of the same reflections in the promoted materials confirms that the hexagonal structure is maintained after the incorporation of sulfonic groups as well. Nevertheless, the reflections intensity decreases in the modified samples, especially for SBA-HEX, suggesting that the ordered pore structure could have been affected [151].

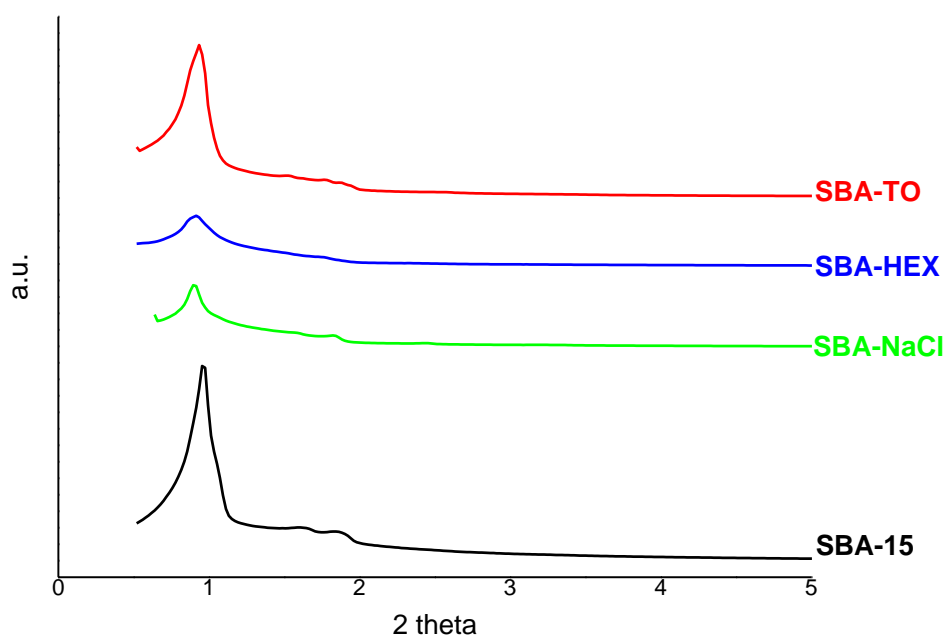


Figure 5. 1 Low-angle XRD patterns of pure SBA-15 and grafted SBA-15

The overall morphology of the materials was evaluated by means of both conventional C-TEM and HR-TEM investigations: some selected images are reported in Figure 5.1. Plain SBA-15 sample (see Figure 5.2 section a)) exhibits the typical 2D periodic hexagonal structure expected for this material. In the case of all grafted materials, the highly-organized mesoporous channels are almost totally preserved but, as already highlighted by XRD spectra, the morphology of sulfonated samples is somewhat altered in comparison with pure SBA-15 and a decrement in space order is visible: see sections b, c and d in Figure 5.2).

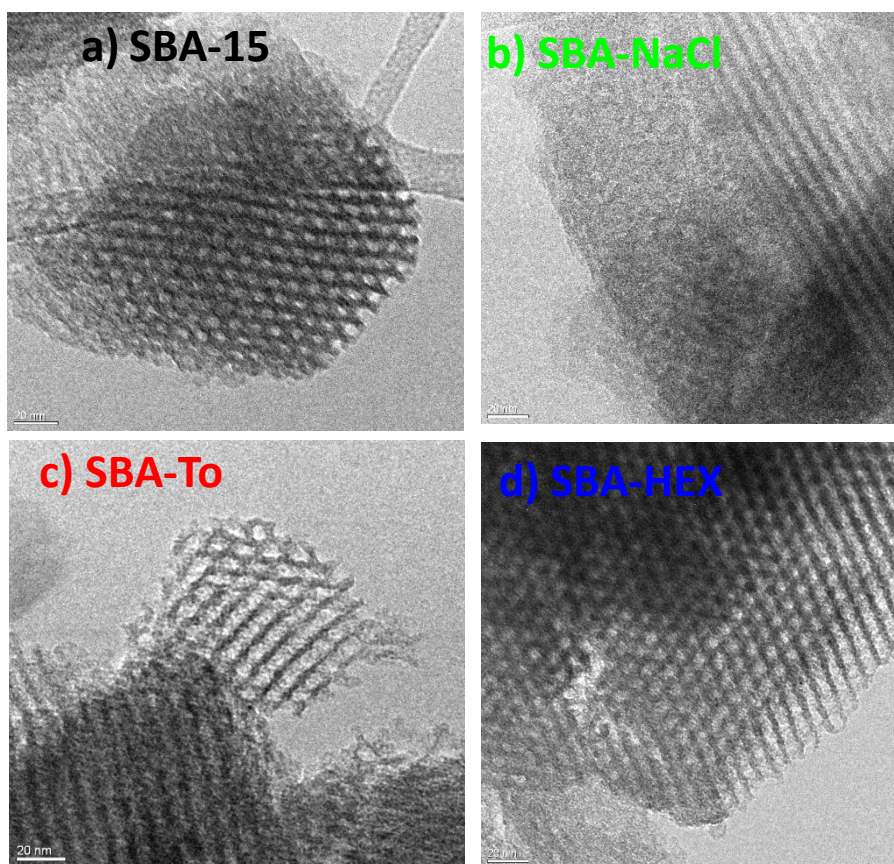


Figure 5.2 TEM images of a) SBA-15, b) SBA-NaCl, c) SBA-TO and d) SBA-HEX

These results, in accordance with XRD results, suggest that the grafting approach partially affects the ordered mesoporous organization, even though a good order degree is still preserved. Important parameters that should also be evaluated for catalytic application of these materials are surface area and pore size distribution. Therefore, the nitrogen adsorption-desorption measurements were carried out. Isotherms and the corresponding BJH pore size distributions for all the examined samples are reported in Figure 5.3, section a) and section b), respectively. All samples exhibit IV type adsorption isotherm curves with the characteristic hysteresis loop of a mesoporous material; in the case of SBA-15, the loop has a H1 shape, typical of ordered material with an open bottle-necked pore. For SBA-TO, slight modification of the hysteresis shape is visible meanwhile for both SBA-NaCl and SBA-HEX, the hysteresis loop shapes have completely changed to the H4 type. In all the isotherms, the condensation step is located in the range of 0.4-0.8 P/P_0 values. SBA-NaCl and SBA-HEX show a slight shift to lower relative pressures, indicating a slight decrement in the pore diameter. Specific surface area calculated with the BET method and the average pore diameter obtained by BJH method are reported in Table 5.1. A decrement in the BET surface area values, associated with a slight narrowing of the pore diameters, is observed moving from pure SBA-15 to the grafted samples, with the following order: SBA-TO > SBA-NaCl and SBA-HEX, respectively. As reported by other

authors¹⁹, the decrease in surface area and pore diameter values can be related to the effectiveness of the grafting approach and to the sulfonic group amount, since grafting reactions could not only proceed at the surface of the material but also inside the pore cavities. Moreover, the change in the hysteresis shape for both SBA-NaCl and SBA-HEX can be a further confirmation of the introduction of alkyl chain of MPTMS precursor inside the pore structure [152].

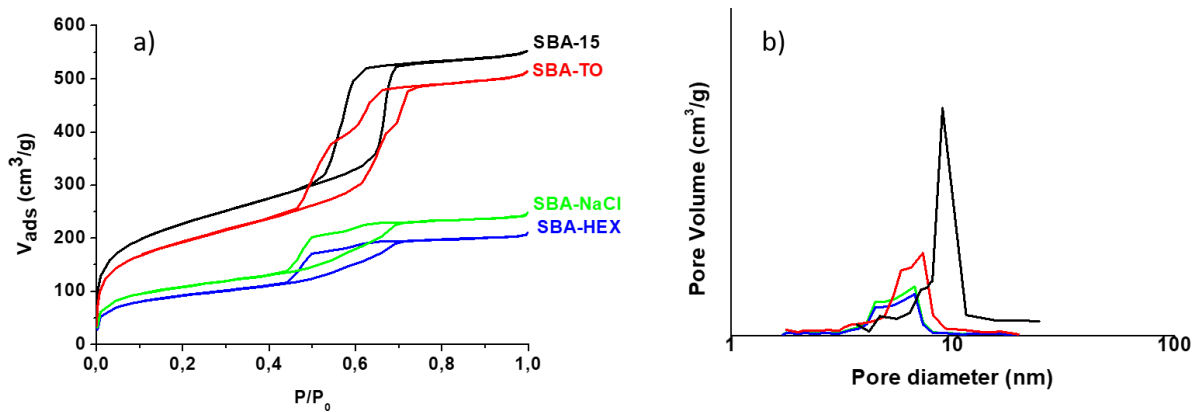


Figure 5.3 N_2 adsorption-desorption isotherms (section a) and pore size distribution (section b) of pristine and grafted SBA-15

Table 5.1 Physical properties of pristine and grafted SBA-15 (^a Specific surface area (m^2/g) calculated via BET equation, ^b Pore diameter (nm) calculated via BJH equation, ^c weight loss (%) determined by thermogravimetric analysis)

Samples	A_{sup} (m^2/g) ^a	Pore diameter (nm) ^b	Weight loss (%) ^c
SBA-15	866	5.3	-
SBA-To	655	5.4	13 %
SBA- NaCl	393	4.7	17 %
SBA- HEX	288	4.7	14 %

FTIR-analysis was carried out as a qualitative method for the identification of the surface functionalities of the materials. Figure 5.4 reports FT-IR spectra of both pristine support and grafted materials after the thermal activation: no undissociated adsorbed water is present yet, even though in the 3900-2800 cm^{-1} spectral range (ν_{OH}) it is possible to recognize two peculiar contributions. The band at higher frequency ($\sim 3740 \text{ cm}^{-1}$) can be ascribed to the ν_{OH} mode of terminal silanols free from H-bonding interaction, and a broad and unresolved envelope located at lower wavenumber due to the ν_{OH} of hydroxyl groups still interacting by H-bonding, while the signal due to terminal silanols is well resolved in SBA-15 spectrum and the unresolved envelope represents a minor spectral feature. This broad envelope is well evident for all the grafting materials even after thermal activation which represents the predominant spectral component and suggests a major hydrated surface where many OH groups may still interact by H-bonding. Nevertheless, for SBA-NaCl the peak of terminal silanols is less intense in comparison with the other sulfonated materials, suggesting that a major interaction of silanol groups with MPTMS has occurred during the synthesis. Moreover, the presence of sulfonated species is confirmed by the spectral component located at $\sim 1375 \text{ cm}^{-1}$ (see the inset to Figure 5.4), which can be ascribed to asymmetric stretching of these moieties. The intensity of this peak is slightly higher for the SBA-NaCl sample than the SBA-TO and SBA-HEX, indicating the possible presence of a larger number of sulfonated groups for the SBA-NaCl material.

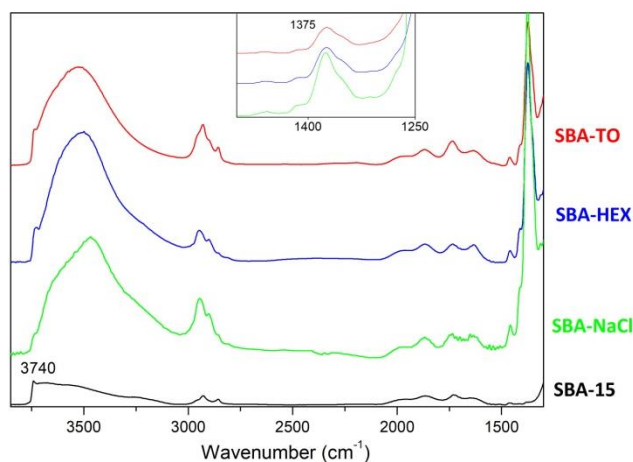


Figure 5.4 FT-IR spectra of samples after thermal treatment in vacuum

To quantify the number of these sulfonated groups on the silica surface, TG-DTA analysis was performed. In Figure 5.5, the weight loss percentage and the exchange heat as a function of the temperature are reported in the left and right ordinate respectively. For all the samples, a weight loss associated with an endothermic heat transfer is visible below $150 \text{ }^\circ\text{C}$ which can be attributed to the removal of adsorbed water.

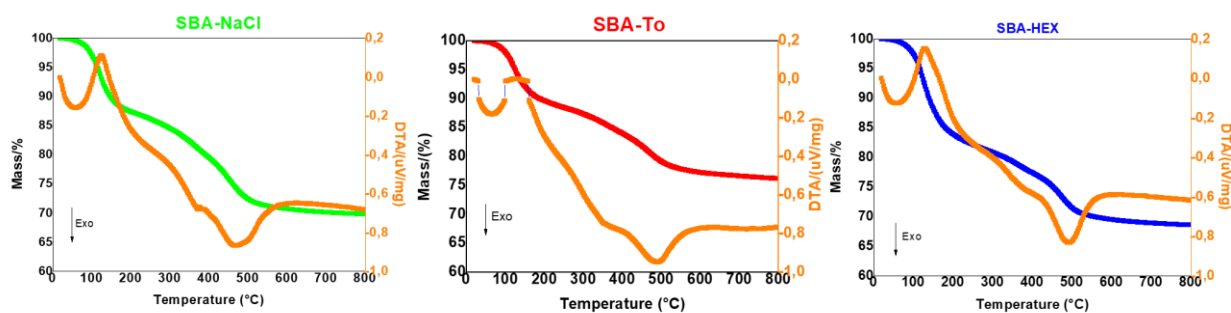


Figure 5.5 TG-DTA analysis of SBA-NaCl, SBA-TO and SBA-HEX catalysts.

For all the samples, a second exothermic band in the 350 – 600 °C temperature range is visible. This peak is associated with the decomposition of alkyl sulfonic acid group in C_3H_6 , SO_2 and H_2O . Therefore, as reported by P. Zhang *et al.*¹⁹, the weight loss in this temperature range can be correlated with the number of sulfonic groups grafted on the material surface. As reported in Table 5.1, the catalyst prepared in saline solution (SBA-NaCl) presents the most remarkable weight loss. Hence, the highest amount of the sulfonated species was anchored on the support. Hexane solvent makes the grafting less effective, meanwhile the most traditional solvent, toluene, seems to be the least efficient. Thermal analysis results also confirm the effectiveness of the oxidation step, since no peaks associated with the oxidation of thiol species to sulfonic groups are present. In this regard, Figure 5.6 reports the TG-DTA analyses conducted on the materials before the H_2O_2 treatment. Mercaptopropyl groups were decomposed at 350 °C. As can be seen in Figure 5.6, a broad exothermic peak between 200-600 °C is visible, associated firstly with the thiol (-SH) and disulphide (-S-S-) decomposition, followed by the decomposition of propyl sulfonic acid group above 350 °C²². The difference between the not oxidized (Figure 5.6) and oxidized samples (Figure 5.5) is obvious since in the last case, the range of temperature associated with the endothermic peak is sharper and is located at higher temperature.

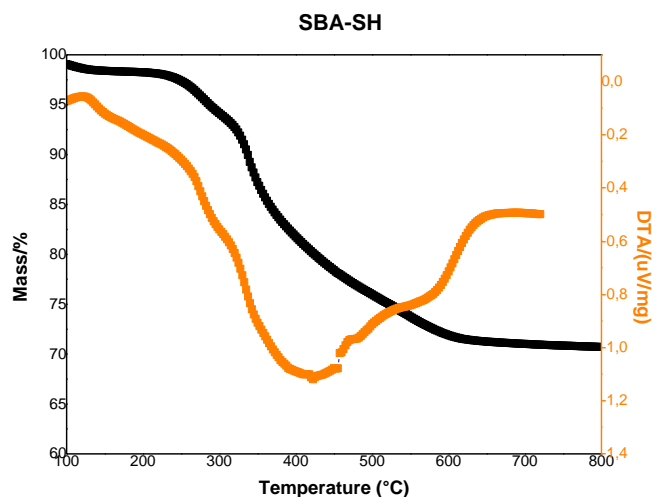


Figure 5.6 TG-DTA analysis of SBA-SH

Further investigation was performed via Raman spectroscopy to definitively exclude the presence of unreacted –SH groups, as Raman spectroscopy is very sensitive toward thiol vibrations. The comparison among the Raman spectra of SBA-15, SBA-SH and the sulfonated materials is reported in Figure 5.7.

The SBA-15 spectrum exhibits five weak signals at low wavenumbers. It is very similar to that of pure silica, but for the intensity of the peak at 980 cm^{-1} (see the magnified black curve in Figure 5.7), ascribable to surface silanol groups, becomes more relevant in mesoporous systems [153].

On the contrary, the spectrum of grafted-MPTMS (SBA-SH) sample exhibits a strong band at $\sim 2570\text{ cm}^{-1}$, ascribable to the $\nu_{\text{S-H}}$ stretching mode of the mercaptopropyl segment present in MPTMS. Moreover, it is possible to observe a band at 651 cm^{-1} , that is assigned to the $\nu_{\text{C-S}}$ stretching mode [154]. The formation of bridged disulfide groups can be excluded due to the absence of modes in the $500\text{-}550\text{ cm}^{-1}$ spectral range [155]. Thus, it can be concluded that the thiol group is grafted to the SBA-15 material without any chemical alterations.

Raman spectra relative to samples after oxidation with H_2O_2 are very similar to each other and confirms the complete transformation of the thiol functionality into $-\text{SO}_3\text{H}$ groups according with thermal analyses (see the green, blue and red curves in Figure 5.7).

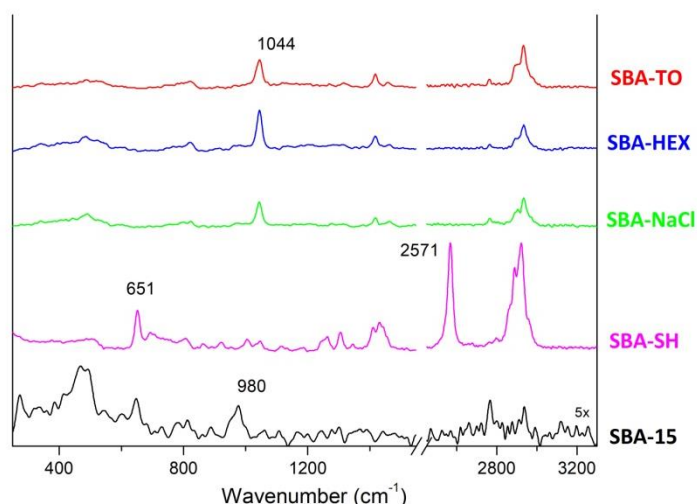


Figure 5.7 FT-Raman spectra of indicated samples

It is possible to observe the disappearing of the thiol stretching mode at $\sim 2570 \text{ cm}^{-1}$ with the parallel appearance of a new signal at 1044 cm^{-1} , assigned to the symmetric mode of the SO_3 group of the corresponding sulfonic acid [156]. On the contrary, the formation of disulphide species can be excluded also in the oxidized samples. In conclusion, the Raman technique allows to exclude the presence of unreacted thiols group and to verify the efficiency of H_2O_2 oxidation treatment.

5.2.2 Reactivity tests

After preliminary characterisations, catalytic tests were carried out. All these materials were tested through the hydrolysis reaction with two different substrates, glucose and fructose. The products yield and conversion of fructose and glucose are reported in Figure 5.8 section a) and b), respectively.

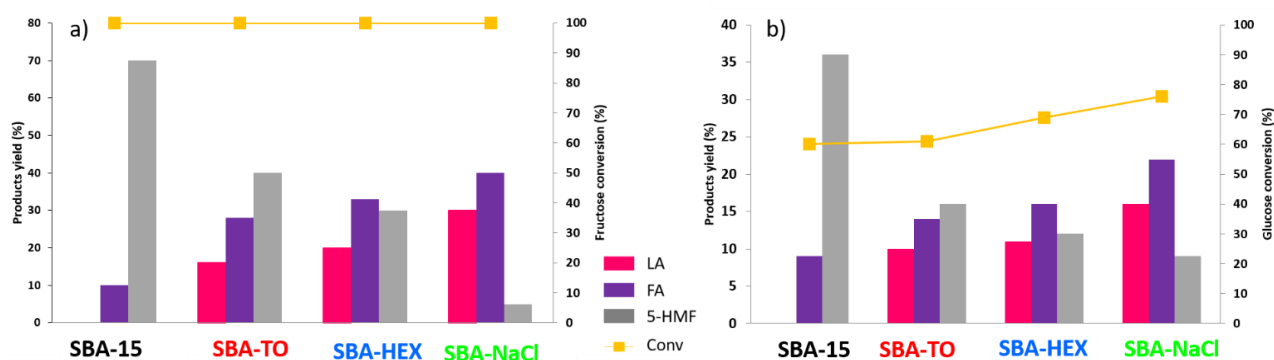


Figure 5.8 Substrate conversion (Section a): Fructose, Section b): Glucose) and products yield as a function of different catalysts.

Reaction conditions: $180 \text{ }^\circ\text{C}$, 10 Bar of N_2 for 7 h.

As reported by Ramli *et al.* [157], glucose isomerization to fructose is the rate determining step of the glucose hydrolysis reaction. Therefore, as evident in section a) of Figure 7.8, 100% of conversion has been obtained for all the catalysts using fructose as substrate. The main differences between them can be found in the products yield. For pristine SBA-15, no levulinic acid is produced. SBA-15, as previously reported, owns an intrinsic Lewis acidity given by the silanols functionalities, whereas the absence of Brønsted acid sites does not allow the hydration of 5-HMF, the main intermediate, to LA. On the contrary, the reaction is completed while using sulfonated materials. For both SBA-TO and SBA-HEX a very similar behaviour can be observed, whereas SBA-NaCl reaches to the 30 % of LA yield, 40 % of FA yield and only 6 % of 5-HMF yield. In this last case, hydration of 5-HMF to LA is favoured in comparison with the catalysts prepared in non-polar solvents. Similar trend has been found for glucose hydrolysis, as reported in section b) of Figure 5.8. Firstly, it must be pointed out that, no complete conversion is ever achieved using glucose as substrate. As reported in Figure 1.6 in Chapter 1, Brønsted acid sites, which in these catalysts are provided by the presence of sulfonic acid groups, are fundamental to bring to completeness the reaction. At the same time, Lewis acidity is necessary to convert glucose to fructose; nonetheless, in these catalysts, only small amounts of Lewis acid sites are present. Therefore the glucose conversion cannot reach the value of 100 %. Nonetheless, the maximum value (80 %) is obtained with SBA-NaCl. In addition, SBA-NaCl exhibits the highest LA yield and the lowest amount of 5-HMF. Although the sample prepared in saline solution SBA-NaCl shows higher activity in levulinic acid production than the other studied catalysts, it does not have an activity comparable to the most zeolite catalysts. Indeed, Ramli *et al.* present the activity of Fe/HY zeolite in glucose conversion at 180 °C which reaches the value of 100 % and 65 % of hydrogen yield after 4 hours of reaction [96]. Meanwhile, working with Amberlyst-15, as the other ion exchange resins, cannot guarantee a high glucose conversion since they consist of macroreticular pore structure with strong Brønsted acid sites only. Therefore, as it is observed with the studied catalysts, the absence of Lewis acid sites cannot allow an efficient glucose conversion. Temperatman *et al.*, introduced transition metals from transition metal groups into Amberlyst-15 to improve the glucose conversion from 10 % to 70 % at 120 °C [158]. Despite these considerations, it is important to note that the best-considered catalyst is the one prepared in the greenest and cheapest solution. For this reason, in order to understand the role of the solvent in the catalytic results, the acidity of the samples was evaluated by both titration and FTIR with a basic probe molecule.

5.2.3 Acidic properties

Table 5.2 summarizes the evaluation of the acidic properties of the SBA-based materials.

Table 5.2 Acidic properties of pristine and grafted SBA-15(^aRatio between Lewis and Bronsted acid sites calculated on normalized spectra using $\epsilon_L=1.9$ and $\epsilon_B=7.9$ and ^b Acid capacity (mmol/g) calculated via titration method)

	Acid capacity (mmol/g) ^b	L/B ^a
SBA-15	-	∞
SBA-NaCl	10	1.6
SBA-HEX	6.4	1.9
SBA-TO	7.8	1.8

For the total acidity, evaluated by titration method, the material prepared in saline solution (SBA-NaCl) presents the highest value followed by the catalyst prepared by using the most traditional solvent, toluene. It is important to underline that; this test gives only a roughly determination of acidity without properly distinguishing between Lewis and Brønsted acid sites. In order to investigate both kinds of acidity of the catalysts, FTIR adsorption of 2,6-dimethylpyridine (2,6-DMP) was carried out at ambient temperature. FTIR spectra of 2,6-DMP adsorbed on all samples are presented in figure 5.9, in the spectral range of signals ascribable to 8a and 8b modes of 2,6-DMP following a well-accepted procedure reported in the literature [159].

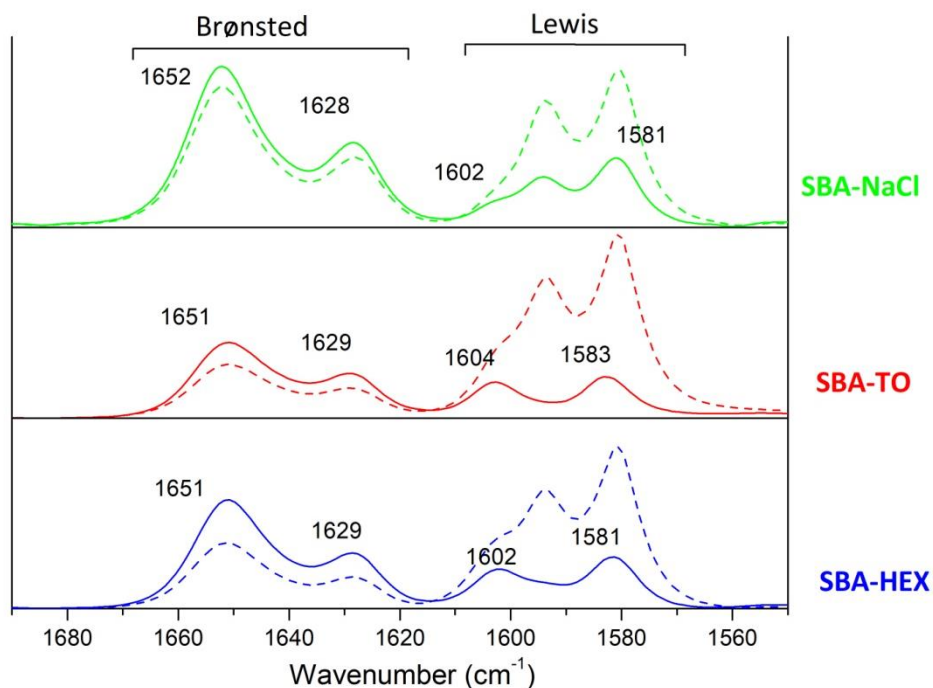


Figure 5.9 FT-IR spectra of adsorption/desorption of 2,6-DMP (dash line under maximum pressure of 2,6-DMP, line after evaluation for 15 min) for SBA-HEX, SBA-TO and SBA-NaCl.

In all the samples, 2,6-DMP adsorption/desorption spectra suggest the presence of Brønsted acidic sites. As can be seen, the intensity of signals at ~ 1650 and 1630 cm^{-1} increase in intensity after evacuation for 15 minutes. At lower wavenumbers, 8a and 8b modes of physisorbed and H-bonding 2,6-DMP (1604 , 1595 and 1580 cm^{-1}) are detectable: only existing signals after evacuation are attributable to Lewis acid sites of medium-high strength, as these are more strongly held at the surface. On the contrary, 2,6-DMP adsorption on SBA-15 (not shown for the sake of brevity) reveals the presence of only Lewis acidic sites, but no signals related to the Brønsted centers are detectable which is in good agreement to the data in the literature about silica-based materials. As already reported in section 5.2.2 for what concerns glucose/fructose hydrolysis, selectivity is influenced by both strength and number of Lewis and Brønsted acid sites. Thus, the ratio between Lewis and Brønsted acidic sites (L/B) could play a key role in the determining of the best catalyst. The estimation of (L/B) ratio requires the knowledge of molar absorption coefficients (ϵ) values, specific for each vibrational mode considered and influenced by the surface. Some studies suggest that a little variation of ϵ as a function of the type of solids and estimated ϵ values for 2,6-DMP adsorbed through H-bonding, coordination and protonation [160]. To minimize errors derived from average values (reported approximately to be 18%), the molar absorption coefficient determined for the 8a and 8b modes on similar materials (silica and phosphate silica) have been taken into account. Calculated L/B ratios for the SBA-based

samples (reported in Table 5.2) are higher than unity for all samples suggesting a prevalence of Lewis acidity. However, the differences among samples are quite evident. Samples treated with non-polar solvents, present similar values while in the case of saline solution the lower value of this ratio suggests an higher amount of Brønsted acid sites. These results agree with the acid capacity obtained via titration method in which the L/B ratio decreases with the increase of acid capacity.

Preliminary characterisations and acid properties analyses allow to discriminate the effect of solvents. The solvent has a critical role in the grafting process. Usually, it has been chosen to be inert towards the nucleophilic substitution (NS) step to not compete with the grafting reagent. Nevertheless, nucleophilic substitution occurs in the terminal silanol sites. These sites are not completely available in the system since SBA-15 undergoes a calcination process that eliminates water, creating siloxane bridges. Therefore, there is a decrease in the possibility of NS and as consequence on the number of grafted molecules. The effect of solvent and water/NaCl solution can be found in this step. As previously described by Pirez *et al.* [161] NaCl can activate the siloxane bridges, restoring a suitable number of free Si-OH in the presence of Cl⁻ fostering the nucleophilic substitution with MPTMS. Therefore, in comparison with non-polar traditional solvents, it increases the number of sulfonated molecules over the surface leading to the higher Brønsted acidity. The catalytic results are in good agreement with what is obtained from acidity characterizations. Therefore, a direct correlation between catalyst acidity (L/B) and LA yield is evidenced. Indeed, SBA-NaCl, exhibiting the highest total acid capacity, besides the lowest L/B ratio, can promote the last stage of reaction, ruled by Brønsted acidity, reaching the highest LA yield. Moreover, from an environmental point of view, the use of the saline solution, in comparison with the most traditional non-polar solvents, is more eco-friendly, cost-effective and it is greener.

5.3 Conclusions

Herein, sulfonic acid SBA-15 materials were successfully developed for the conversion of glucose to LA. Materials were prepared via post-synthesis grafting using three different solvents: toluene, hexane and water/NaCl. The effect of the solvents was evaluated pointing the attention on morphological, structural features and acidic properties. It was found that the grafting approach partially affects the ordered mesoporous organization, still preserving a good order degree. However, the success of grafting procedures strongly depends on the solvent effect. Indeed, the use of saline solution, in comparison with non-polar traditional solvents, leads to an increase in the number of sulfonated molecules over the surface with higher Brønsted acidity. This evidence exhibits a direct effect on catalytic activity in the glucose and fructose hydrolysis. The best catalytic results were obtained for both reagents using water/NaCl as a grafting solvent. Indeed, this material favours the rehydration reaction of 5-HMF, leading to the highest LA yield. 30 % of LA yield from fructose and 16 % from glucose have been achieved at 180 °C. Therefore, it is possible to increase the efficiency of post-synthesis grafting approach using a sustainable, economic and environmentally friendly solvent. Despite the promising results, the glucose conversion and LA yield values are not comparable to the common catalysts presented in the literature such as zeolites or ion-exchange resins. As mentioned above, this behaviour is due to the reduced number of Lewis acid sites which do not allow a complete conversion of glucose. For this reason, in Chapter 6, the acidic properties of SBA-NaCl have been further implemented by the addition of Lewis acid sites.

Chapter 6. Modification of physical-chemical and catalytic properties of SBA-15 by Al addition

The work reported in this chapter was performed at the Abo Akdemy University in Turku under the supervision of Prof. Tapio Salmi and Prof. Dmitry Y. Murzi. The attention was focused on the implementation of Lewis acidity of SBA-15 by the incorporation of alumina. Herein, two different synthetic procedures were considered for aluminium introduction. Indeed, co-precipitation and evaporation impregnation were studied using aluminium isopropoxide and aluminium nitrate, respectively. Moreover, the post-synthesis grafting method, developed and studied in Chapter 5 was applied to the new material for the introduction of Brønsted acid sites. Direct synthesis turned out not to be a reliable method for silica and alumina interactions. After the identification of the best method for alumina introduction, materials with different Si/Al ratios were prepared: 20, 25 and 30, respectively. The effect of Si/Al ratio on the acidity and morphological features of the materials was evaluated using XRD, N₂-physisorption, pyridine FT-IR and ²⁷Al-NMR. Moreover, catalytic tests in the glucose hydrolysis at 180 °C were performed. The best catalytic results in terms of glucose conversion has been obtained with the SBA-15 with Si/Al ratio of 25. Hence, by the implementation of Brønsted acidity via the post-synthesis grafting method, 90 % of glucose conversion and 50 % of LA yield was obtained.

6.1 Experimental

6.1.1 Catalyst preparation

- *SBA-15 synthesis*: Mesoporous SBA-15 was synthesized according to Zhao *et al.* using TEOS (Tetraethyl orthosilicate) as silica source, P123 (EO₂₀-PO₇₀-EO₂₀) as template in acid solution[162]. The mixture was continuously stirred for 20 h at 25 °C and crystallized in a Teflon autoclave at 90 °C for 24 h. The mixture was then filtered, washed, dried at 80 °C for 24 h and finally calcined in air (50 mL/min) at 500 °C for 6 h.
- *Introduction of alumina*
 - 1) Direct synthesis method: As for SBA-15 synthesis, aluminium isopropoxide (Al[OCH(CH₃)₂]₃ Sigma Aldrich) was used as alumina precursor and it was introduced in the template acid solution after TEOS addition in order to obtain SiO₂/Al₂O₃ = 35. The mixture was continuously stirred for 20 h at 25 °C and crystallized in a Teflon autoclave at 90 °C for 24 h. The mixture was then filtered, washed, dried at 80 °C for 24 h and finally calcined in air (50 mL/min) at 500 °C for 6 h. The final catalyst was labelled SBA-Al-DS.

- 2) Evaporation-impregnation method: Alumina was introduced to SBA-15 by evaporation impregnation method. The various amounts of $\text{Al}(\text{NO}_3)_3 \cdot 9\text{H}_2\text{O}$ (Sigma-Aldrich), were dissolved in 250 mL of water, to prepare materials with $\text{SiO}_2/\text{Al}_2\text{O}_3$ ratio as 35, 32 and 30. After the complete dissolution of the salt, SBA-15 was added to the solution and stirred at 60 °C for 24 h. The mixture was evaporated *in vacuum* at 60 °C. The obtained powder was calcined at 500 °C for 6 h. The final catalysts were labelled SBA-Al-EI-x, where x is the ratio between SiO_2 and Al_2O_3 .
- *Grafting sulfonic groups*: A post-grafting method was used to functionalize the selective promoted-SBA-15 material. 1 g of SBA-15 was dissolved in 30 mL of saline (NaCl) solution 0.2 M. MPTMS was added in the mixture exhibiting 2:1 molar ratio of SiO_2 to 1MPTMS and the mixture was stirred for 24 h at 90 °C. The solid was then washed in water (three portion of 20 mL) and dried for 18 h at 70 °C. Then, mild oxidation with 30 wt% H_2O_2 using 2:0.11 molar ratio of SiO_2 to H_2O_2 was performed stirring for 24 h at 30 °C. The sulfonated solid was filtered, washed with methanol and dried at 25 °C for 18 h. The final catalyst was labelled SBA-Al-EI-x- SO_3H .

6.1.2 Catalyst characterizations

N_2 -physisorption was performed as reported in section 2.1.2 of Chapter 2, while XRD was carried out as reported in section 3.1.2 of Chapter 3.

Scanning electron microscopy (Zeiss Leo Gemini 1530) was used to study the crystal morphology of the Al-SBA-15 mesoporous materials synthesized using different methods of aluminium grafting. Energy dispersive X-ray micro-analyses (EDX) attached to SEM was applied for quantitative elemental analyses.

Transmission electron microscopy was used to study the structure, pore size and periodicity of the SBA mesoporous catalysts. The instrument applied for the measurements was JEM 1400 plus with an acceleration voltage of 120 kV and resolution of 0.98 nm using Quems II MPix bottom mounted digital camera. The particle size distribution was measured by ImageJ software.

Characterization of the Brønsted and Lewis acid sites, their amount and strength were done using pyridine (Sigma Aldrich, $\geq 99.5\%$) adsorption-desorption. The measurements were performed with ATI Mattson FTIR using 10 mg of self supported catalyst pellets. The catalyst was activated in the IR cell by heating from room temperature to 200 °C under vacuum (1×10^{-4} Pa). In order to discriminate between weak, medium and strong acid sites, desorption of pyridine was performed at 150 °C, 250 °C and 350 °C, respectively. Quantification of Brønsted and Lewis acid sites was done

by considering intensity of IR signals at 1545 cm^{-1} and 1455 cm^{-1} , respectively, using the molar extinction factor given by Emeis.[163]

^{27}Al MAS-NMR spectra were recorded at 208.49 MHz on Bruker AVANCE-III spectrometer at 18.8 T external field using Bruker MAS probe for 3.2 mm zirconia rotors. The spectra were collected by single $0.6\text{ }\mu\text{s}$ pulse ($\pi/18$) excitation with repetition time 0.1 s at 22 kHz sample spinning frequency. The spectra are referenced to the frequency of AlNO_3 aqua solution. The intensity in the spectra was normalized to the number of accumulations and to the mass of the sample.

6.1.3 Catalytic test

The catalysts were tested for glucose hydrolysis in a stainless-steel autoclave (Parr Inc, USA). The temperature was measured with a thermocouple and automatically adjusted with an inbuilt temperature regulator (Parr4848 Reactor Controller). The autoclave was equipped with a gas inlet/sampling outlet fitted with $7\text{ }\mu\text{m}$ metal filter. Before the reaction, 500 mg of substrate, 100 mL of water and 500 mg of catalyst were loaded into the reactor and then heated to $180\text{ }^\circ\text{C}$ under 10 bar of N_2 . The initial time of the reaction was taken once the reaction temperature was reached. The reaction was carried out for 7 hours at 1000 rpm. Throughout the experiment, samples were taken at suitable intervals. At the end of the reaction, the mixture was cooled down to $25\text{ }^\circ\text{C}$ and separated by filtration. Final reaction mixture and every sampling were analysed by high performance liquid chromatography (HPLC) VWR HITACHI Chromaster, equipped by an Aminex HPX-87H column kept at $50\text{ }^\circ\text{C}$. 5450 RI detector was used for analytes' identification and quantification.

Reactivity parameters were calculated as follows:

$$\text{Conversion (\%)} = \frac{(\text{mmol sub in}) - (\text{mmol sub out})}{\text{mmol sub in}} \cdot 100$$

$$\text{Yield (\%)} = \frac{\text{mmol } i \text{ out}}{\text{mmol sub in}} \cdot 100$$

Where i represents a general product of reaction.

6.2 Results and discussion

6.2.1 Influence of Alumina introduction method

Small angle XRD patterns of the samples are presented in Figure 6.1. Pristine SBA-15 exhibits the three characteristic reflections at low angle typical of ordered mesoporous materials with a 2D-hexagonal $p6mm$ pore symmetry [164]. The peaks that appear at 0.95° , 1.64° and 1.85° , are associated with (100), (110) and (200) planes, respectively [102]. Concerning the alumina-silica materials (SBA-Al-DS and SBA-Al-EI), a partial loss in the mesoporous order is evident since the second and third peaks are completely disappeared in the final materials. Furthermore, the intensity of the reflection of the first main peak at 0.95° is attenuated in both promoted samples. Another interesting aspect is the shift of the main peak to lower angle in comparison with pristine silica, 0.81° for SBA-Al-DS and 0.92° for SBA-Al-EI. The shift is assigned to the introduction of alumina in the framework that reduces the ordered hexagonal symmetry [165].

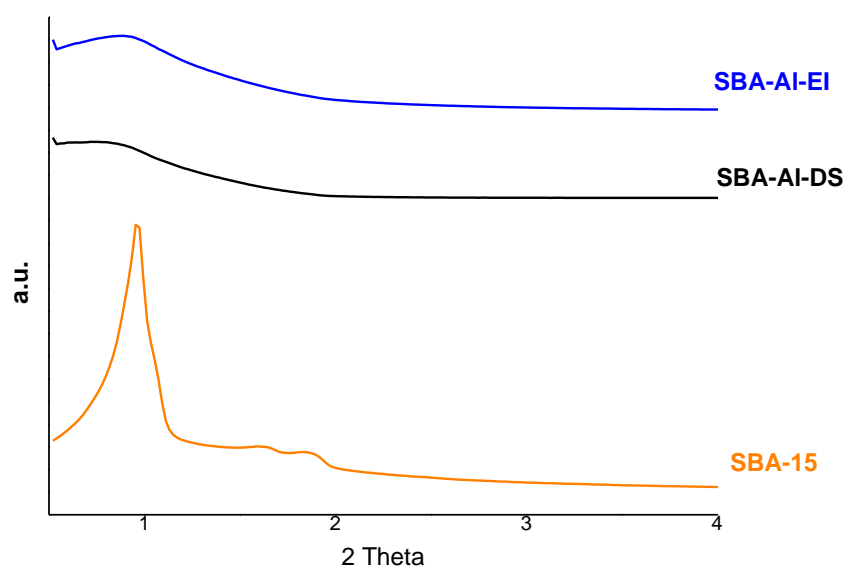


Figure 6.1 Low-Angle XRD patterns of SBA-15 and Alumina/SBA-15 catalysts.

Therefore, to understand the effective amount of alumina in the final materials, SEM coupled with EDX was performed. Figure 6.2 represents SEM images of aluminium modified SBA-15 mesoporous catalysts and Si/Al and $\text{SiO}_2/\text{Al}_2\text{O}_3$ ratios are reported in Table 6.1, calculated using energy dispersive X-ray-micro analyses. Both composites are made of spherical shaped particles (silica) and of bigger alumina agglomerates characterized by heterogeneous size and shape. Anyway, in the case of the SBA-Al-EI sample, the alumina nanoparticles are smaller and evenly distributed. Moreover, the two materials present a completely different ratio. In the case of evaporation-impregnation, the expected value ($\text{SiO}_2/\text{Al}_2\text{O}_3$ 35) is partially respected; in contrast, the material prepared via direct synthesis presents a completely different ratio than predicted. As a matter of fact, the preparation method

strongly affects not only the material's morphology but also the effective possibility to introduce the desired amount of promoter.

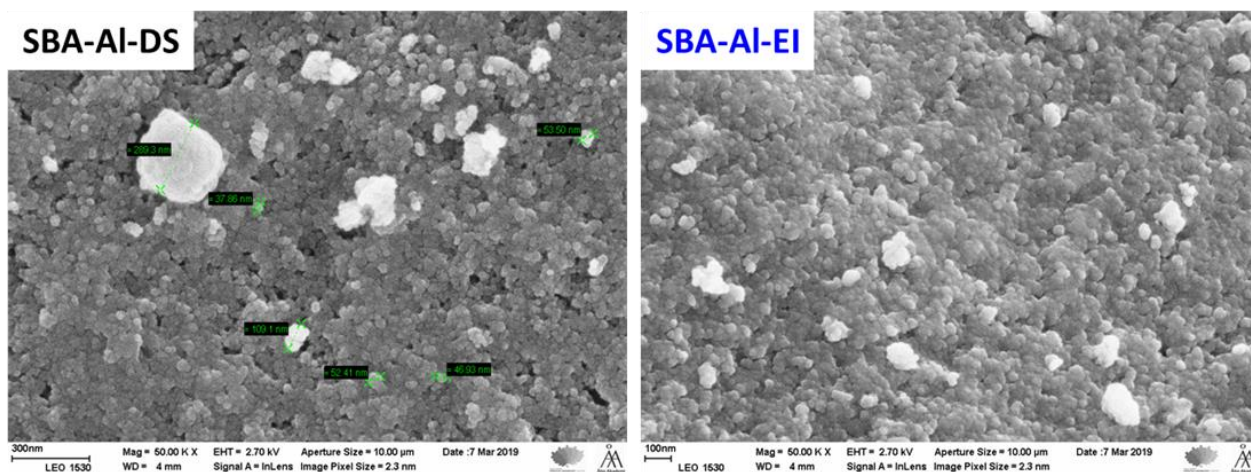


Figure 6.2 SEM images of SBA-Al-DS and SBA-Al-EI

N_2 -physisorption was performed to evaluate the surface area, pore volume and pore size distributions of SBA-15 catalysts. The isotherms of the three samples and the corresponding BJH pore size distributions are reported in Figure 6.3.

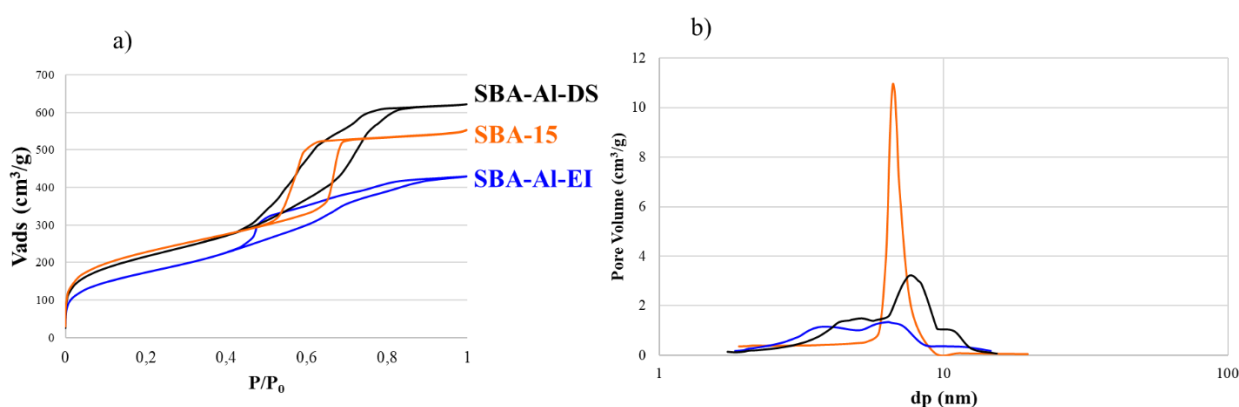


Figure 6.3 N_2 adsorption-desorption isotherms (section a) and BJH pore size distribution (section b) of SBA-15 and Alumina/SBA-15 catalysts.

All SBA-15 samples exhibit type VI isotherm curves with the characteristic hysteresis loop of mesoporous materials [166]. SBA-15 shows the H1 hysteresis shape with a sharp pore size distribution centred at 6 nm, characteristic of ordered material with a bottle-necked pore opening [167]. For the modified materials, as already evidenced in the small-angle XRD patterns, the order is partially lost since the hysteresis shape is more irregular, with a wide and uneven distribution of the pore diameter. In both doped materials, H3-type hysteresis is centred between the P/P_0 of 0.4 and 0.8 with a broader distribution for SBA-Al-EI catalyst. Indeed, looking at the data reported in Table 6.1, evaporation-impregnation technique seems to strongly affect the surface area, leading to a decrement

of almost 200 m²/g from the pristine catalyst. Besides, it is visible an increase in mean pore diameter for direct synthesis catalyst, from 5 nm of pristine SBA-15 to 5.2 nm of promoted material. As already mentioned by Vinu *et al.*[168] isopropanol, that is formed in the reaction mixture, can enter in the P123 micelles and increase their size; in consequence the material pores are enlarged. The highest surface area (812 m²/g), Table 6.1, was obtained for pure SBA-15 mesoporous material. However, modification with Al using direct synthesis and evaporation impregnation methods resulted in decrease in the surface area. The decrement in the surface area can be attributed, independently from the formulation approach, to the pore blockage of SBA-15 with Al₂O₃ nanoparticles during the modification with Al.

Table 6.1 Textural and structural properties of solid catalysts (^a Specific surface area, ^b Pore volume, ^c Average pore diameter, ^d silicium/aluminium ratios and ^esilica/alumina ratio)

Sample	S _{BET} (m ² /g) ^a	V _p (cm ³ /g) ^b	d _p (nm) ^c	Si/Al ^d	SiO ₂ /Al ₂ O ₃ ^e
SBA-15	812	0.80	5	-	-
SBA-Al-DS	770	0.96	5.2	483	587
SBA-Al-EI	621	0.66	4.6	29	35

Transmission electron microscopy (TEM) was used to deeply investigate the textural properties, pore dimensions, porosity of all modified SBA-15 mesoporous materials. Nanoparticles dimension of Al₂O₃ was also measured using TEM. Transmission electron micrographs of SBA-Al-DS and SBA-Al-EI mesoporous materials are reported in Figure 6.4. Ordered mesoporous materials are typically characterised by the 2-D hexagonal mesostructures. Mapping different area for those samples, 2D periodic hexagonal appear randomly, meaning that the structure is partially affected. These results are well in agreement with small-angle XRD patterns and N₂-physisorption. Moreover, in TEM images, small alumina agglomerates are clear; those particles are big and isolated in the material prepared via direct synthesis (SBA-Al-DS) and small and homogeneously dispersed in the evaporation-impregnation one (SBA-Al-EI), as already seen by SEM technique.

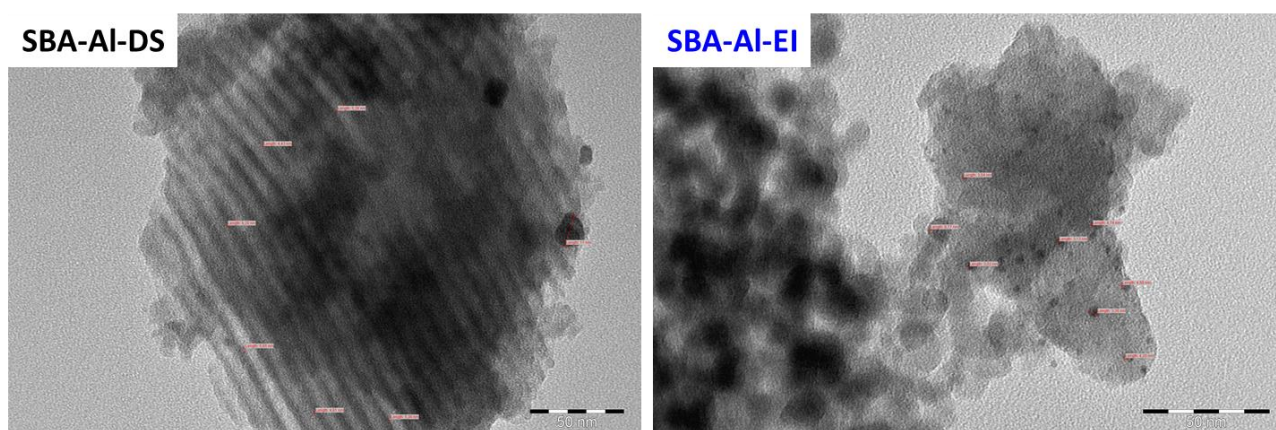


Figure 6.4 TEM images of SBA-Al-DS and SBA-Al-EI

The obtained results suggest that evaporation-impregnation technique seems to be the best method for the preparation of doped alumina-SBA-15. Indeed, in the case of direct synthesis, the introduction of alumina precursor has affected the synthetic environment, impacting on the structural and morphological features of final material; moreover, it has not allowed to reach the expected $\text{SiO}_2/\text{Al}_2\text{O}_3$ ratio, leaving only small alumina deposit over the surface. For this reason, the direct synthesis has been abandoned and the work has been deepening inside the evaporation-impregnation approach. This method allows to successfully insert alumina in SBA-15 achieving the right $\text{SiO}_2/\text{Al}_2\text{O}_3$ ratio. Moreover, this synthetic approach affects the morphology of the final material only in part, by well preserving the original features of the silica support.

6.2.2 Influence of aluminium amount

After the determination of the best methodology for alumina incorporation in SBA-15, the investigation of the effect of alumina content was carried out. As already mentioned in the introduction part (section 1.5.1), alumina was selected as a promoter for SBA-15 to create Lewis-Brønsted acid sites on the silica surface. For this reason, three different alumina amounts, to prepare material with SiO₂/Al₂O₃ ratio as 35, 32 and 30, were evaluated.

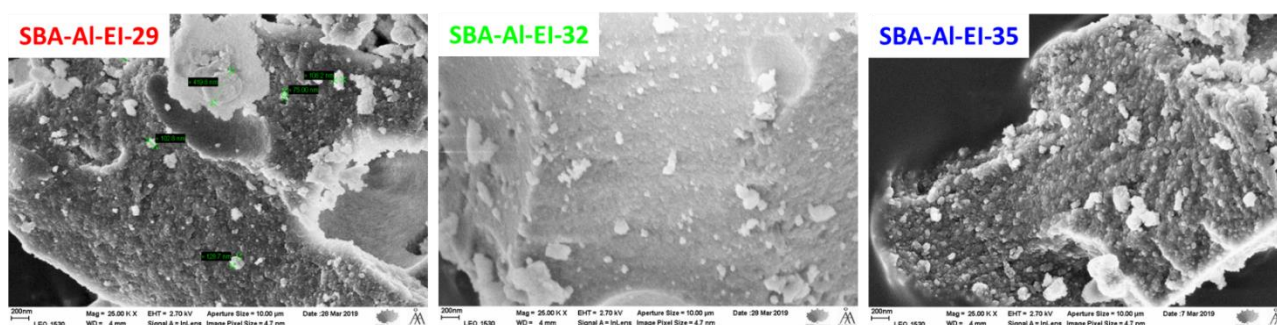


Figure 6.5 SEM images of SBA-15 mesoporous materials synthesized with different Si/Al ratios

First, the real amount of alumina in the final catalysts was determined using EDX; in this case, direct correlation between nominal and effective amount is respected and data are reported in Table 6.2.

Table 6.2 Textural and structural properties of different SiO₂/Al₂O₃ catalysts (^a Specific surface area, ^b Pore volume, ^c Average pore diameter, ^d Silica/Alumina ratio)

Sample	S _{BET} (m ² /g) ^a	V _p (cm ³ /g) ^b	d _p (nm) ^c	SiO ₂ /Al ₂ O ₃ ^d
SBA-15-Al-29	548	0.75	4.8	29
SBA-15-Al-32	627	0.68	4.6	32
SBA-15-Al-35	621	0.66	4.6	35

Figure 6.6 reports XRD patterns of different Si/Al ratio catalysts. As already observed for SBA-Al-DS and SBA-Al-EI, the different Si/Al ratio catalysts have partially lost the surface order as well. Indeed, only the first diffraction peak at 2θ 0.90 ° appears. No significant difference in intensity can be noted while a shift in the diffraction angle is perceptible. As reported by Xing *et al.* [108], when alumina is introduced inside the framework, reduction of the segmental ordered hexagonal symmetry appears. In this case, no direct correlation between alumina amount and the diffraction angle can be correlated. 0.85°, 0.9 ° and 0.88 ° are the diffraction angles of SBA-Al-EI-29, SBA-Al-EI-32 and SBA-Al-EI-35, respectively. At the same time, this small difference can suggest a diverse introduction of alumina: in the framework or extra framework.

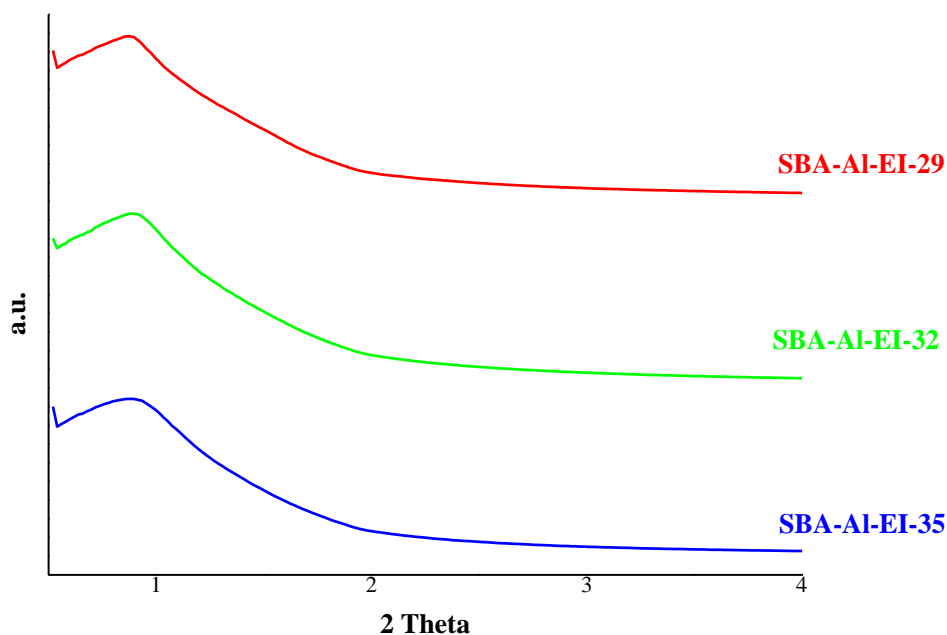


Figure 6.6 XRD patterns for different $\text{SiO}_2/\text{Al}_2\text{O}_3$ catalysts

Considering N_2 -physisorption, all samples present type VI isotherm curves with H3 hysteresis shape. The range of hysteresis is broad, from 0.4 to 0.8 which agrees with the BJH pore size distribution reported in Figure 6.7, section b. At the same time, SBA-Al-EI-32 and SBA-Al-EI-35 are more similar to each other than SBA-Al-EI-29. As it can be seen, the hysteresis curves are almost overlapping. Moreover, SBA-Al-EI-29, having the highest alumina content, appears with the lowest surface area (see Table 6.2). In this case, such marked differences can be attributed not only to the higher amount of alumina but also to its position inside/outside the silica lattice. The highest surface area ($627 \text{ m}^2/\text{g}$), Table 6.2, was obtained for the SBA-15-Al-32 mesoporous catalysts, whereas the lowest surface area was obtained for SBA-15-Al-29 ($548 \text{ m}^2/\text{g}$). The plausible explanation for such low surface for SBA-15-Al-29 mesoporous catalyst is the blocking of pores by large nanoparticles of Al_2O_3 , furthermore, such decrease in surface can also be combined with the partial loss of the mesoporous order.

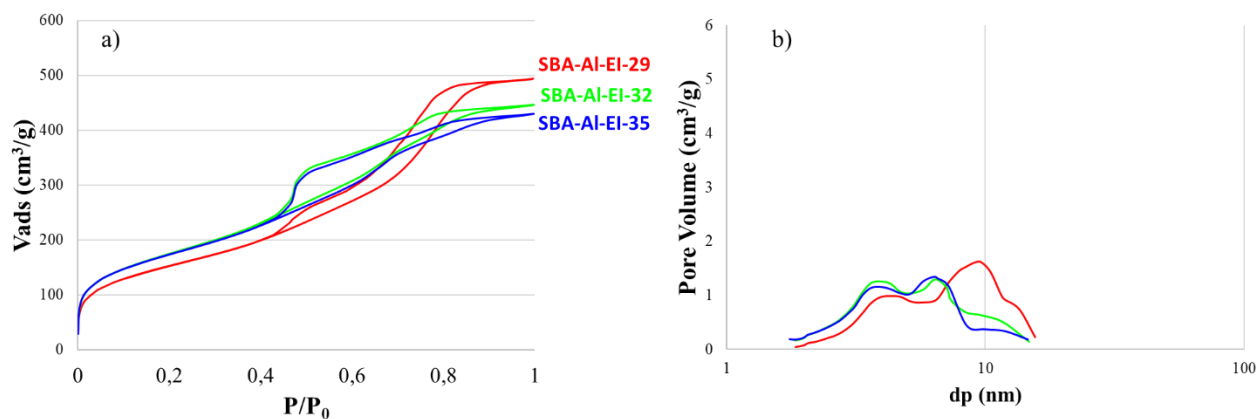


Figure 6.7 N_2 adsorption-desorption isotherms of SBA-15 and Alumina/SBA-15 catalysts and BJH pore size distribution.

TEM analyses were also carried out in the different Si/Al evaporation-impregnation catalysts to confirm the preservation of the ordered mesoporous structure. As visible in Figure 6.8, all catalysts exhibit the channel pore structure with characteristic order.

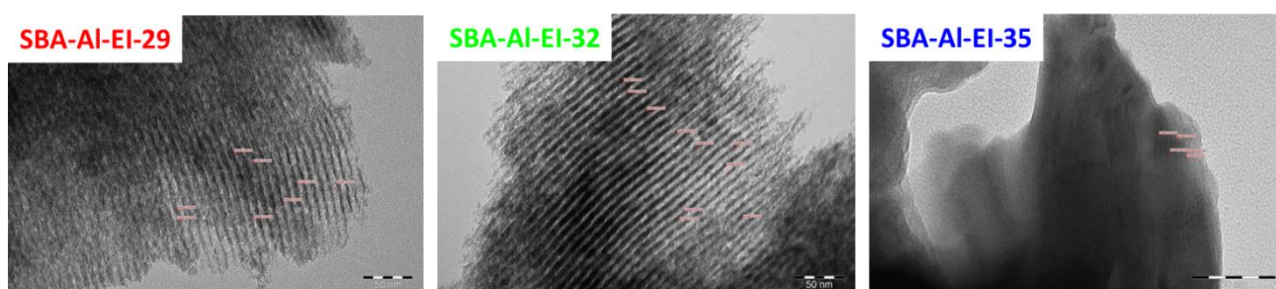


Figure 6.8 TEM images of different SiO_2/Al_2O_3 evaporation-impregnation catalysts.

After the evaluation of morphological and structural properties, surface acidity study was performed. Table 6.3 summarises the concentration and the types of acid sites, determined by FTIR spectroscopy of pyridine adsorption in the spectral range of $1400-1575\text{ cm}^{-1}$. For each catalyst, the concentration of Brønsted and Lewis acid sites at different temperature is reported. The higher the temperature of the analysis, the stronger the site [169]. As it is reported in Table 6.3, the catalyst with the highest amount of alumina (SBA-Al-EI-29) has the lowest number of sites at each temperature, with no acid sites at $350\text{ }^\circ\text{C}$. SBA-Al-EI-32 and SBA-Al-EI-35, unlike SBA-Al-EI-29, have shown strong Lewis acid sites. Particularly, SBA-Al-EI-32 has shown the highest concentration of medium and strong Lewis acid sites at 250 and $350\text{ }^\circ\text{C}$, respectively. For all the catalysts, no Brønsted acid sites are present at high temperature. As a rule, as the aluminium content increases, the amount of sites increases at the detriment of its strength [170]. This fact is not in agreement with the obtained results since the higher amount of medium and strong acid sites is found in the sample with the intermediate amount of alumina. Even in this case, it can be hypothesised that the effect is strongly connected with alumina coordination.

Table 6.3 Concentration of Brønsted acid sites (B) and Lewis acid sites (L) in the SBA-15 mesoporous catalyst with different SiO₂/Al₂O₃ catalysts determined with FTIR-pyridine method. Concentration expressed in μmol/g

T(°C)	SBA-Al-EI-29			SBA-Al-EI-32			SBA-Al-EI-35		
	C _B	C _L	Total	C _B	C _L	Total	C _B	C _L	Total
150	19	33	52	26	44	70	27	74	101
250	10	19	29	17	24	41	16	17	33
350	0	0	0	0	4	4	0	2	2

In conclusion, alumina has been successfully introduced inside SBA-15 lattice and the required aluminium amount has been obtained in the final catalysts. As expected, aluminium amount influences morphological and structural features of the final materials. The catalyst with the highest amount of alumina SBA-Al-EI-29 presents the most different properties. It has the lowest surface area with different hysteresis shape and the lowest amount of acid sites. Considering the other two samples, only slight changes in properties can be observed. Among them, the most important feature is the presence of strong Lewis acid sites in the intermediate alumina sample SBA-Al-EI-32. Indeed, in contrast to what expected, the most acidic samples are those with the lowest aluminium content. This is probably due to the coordination of the aluminium ion. Therefore, determination of Al coordination in the studied materials was performed using ²⁷Al-NMR. Figure 6.9 reports all the spectra. Each spectrum was decomposed by 5 Gaussian lines. For the three samples, the most significant peak is around 54 ppm which is typical for tetrahedrally coordinated AlO₄ groups. A broad line around 35 to 40 ppm and the broad weak line at 17 ppm can be assigned to 5- coordinated Al sites. The resonance near 3,-4 ppm belong to octahedral 6 coordinated Al sites.

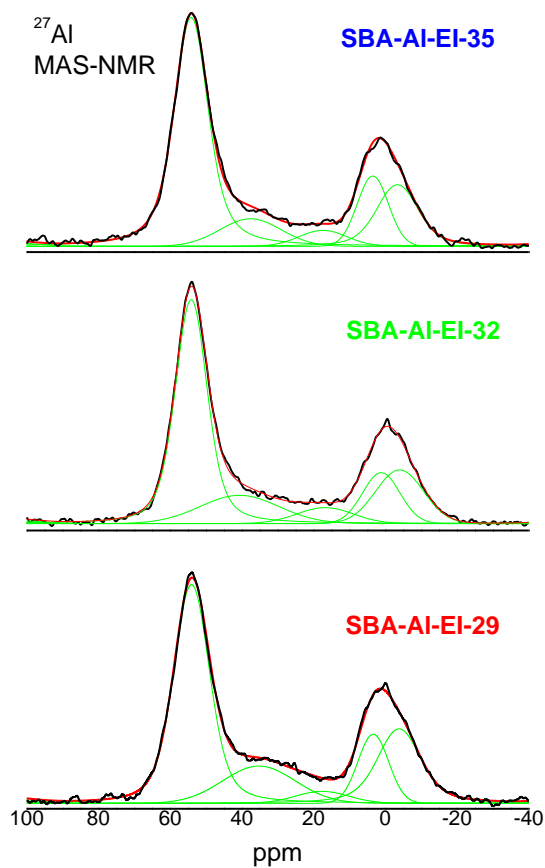


Figure 6.9 ^{27}Al MAS-NMR spectra of different Si/Al ratio catalysts.

Table 6.4 Relative contribution of different forms of Al calculated via ^{27}Al -NMR

Samples	^{27}Al -NMR		
	Al (IV) %	Al (V) %	Al (VI) %
SBA-Al-EI-29	49.3	18.2	32.5
SBA-Al-EI-32	52.6	19.5	27.9
SBA-Al-EI-35	55.7	14.3	30

Table 6.4 summarises the relative contribution of the different forms of Al. It can be noted that the relative number of tetrahedral Al (IV) sites gradually increases with decreasing the Al content in expense of the extra-framework Al (V) and Al (VI) sites. Nevertheless, the distribution of Al (V) and Al (VI) does not follow the same trend. Indeed, the intermediate sample SBA-Al-EI-32 has the lowest amount of extra-framework octahedral Al sites [170]. Moreover, the total number of Al sites is varying as 107:93:100 for SBA-Al-EI-29: SBA-Al-EI-32: SBA-Al-EI-35, respectively. Indeed, the material with the highest number of strong and medium acid sites is the one with the lowest octahedral Al and the lowest total number of sites. Therefore, this result justifies the unexpected acidity of SBA-Al-EI-32. To further confirm this trend, catalytic tests were carried out.

6.2.3 Reactivity

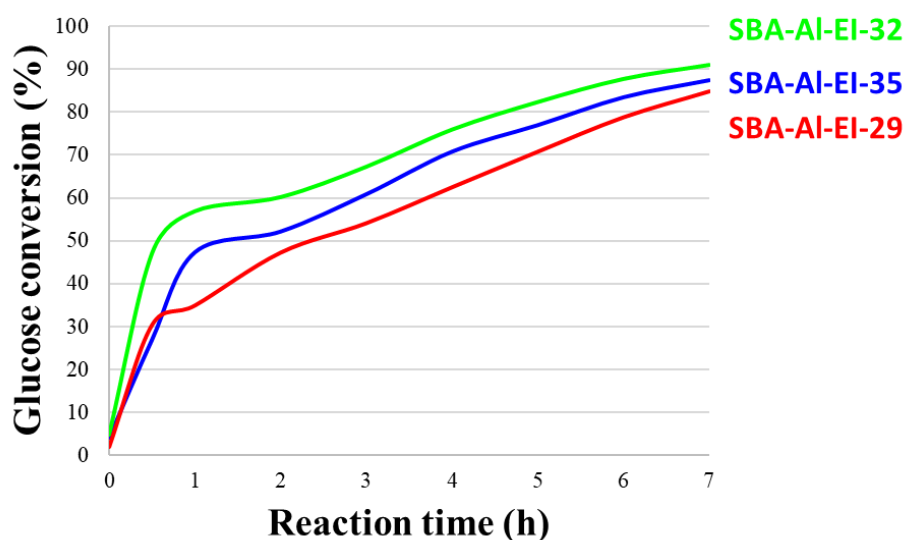


Figure 6.10 Glucose conversion over time for different $\text{SiO}_2/\text{Al}_2\text{O}_3$ catalysts

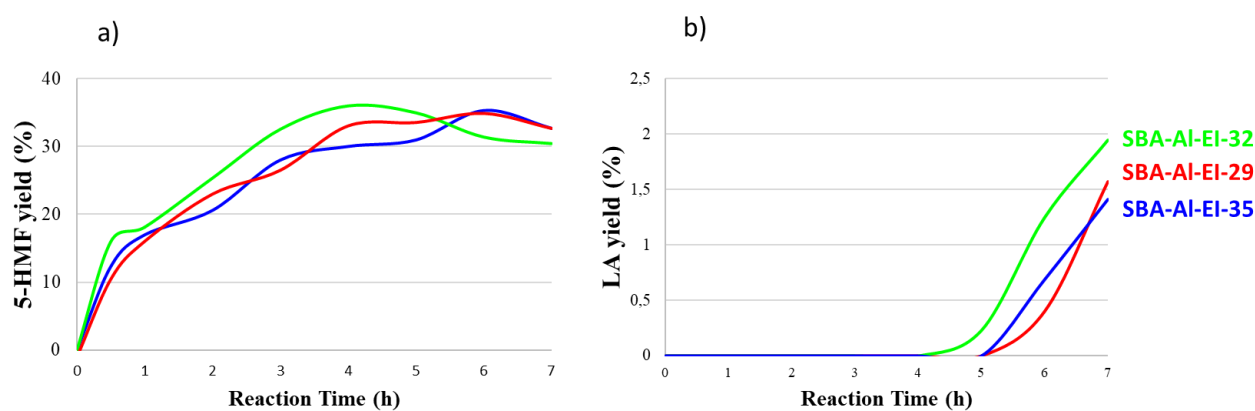


Figure 6.11 5-HMF yield (section a) and Levulinic acid (LA) yield (section b) over time for different $\text{SiO}_2/\text{Al}_2\text{O}_3$ catalysts.

After preliminary characterizations, reactivity tests were carried out. Silica-alumina materials with different Si/Al ratio were tested in the glucose hydrolysis reaction, studying the kinetic. Glucose conversion is reported in Figure 6.10 while Figure 6.11 shows 5-HMF and LA yield vs reaction time. Considering glucose conversion, the three samples exhibit similar profiles; in the first hour of reaction, the slope of the curve is more inclined than the remaining curve, indicating a higher reaction rate at the beginning. Nevertheless, SBA-Al-EI-32 has almost 60 % of conversion after one hour of reaction, reaching 90 % after 7 hours. The conversion of SBA-Al-EI-35 and SBA-Al-EI-29 reach almost 87 and 84 %, respectively. Parallel to the highest glucose conversion achieved, the catalyst

SBA-Al-EI-32 allows obtaining even the highest percentage of LA. Indeed, considering Figure 6.11, section b), LA starts to be produced after 4 hours of reaction, reaching the yield of 2 % in 7 hours. Besides, the quantitative amount of the desired product is modest and most of the glucose is converted into 5-HMF, as visible in section a) of Figure 6.11. As already mentioned in the introduction part, 5-hydroxymethyl-2-furandehyde is the intermediate of C6-sugar decomposition, which is subsequently rehydrated to give levulinic acid and formic acid [171]. Lewis acid sites catalyse the isomerization of glucose to fructose and the subsequently dehydration to 5-HMF, while Brønsted acid sites are responsible for the last re-hydration reaction. For this reason, only a small amount of LA has been produced in this reaction condition. As already noted with the FTIR-Pyridine test, these catalysts have a small amount of weak and medium Brønsted acid sites with no strong sites.

SBA-Al-EI-32 leads to the highest glucose conversion in time and the highest 5-HMF yield in the first 4 hours of reaction. Indeed, at hour 4, a slight conversion of the intermediate to levulinic acid appears. This promising result can be attributed to Lewis' strong acidity of the material, which possesses the highest concentration of Lewis acid sites of medium and strong strength. At the same time, as appropriate LA yield was not achieved, further modification of this promising material was carried out.

6.2.5 Incorporation of Brønsted acid sites

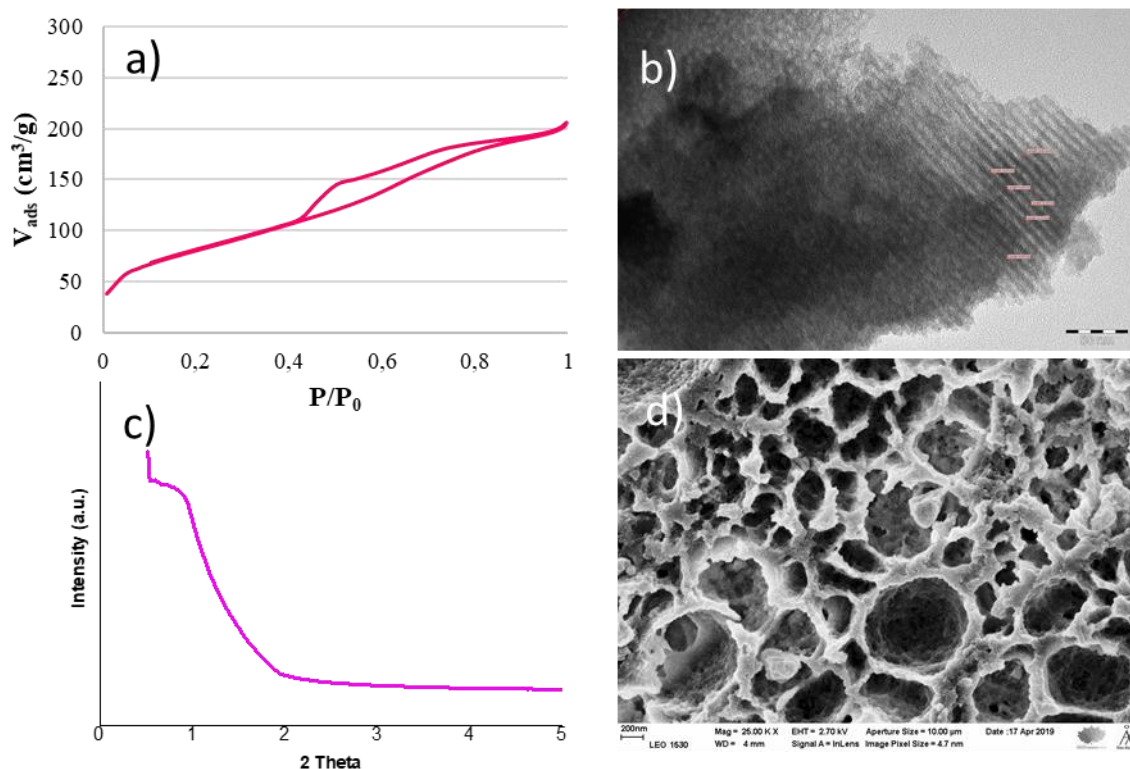


Figure 6.12 Characterisation of SBA-Al-EI-32-SO₃H: section a) N₂-physorption, section b) TEM, section c) low-angle XRD and section d) SEM.

Increment of Brønsted acid sites was achieved using post-synthesis grafting method, following the method reported in Chapter 5. The new material, SBA-Al-EI-35-SO₃H, was fully characterized via N₂-Physorption, TEM, small-angle XRD and SEM-EDX. Figure 6.12 summarizes all the characterizations; as visible, grafting procedure affects the morphological and structural feature of the material. Surface area is decreased from 627 to 294 m²/g and SEM image of the new sample appears completely different from the not-grafted one. Nevertheless, partial order and mesoporous structure are still preserved. XRD pattern presents the typical peak of SBA-15 at 2θ of 0.84° while TEM image shows the characteristic pore channels. As before, the most important aspect to be evaluated is the study of the amount and kind of acid sites. For this reason, to determine the efficiency of the grafting method in increasing Brønsted sites concentrations, FT-IR spectroscopy by using pyridine as probe molecule was performed.

Table 6.5 Concentration of Brønsted acid sites (B) and Lewis acid sites (L) in SBA-Al-EI-32-SO₃H determined with FTIR-pyridine method.

	C _B (μmol/g)	C _L (μmol/g)	Total (μmol/g)
150 °C	233	15	248
250 °C	59	5	64
350 °C	7	0	7

SBA-Al-EI-32-SO₃H, in comparison with SBA-Al-EI-32, shows higher concentration of weak, medium and strong Brønsted acid sites, indicating the effectiveness of the grafting approach. Therefore, the new material was tested in the glucose hydrolysis reaction. The same reaction conditions have been used as before to evidence how the kind of acidity influences the kinetic. Comparative study is reported in Figure 6.13. Section a) shows glucose conversion and section b) reports LA and 5-HMF yields for both catalysts.

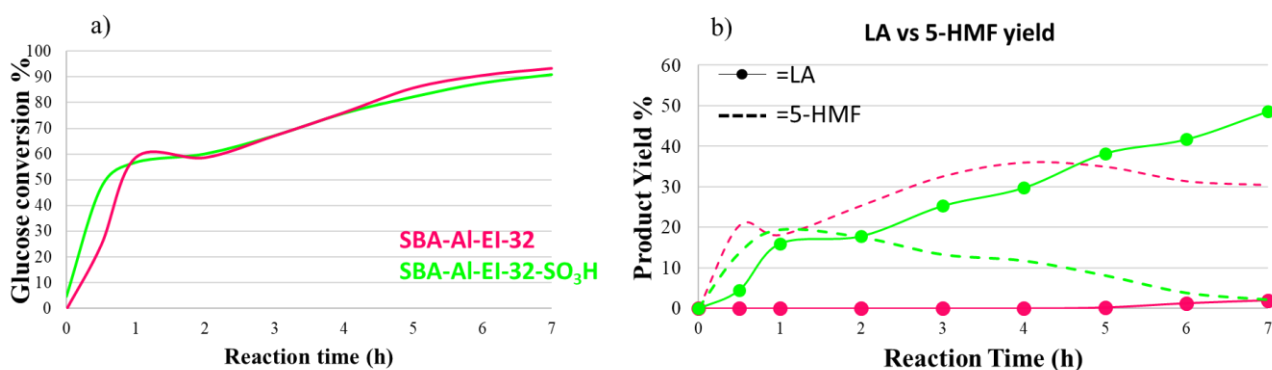


Figure 6.13 Glucose conversion (section a) and products yield (section b) for SBA-Al-EI-32 and SBA-Al-EI-32-SO₃H catalysts.

As it can be seen in section a) of Figure 6.13, there are no substantial differences between the conversion of two samples. According to the section b), the real difference can be seen in the products yield. Indeed, despite the non-grafted sample produces insignificant quantity of LA, the introduction of sulfonic acid groups implements the amount of Brønsted acid sites, leading to an increase in LA yield from 2% to 50 % during seven hours of reaction.

6.3 Conclusions

Formulation of an acid heterogeneous catalyst based on SBA-15 was successfully performed for the conversion of glucose to LA. Implementation of surface SBA-15 acidity was studied with the introduction of aluminium and sulfonic groups. In particular, aluminium was introduced in SBA-15 via two different synthetic approaches: direct synthesis during the preparation of SBA-15 mesoporous material and evaporation-impregnation method. The request silica/alumina ratio was obtained only with the evaporation-impregnation method. Direct synthesis turned out not to be a reliable method for silica and alumina interactions. After the identification of the best method for alumina introduction, materials with different Si/Al ratios were prepared: 20, 25 and 30, respectively. The effect of Si/Al ratio on the acidity and morphological features of the materials was evaluated using XRD, N₂-physisorption, pyridine FT-IR and ²⁷Al-NMR. Moreover, catalytic tests in the glucose hydrolysis at 180 °C were performed. The best catalytic results in terms of glucose conversion has been obtained with the SBA-15 with Si/Al ratio of 25 since stronger Lewis acid sites are present in this sample. Indeed, as stated by ²⁷Al-NMR, the lowest number of Al sites could guarantee the strongest nature of the acid sites. Nevertheless, the low concentration of Brønsted acid sites in the sample does not allow to produce an adequate LA yield. Hence, implementation of Brønsted acidity was carried out via the post-synthesis grafting method. With the introduction of sulfonic acid groups, the final catalyst allows to obtain 90 % of glucose conversion and 50 % of LA yield. Finally, this new material has promising properties to be used in converting more complex carbohydrate structures. Indeed, catalytic results are comparable to better known catalysts such as zeolites or ion-exchange resins.

Chapter 7. Conclusions

In this research thesis, the development of new heterogenous catalysts for biomass valorisation was performed. Two main topics had been addressed to produce, starting from biomass, one fuel and one chemical, respectively. Thanks to their promising properties, H₂ and LA were selected. As mention before, the common denominator of this thesis is the study and the optimization of most suitable catalyst for each process. In the blue boxes in Figure 7.1 are reported the main features of each catalyst. The ideal catalyst for H₂ production must be robust and resistant to coke deposition, while the best catalyst for LA production must be sufficiently acid to direct the conversion of glucose to the main product and suppress the unwanted reactions. The main findings of this work are represented in the following Figure.

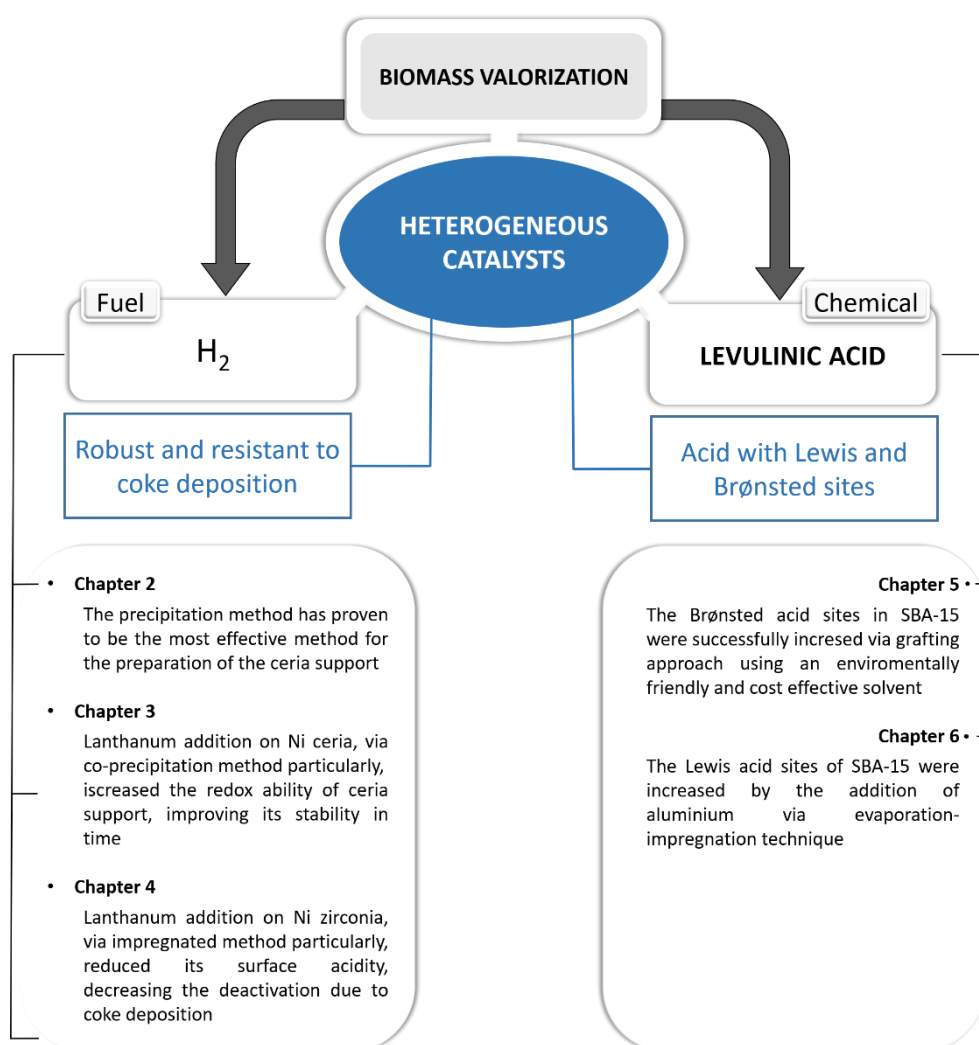


Figure 7. 1 Schematic representation of the main results of this work

Considering H₂ production, it was demonstrated how support synthesis strongly influences the catalyst features and consequently, the catalytic activity. For ceria support, it was determined how the precipitation method allows obtaining a good catalyst with high surface area, high degree of crystallinity and with a wide distribution of active phase. Moreover, these properties were successfully implemented introducing a promoter as lanthanum. It was found that lanthanum increases the redox ability of the Ni-ceria catalyst, guaranteeing higher stability in ESR conditions. Moreover, these properties were widely enhanced when the lanthanum was added by co-precipitation. The effect of lanthanum was also investigated in nickel zirconia-based catalyst. In this case, its influence is completely different from the ceria case. Indeed, for zirconia, lanthanum properly modulates the acidic/basic features. Moreover, in this case, the best result was obtained with the catalyst prepared via impregnation of the promoter on the support. Thanks to this study, it was possible to enormously implement the properties of the individual support, tuning its preparation method and introducing a promoter.

Considering the second part of the work, for LA production via hydrolysis, implementation of SBA-15 acidity was achieved with the introduction of aluminium and sulfonic groups. It was found a new environmentally friendly and cost-effective method to graft sulfonic acid groups over silica surface and increase its Brønsted acidity. To implement the Lewis one, it was demonstrated that the addition of alumina via evaporation-impregnation increases the number of medium and strong Lewis sites preserving the SBA-15 morphological features. Therefore, this new material has promising properties to be used in converting more complex carbohydrate substrates.

Thanks to this work, it was possible to understand how a deep knowledge of the processes allows to identify the weaknesses of the catalyst and to overcome it for the formulation of the ideal catalytic system. As reported, it was evident how the catalytic properties of a material can be strongly implemented by the modification of the synthetic approach and by the addition of the most appropriate promoter.

Chapter 8. References

- [1] Energy Technology Transitions for Industry, 2009. <https://doi.org/10.1787/9789264068612-en>.
- [2] BP Energy Outlook, BP Energy Outlook 2019 edition The Energy Outlook explores the forces shaping the global energy transition out to 2040 and the key uncertainties surrounding that, BP Energy Outlook 2019. (2019). <https://www.bp.com/content/dam/bp/business-sites/en/global/corporate/pdfs/energy-economics/energy-outlook/bp-energy-outlook-2019.pdf>.
- [3] D. Neves, S. Gonçalves, G. Vasconcelos, M. De Almeida, D. Agosto, R. Albergaria, D.M. Bandeira, Energy use and emissions scenarios for transport to gauge progress toward national commitments, *Energy Policy*. 135 (2019) 110997. <https://doi.org/10.1016/j.enpol.2019.110997>.
- [4] H. Machrafi, *Green Energy and Technology*, 2012. <https://doi.org/10.2174/97816080528511120101>.
- [5] J. Rogelj, J. Nabel, C. Chen, W. Hare, K. Markmann, M. Meinshausen, M. Schaeffer, K. MacEy, N. Höhne, Copenhagen Accord pledges are paltry, *Nature*. 464 (2010) 1126–1128. <https://doi.org/10.1038/4641126a>.
- [6] R. Falkner, The Paris agreement and the new logic of international climate politics, *Int. Aff.* 92 (2016) 1107–1125. <https://doi.org/10.1111/1468-2346.12708>.
- [7] H2020, Horizon 2020 Work Programme 2018 - 2020, H2020. (2019).
- [8] M. Pauly, K. Keegstra, Cell-wall carbohydrates and their modification as a resource for biofuels, *Plant J.* 54 (2008) 559–568. <https://doi.org/10.1111/j.1365-313X.2008.03463.x>.
- [9] S. V. Vassilev, D. Baxter, L.K. Andersen, C.G. Vassileva, An overview of the chemical composition of biomass, *Fuel*. 89 (2010) 913–933. <https://doi.org/10.1016/j.fuel.2009.10.022>.
- [10] P. O'Connor, A General Introduction to Biomass Utilization Possibilities, in: *Role Catal. Sustain. Prod. Bio-Fuels Bio-Chemicals*, © 2013 Elsevier B.V. All rights reserved., 2013: pp. 1–25. <https://doi.org/10.1016/B978-0-444-56330-9.00001-2>.
- [11] N. Mirabella, V. Castellani, S. Sala, Current options for the valorization of food manufacturing waste: A review, *J. Clean. Prod.* 65 (2014) 28–41. <https://doi.org/10.1016/j.jclepro.2013.10.051>.
- [12] R.A. Van Santen, Catalysis for Renewables, in: *Catal. Renewables*, 2007. <https://doi.org/10.1002/9783527621118>.
- [13] P. McKendry, Energy production from biomass (part 1): Overview of biomass, *Bioresour. Technol.* 83 (2002) 37–46. [https://doi.org/10.1016/S0960-8524\(01\)00118-3](https://doi.org/10.1016/S0960-8524(01)00118-3).
- [14] H. Chen, H. Chen, Chemical Composition and Structure of Natural Lignocellulose, in: *Biotechnol.*

Lignocellul., 2014. https://doi.org/10.1007/978-94-007-6898-7_2.

- [15] Y. Zhao, K. Lu, H. Xu, Y. Qu, L. Zhu, S. Wang, Comparative Study on the Dehydration of Biomass-Derived Disaccharides and Polysaccharides to 5 - Hydroxymethylfurfural, (2019). <https://doi.org/10.1021/acs.energyfuels.9b02863>.
- [16] EIA Hydrogen, Global Trends and Outlook for Hydrogen, Prep. by Mary-Rose Valladares. (2017). <https://doi.org/ISBN-13: 978-1-945951-07-7>.
- [17] J. Wang, H. Chen, Y. Tian, M. Yao, Y. Li, Thermodynamic analysis of hydrogen production for fuel cells from oxidative steam reforming of methanol, *Fuel*. 97 (2012) 805–811. <https://doi.org/10.1016/j.fuel.2012.03.008>.
- [18] M. Ball, M. Weeda, The hydrogen economy - Vision or reality?, *Int. J. Hydrogen Energy*. 40 (2015) 7903–7919. <https://doi.org/10.1016/j.ijhydene.2015.04.032>.
- [19] Z. Liu, S.D. Senanayake, J.A. Rodriguez, Catalysts for the Steam Reforming of Ethanol and Other Alcohols, in: *Ethanol*, 2018: pp. 133–158. <https://doi.org/10.1016/b978-0-12-811458-2.00005-5>.
- [20] R.M. Navarro, M.A. Peña, J.L.G. Fierro, Hydrogen production reactions from carbon feedstocks: Fossil fuels and biomass, *Chem. Rev.* 107 (2007) 3952–3991. <https://doi.org/10.1021/cr0501994>.
- [21] J.O. Abe, A.P.I. Popoola, E. Ajenifuja, O.M. Popoola, Hydrogen energy, economy and storage: Review and recommendation, *Int. J. Hydrogen Energy*. 44 (2019) 15072–15086. <https://doi.org/10.1016/j.ijhydene.2019.04.068>.
- [22] F. Gallucci, A. Basile, S. Tosti, A. Iulianelli, E. Drioli, Methanol and ethanol steam reforming in membrane reactors: An experimental study, *Int. J. Hydrogen Energy*. (2007). <https://doi.org/10.1016/j.ijhydene.2006.11.019>.
- [23] M. Martinelli, C.D. Watson, G. Jacobs, Sodium doping of Pt/m-ZrO₂ promotes C–C scission and decarboxylation during ethanol steam reforming, *Int. J. Hydrogen Energy*. (2019) 1–12. <https://doi.org/10.1016/j.ijhydene.2019.08.111>.
- [24] E.Y. Mironova, A.A. Lytkina, M.M. Ermilova, M.N. Efimov, L.M. Zemtsov, N. V. Orekhova, G.P. Karpacheva, G.N. Bondarenko, D.N. Muraviev, A.B. Yaroslavtsev, Ethanol and methanol steam reforming on transition metal catalysts supported on detonation synthesis nanodiamonds for hydrogen production, *Int. J. Hydrogen Energy*. 40 (2015) 3557–3565. <https://doi.org/10.1016/j.ijhydene.2014.11.082>.
- [25] W. Xu, Z. Liu, A.C. Johnston-Peck, S.D. Senanayake, G. Zhou, D. Stacchiola, E.A. Stach, J.A. Rodriguez, Steam reforming of ethanol on Ni/CeO₂: Reaction pathway and interaction between Ni and the CeO₂ support, *ACS Catal.* 3 (2013) 975–984. <https://doi.org/10.1021/cs4000969>.

- [26] 2000 高血圧症下巻 ★Jカーブ現象, (n.d.).
- [27] B. Nematollahi, M. Rezaei, M. Khajenoori, Combined dry reforming and partial oxidation of methane to synthesis gas on noble metal catalysts, *Int. J. Hydrogen Energy*. 36 (2011) 2969–2978. <https://doi.org/10.1016/j.ijhydene.2010.12.007>.
- [28] I. Rossetti, J. Lasso, V. Nichele, M. Signoretto, E. Finocchio, G. Ramis, A. Di Michele, Silica and zirconia supported catalysts for the low-temperature ethanol steam reforming, *Appl. Catal. B Environ.* 150–151 (2014) 257–267. <https://doi.org/10.1016/j.apcatb.2013.12.012>.
- [29] Y. Han, Y. Quan, P. Hao, J. Zhao, J. Ren, Highly anti-sintering and anti-coking ordered mesoporous silica carbide supported nickel catalyst for high temperature CO methanation, *Fuel*. 257 (2019) 116006. <https://doi.org/10.1016/j.fuel.2019.116006>.
- [30] I. Rossetti, A. Gallo, V. DalSanto, C.L. Bianchi, V. Nichele, M. Signoretto, E. Finocchio, G. Ramis, A. Di Michele, Nickel Catalysts Supported Over TiO₂, SiO₂ and ZrO₂ for the Steam Reforming of Glycerol, *ChemCatChem*. 5 (2013) 294–306. <https://doi.org/10.1002/cctc.201200481>.
- [31] P. Osorio-Vargas, C.H. Campos, R.M. Navarro, J.L.G. Fierro, P. Reyes, Rh/Al₂O₃-La₂O₃ catalysts promoted with CeO₂ for ethanol steam reforming reaction, *J. Mol. Catal. A Chem.* 407 (2015) 169–181. <https://doi.org/10.1016/j.molcata.2015.06.031>.
- [32] D. Li, L. Zeng, X. Li, X. Wang, H. Ma, S. Assabumrungrat, J. Gong, Ceria-promoted Ni/SBA-15 catalysts for ethanol steam reforming with enhanced activity and resistance to deactivation, *Appl. Catal. B Environ.* 176–177 (2015) 532–541. <https://doi.org/10.1016/j.apcatb.2015.04.020>.
- [33] J.H. Song, S.J. Han, J. Yoo, S. Park, D.H. Kim, I.K. Song, Hydrogen production by steam reforming of ethanol over Ni-X/Al₂O₃-ZrO₂ (X = Mg, Ca, Sr, and Ba) xerogel catalysts: Effect of alkaline earth metal addition, *J. Mol. Catal. A Chem.* 415 (2016) 151–159. <https://doi.org/10.1016/j.molcata.2016.02.010>.
- [34] S.J. Han, Y. Bang, J.H. Song, J. Yoo, S. Park, K.H. Kang, I.K. Song, Hydrogen production by steam reforming of ethanol over dual-templated Ni-Al₂O₃ catalyst, *Catal. Today*. 265 (2016) 103–110. <https://doi.org/10.1016/j.cattod.2015.07.041>.
- [35] T. Kecské, Hydrogen formation in ethanol reforming on supported noble metal catalysts, 116 (2006) 367–376. <https://doi.org/10.1016/j.cattod.2006.05.073>.
- [36] S. Curtin, J. Gangi, IEA, E.K. Tan, N. Materials, T. Flexcell, G.G. Tao, A. V Virkar, D. of the N.E. and I.T.D.O. (NEDO), 4thenergywave, I.E. Event, IEA, A. Iyengar, D. Keairns, K. Krulla, D. Newby, H. Kawamoto, Y. Kobayashi, Y. Ando, T. Kabata, M. Nishimura, K. Tomida, N. Mataka, N.Q. Mitali, M.B. Mogensen, C. Roadmap, W.G. Street, W. Lee, National Aeronautics and Space Administration,

- S. Sui, H. Tu, Q. Yu, Development of Fuel Cell and Hydrogen 2009-2010, Technol. Roadmap. 22 (2014) 55–62. <https://doi.org/10.1039/b105764m>.
- [37] M. Capdevila-Cortada, G. Vilé, D. Teschner, J. Pérez-Ramírez, N. López, Reactivity descriptors for ceria in catalysis, *Appl. Catal. B Environ.* 197 (2016) 299–312. <https://doi.org/10.1016/j.apcatb.2016.02.035>.
- [38] T.R. Reina, S. Ivanova, V. Idakiev, T. Tabakova, M.A. Centeno, Q.F. Deng, Z.Y. Yuan, J.A. Odriozola, Nanogold mesoporous iron promoted ceria catalysts for total and preferential CO oxidation reactions, *J. Mol. Catal. A Chem.* 414 (2016) 62–71. <https://doi.org/10.1016/j.molcata.2016.01.003>.
- [39] D.R. Mullins, The surface chemistry of cerium oxide, *Surf. Sci. Rep.* 70 (2015) 42–85. <https://doi.org/10.1016/j.surfrep.2014.12.001>.
- [40] T. Montini, M. Melchionna, M. Monai, P. Fornasiero, Fundamentals and Catalytic Applications of CeO₂ - Based Materials, (2016). <https://doi.org/10.1021/acs.chemrev.5b00603>.
- [41] O.H. Laguna, M.A. Centeno, M. Boutonnet, J.A. Odriozola, Au-supported on Fe-doped ceria solids prepared in water-in-oil microemulsions: Catalysts for CO oxidation, *Catal. Today.* (2016). <https://doi.org/10.1016/j.cattod.2016.05.059>.
- [42] J.S. Elias, M. Risch, L. Giordano, A.N. Mansour, Y. Shao-Horn, Structure, bonding, and catalytic activity of monodisperse, transition-metal-substituted CeO₂ nanoparticles, *J. Am. Chem. Soc.* 136 (2014) 17193–17200. <https://doi.org/10.1021/ja509214d>.
- [43] S. Eriksson, U. Nylén, S. Rojas, M. Boutonnet, Preparation of catalysts from microemulsions and their applications in heterogeneous catalysis, *Appl. Catal. A Gen.* 265 (2004) 207–219. <https://doi.org/10.1016/j.apcata.2004.01.014>.
- [44] O.H. Laguna, M.A. Centeno, M. Boutonnet, J.A. Odriozola, Au-supported on Fe-doped ceria solids prepared in water-in-oil microemulsions: Catalysts for CO oxidation, *Catal. Today.* 278 (2016) 140–149. <https://doi.org/10.1016/j.cattod.2016.05.059>.
- [45] T. Andana, M. Piumetti, S. Bensaid, L. Veyre, C. Thieuleux, N. Russo, D. Fino, E.A. Quadrelli, R. Pirone, Ceria-supported small Pt and Pt₃Sn nanoparticles for NO_x-assisted soot oxidation, *Appl. Catal. B Environ.* 209 (2017) 295–310. <https://doi.org/10.1016/j.apcatb.2017.03.010>.
- [46] J. Cao, Y. Wang, T. Zhang, S. Wu, Z. Yuan, Preparation, characterization and catalytic behavior of nanostructured, 78 (2008) 120–128. <https://doi.org/10.1016/j.apcatb.2007.09.007>.
- [47] N.D. Charisiou, K.N. Papageridis, G. Siakavelas, V. Sebastian, S.J. Hinder, M.A. Baker, K. Polychronopoulou, M.A. Goula, The influence of SiO₂ doping on the Ni/ZrO₂ supported catalyst for hydrogen production through the glycerol steam reforming reaction, *Catal. Today.* 319 (2019) 206–219. <https://doi.org/10.1016/j.cattod.2018.04.052>.

- [48] K.T. Jung, A.T. Bell, The effects of synthesis and pretreatment conditions on the bulk structure and surface properties of zirconia, *J. Mol. Catal. A Chem.* 163 (2000) 27–42. [https://doi.org/10.1016/S1381-1169\(00\)00397-6](https://doi.org/10.1016/S1381-1169(00)00397-6).
- [49] M. Hye, J. Gil, H. Lee, Y. Bang, J. Suk, I. Kyu, Applied Catalysis B: Environmental Hydrogen production by auto-thermal reforming of ethanol over nickel catalysts supported on metal oxides: Effect of support acidity, *Applied Catal. B, Environ.* 98 (2010) 57–64. <https://doi.org/10.1016/j.apcatb.2010.05.002>.
- [50] M.H. Youn, J.G. Seo, H. Lee, Y. Bang, J.S. Chung, I.K. Song, Hydrogen production by auto-thermal reforming of ethanol over nickel catalysts supported on metal oxides: Effect of support acidity, *Appl. Catal. B Environ.* 98 (2010) 57–64. <https://doi.org/10.1016/j.apcatb.2010.05.002>.
- [51] W. Li, Z. Zhao, Y. Jiao, ScienceDirect Dry reforming of methane towards CO-rich hydrogen production over robust supported Ni catalyst on hierarchically structured monoclinic zirconia nanosheets, *Int. J. Hydrogen Energy.* 41 (2016) 17907–17921. <https://doi.org/10.1016/j.ijhydene.2016.07.272>.
- [52] W. Li, Z. Zhao, Y. Jiao, Dry reforming of methane towards CO-rich hydrogen production over robust supported Ni catalyst on hierarchically structured monoclinic zirconia nanosheets, *Int. J. Hydrogen Energy.* 41 (2016) 17907–17921. <https://doi.org/10.1016/j.ijhydene.2016.07.272>.
- [53] A. Ochoa, B. Aramburu, M. Ibáñez, B. Valle, J. Bilbao, A.G. Gayubo, P. Castaño, Compositional Insights and Valorization Pathways for Carbonaceous Material Deposited During Bio-Oil Thermal Treatment, *ChemSusChem.* 7 (2014) 2597–2608. <https://doi.org/10.1002/cssc.201402276>.
- [54] V. Nichele, M. Signoreto, F. Pinna, F. Menegazzo, I. Rossetti, G. Cruciani, G. Cerrato, A. Di Michele, Ni/ZrO₂ catalysts in ethanol steam reforming: Inhibition of coke formation by CaO-doping, *Appl. Catal. B Environ.* 150–151 (2014) 12–20. <https://doi.org/10.1016/j.apcatb.2013.11.037>.
- [55] C.H. Campos, P. Osorio-Vargas, N. Flores-González, J.L.G. Fierro, P. Reyes, Effect of Ni Loading on Lanthanide (La and Ce) Promoted γ -Al₂O₃ Catalysts Applied to Ethanol Steam Reforming, *Catal. Letters.* 146 (2016) 433–441. <https://doi.org/10.1007/s10562-015-1649-6>.
- [56] P. Osorio-Vargas, C.H. Campos, R.M. Navarro, J.L.G. Fierro, P. Reyes, Improved ethanol steam reforming on Rh/Al₂O₃ catalysts doped with CeO₂ or/and La₂O₃: Influence in reaction pathways including coke formation, *Appl. Catal. A Gen.* 505 (2015) 159–172. <https://doi.org/10.1016/j.apcata.2015.07.037>.
- [57] M. Dan, M. Mihet, Z. Tasnadi-Asztalos, A. Imre-Lucaci, G. Katona, M.D. Lazar, Hydrogen production by ethanol steam reforming on nickel catalysts: Effect of support modification by CeO₂ and La₂O₃, *Fuel.* 147 (2015) 260–268. <https://doi.org/10.1016/j.fuel.2015.01.050>.
- [58] J. Bussi, M. Musso, S. Veiga, N. Bepalko, R. Faccio, A.C. Roger, Ethanol steam reforming over

- NiLaZr and NiCuLaZr mixed metal oxide catalysts, *Catal. Today*. 213 (2013) 42–49. <https://doi.org/10.1016/j.cattod.2013.04.013>.
- [59] D. Carnevali, M.G. Rigamonti, T. Tabanelli, G.S. Patience, F. Cavani, Levulinic acid upgrade to succinic acid with hydrogen peroxide, *Appl. Catal. A Gen.* 563 (2018) 98–104. <https://doi.org/10.1016/j.apcata.2018.06.034>.
- [60] G. Morales, J.A. Melero, J. Iglesias, M. Paniagua, C. López-Aguado, From levulinic acid biorefineries to γ -valerolactone (GVL) using a bi-functional Zr-Al-Beta catalyst, *React. Chem. Eng.* 4 (2019) 1834–1843. <https://doi.org/10.1039/c9re00117d>.
- [61] Z. Yu, X. Lu, J. Xiong, N. Ji, Transformation of Levulinic Acid to Valeric Biofuels: A Review on Heterogeneous Bifunctional Catalytic Systems, *ChemSusChem*. 12 (2019) 3915–3930. <https://doi.org/10.1002/cssc.201901522>.
- [62] Z. Yi, D. Hu, H. Xu, Z. Wu, M. Zhang, K. Yan, Metal regulating the highly selective synthesis of gamma-valerolactone and valeric biofuels from biomass-derived levulinic acid, *Fuel*. 259 (2020) 116208. <https://doi.org/10.1016/j.fuel.2019.116208>.
- [63] V. Russo, V. Hrobar, P. Mäki-Arvela, K. Eränen, F. Sandelin, M. Di Serio, T. Salmi, Kinetics and Modelling of Levulinic Acid Esterification in Batch and Continuous Reactors, *Top. Catal.* 61 (2018) 1856–1865. <https://doi.org/10.1007/s11244-018-0998-y>.
- [64] G. Novodárszki, J. Valyon, Á. Illés, S. Dóbbé, D. Deka, J. Hancsók, M.R. Mihályi, Heterogeneous hydroconversion of levulinic acid over silica-supported Ni catalyst, *React. Kinet. Mech. Catal.* 126 (2019) 795–810. <https://doi.org/10.1007/s11144-018-1507-9>.
- [65] S.S. Chen, T. Maneerung, D.C.W. Tsang, Y.S. Ok, C.H. Wang, Valorization of biomass to hydroxymethylfurfural, levulinic acid, and fatty acid methyl ester by heterogeneous catalysts, *Chem. Eng. J.* 328 (2017) 246–273. <https://doi.org/10.1016/j.cej.2017.07.020>.
- [66] F.D. Pileidis, M.M. Titirici, Levulinic Acid Biorefineries: New Challenges for Efficient Utilization of Biomass, *ChemSusChem*. 9 (2016) 562–582. <https://doi.org/10.1002/cssc.201501405>.
- [67] T. Werpy, G. Petersen, Top Value Added Chemicals from Biomass: Volume I -- Results of Screening for Potential Candidates from Sugars and Synthesis Gas. Office of Scientific and Technical Information (OSTI), Off. Sci. Tech. Inf. (2004) 69. <https://doi.org/10.2172/15008859>.
- [68] K.C. Badgular, V.C. Badgular, B.M. Bhanage, A review on catalytic synthesis of energy rich fuel additive levulinate compounds from biomass derived levulinic acid, *Fuel Process. Technol.* 197 (2020) 106213. <https://doi.org/10.1016/j.fuproc.2019.106213>.
- [69] A.M.R. Galletti, C. Antonetti, V. De Luise, D. Licursi, N.N.O. Di Nasso, Levulinic acid production from waste biomass, *BioResources*. 7 (2012) 1824–1834.

- [70] A. Morone, M. Apte, R.A. Pandey, Levulinic acid production from renewable waste resources: Bottlenecks, potential remedies, advancements and applications, *Renew. Sustain. Energy Rev.* 51 (2015) 548–565. <https://doi.org/10.1016/j.rser.2015.06.032>.
- [71] L. Yan, N. Yang, H. Pang, B. Liao, Production of levulinic acid from bagasse and paddy straw by liquefaction in the presence of hydrochloride acid, *Clean - Soil, Air, Water.* 36 (2008) 158–163. <https://doi.org/10.1002/clen.200700100>.
- [72] Q. Fang, M.A. Hanna, Experimental studies for levulinic acid production from whole kernel grain sorghum, *Bioresour. Technol.* 81 (2002) 187–192. [https://doi.org/10.1016/S0960-8524\(01\)00144-4](https://doi.org/10.1016/S0960-8524(01)00144-4).
- [73] M. Signoretto, S. Taghavi, E. Ghedini, F. Menegazzo, Catalytic Production of Levulinic Acid (LA) from Actual Biomass, *Molecules.* (2019). <https://doi.org/10.3390/molecules24152760>.
- [74] L.T. Mika, E. Cséfalvay, Á. Németh, Catalytic Conversion of Carbohydrates to Initial Platform Chemicals: Chemistry and Sustainability, *Chem. Rev.* 118 (2018) 505–613. <https://doi.org/10.1021/acs.chemrev.7b00395>.
- [75] S. Kang, J. Yu, An intensified reaction technology for high levulinic acid concentration from lignocellulosic biomass, *Biomass and Bioenergy.* 95 (2016) 214–220. <https://doi.org/10.1016/j.biombioe.2016.10.009>.
- [76] R. Weingarten, Y.T. Kim, G.A. Tompsett, A. Fernández, K.S. Han, E.W. Hagaman, W.C. Conner, J.A. Dumesic, G.W. Huber, Conversion of glucose into levulinic acid with solid metal(IV) phosphate catalysts, *J. Catal.* 304 (2013) 123–134. <https://doi.org/10.1016/j.jcat.2013.03.023>.
- [77] X. Zhang, K. Wilson, A.F. Lee, Heterogeneously Catalyzed Hydrothermal Processing of C5-C6 Sugars, *Chem. Rev.* 116 (2016) 12328–12368. <https://doi.org/10.1021/acs.chemrev.6b00311>.
- [78] R. Weingarten, J. Cho, R. Xing, W.C. Conner, G.W. Huber, Kinetics and reaction engineering of levulinic acid production from aqueous glucose solutions, *ChemSusChem.* 5 (2012) 1280–1290. <https://doi.org/10.1002/cssc.201100717>.
- [79] R.M. Abdilla-Santes, W. Guo, P.C.A. Bruijninx, J. Yue, P.J. Deuss, H.J. Heeres, High-Yield 5-Hydroxymethylfurfural Synthesis from Crude Sugar Beet Juice in a Biphasic Microreactor, *ChemSusChem.* 12 (2019) 4304–4312. <https://doi.org/10.1002/cssc.201901115>.
- [80] K. Kohli, R. Prajapati, B.K. Sharma, Bio-based chemicals from renewable biomass for integrated biorefineries, *Energies.* 12 (2019). <https://doi.org/10.3390/en12020233>.
- [81] L. Cao, I.K.M. Yu, D.W. Cho, D. Wang, D.C.W. Tsang, S. Zhang, S. Ding, L. Wang, Y.S. Ok, Microwave-assisted low-temperature hydrothermal treatment of red seaweed (*Gracilaria lemaneiformis*) for production of levulinic acid and algae hydrochar, *Bioresour. Technol.* 273 (2019) 251–258. <https://doi.org/10.1016/j.biortech.2018.11.013>.

- [82] D.J. Hayes, S. Fitzpatrick, M.H.B. Hayes, J.R.H. Ross, The Biofine Process - Production of Levulinic acid, Furfural, and Formic Acid from lignocellulosic feedstocks in biorefineries - Industrial processes and products\n\nDaniel J. Hayes, Steve Fitzpatrick, Michael H. B. Hayes, and Julian R.H. Ross, *Ind. Process. Prod. - Status Quo Futur. Dir.* 1 (2006).
- [83] S.W. Fitzpatrick, The biofine technology: A “bio-refinery” concept based on thermochemical conversion of cellulosic biomass, *ACS Symp. Ser.* 921 (2006) 271–287. <https://doi.org/10.1021/bk-2006-0921.ch020>.
- [84] J.J. Bozell, L. Moens, D.C. Elliott, Y. Wang, G.G. Neuenschwander, S.W. Fitzpatrick, R.J. Bilski, J.L. Jarnefeld, Production of levulinic acid and use as a platform chemical for derived products, *Resour. Conserv. Recycl.* 28 (2000) 227–239. [https://doi.org/10.1016/S0921-3449\(99\)00047-6](https://doi.org/10.1016/S0921-3449(99)00047-6).
- [85] B. Agarwal, K. Kailasam, R.S. Sangwan, S. Elumalai, Traversing the history of solid catalysts for heterogeneous synthesis of 5-hydroxymethylfurfural from carbohydrate sugars: A review, *Renew. Sustain. Energy Rev.* 82 (2018) 2408–2425. <https://doi.org/10.1016/j.rser.2017.08.088>.
- [86] I. Thapa, B. Mullen, A. Saleem, C. Leibig, R.T. Baker, J.B. Giorgi, Efficient green catalysis for the conversion of fructose to levulinic acid, *Appl. Catal. A Gen.* 539 (2017) 70–79. <https://doi.org/10.1016/j.apcata.2017.03.016>.
- [87] A. Osatiashtiani, K. Wilson, A.F. Lee, D.R. Brown, J.A. Melero, G. Morales, Bifunctional SO_4/ZrO_2 catalysts for 5-hydroxymethylfufural (5-HMF) production from glucose, *Catal. Sci. Technol.* 4 (2014) 333–342. <https://doi.org/10.1039/C3CY00409K>.
- [88] C. Tempelman, U. Jacobs, T. Hut, E.P. de Pina, M. van Munster, N. Cherkasov, V. Degirmenci, Sn exchanged acidic ion exchange resin for the stable and continuous production of 5-HMF from glucose at low temperature, *Appl. Catal. A Gen.* 588 (2019) 112061. <https://doi.org/10.1016/j.jphotochem.2019.112061>.
- [89] D.M. Lai, L. Deng, Q.X. Guo, Y. Fu, Hydrolysis of biomass by magnetic solid acid, *Energy Environ. Sci.* 4 (2011) 3552–3557. <https://doi.org/10.1039/c1ee01526e>.
- [90] W. Wei, H. Yang, S. Wu, Efficient conversion of carbohydrates into levulinic acid over chromium modified niobium phosphate catalyst, *Fuel.* 256 (2019) 115940. <https://doi.org/10.1016/j.fuel.2019.115940>.
- [91] S. Kang, J. Yu, Maintenance of a Highly Active Solid Acid Catalyst in Sugar Beet Molasses for Levulinic Acid Production, *Sugar Tech.* 20 (2018) 182–193. <https://doi.org/10.1007/s12355-017-0543-5>.
- [92] V. Trombettoni, D. Lanari, P. Prinsen, R. Luque, A. Marrocchi, L. Vaccaro, Recent advances in sulfonated resin catalysts for efficient biodiesel and bio-derived additives production, *Prog. Energy*

Combust. Sci. 65 (2018) 136–162. <https://doi.org/10.1016/j.pecs.2017.11.001>.

- [93] J.B. Higgins, G.T. Kerr, A.C. Rohrman, J.L. Schlenker, J.D. Wood, W.J. Rohrbaugh, R.B. LaPierre, The framework topology of zeolite beta, *Zeolites*. 8 (2005) 446–452. [https://doi.org/10.1016/s0144-2449\(88\)80219-7](https://doi.org/10.1016/s0144-2449(88)80219-7).
- [94] D. Zhai, Y. Liu, H. Zheng, L. Zhao, J. Gao, C. Xu, B. Shen, A first-principles evaluation of the stability, accessibility, and strength of Brønsted acid sites in zeolites, *J. Catal.* 352 (2017) 627–637. <https://doi.org/10.1016/j.jcat.2017.06.035>.
- [95] J. Čejka, A. Corma, S. Zones, *Zeolites and Catalysis: Synthesis, Reactions and Applications*, 2010. <https://doi.org/10.1002/9783527630295>.
- [96] N.A.S. Ramli, N.A.S. Amin, Kinetic study of glucose conversion to levulinic acid over Fe/HY zeolite catalyst, *Chem. Eng. J.* 283 (2016) 150–159. <https://doi.org/10.1016/j.cej.2015.07.044>.
- [97] N.A.S. Ramli, N.A.S. Amin, Fe/HY zeolite as an effective catalyst for levulinic acid production from glucose: Characterization and catalytic performance, *Appl. Catal. B Environ.* 163 (2015) 487–498. <https://doi.org/10.1016/j.apcatb.2014.08.031>.
- [98] M. Xia, W. Dong, M. Gu, C. Chang, Z. Shen, Y. Zhang, Synergetic effects of bimetals in modified beta zeolite for lactic acid synthesis from biomass-derived carbohydrates, *RSC Adv.* 8 (2018) 8965–8975. <https://doi.org/10.1039/c7ra12533j>.
- [99] J. Jae, G.A. Tompsett, A.J. Foster, K.D. Hammond, S.M. Auerbach, R.F. Lobo, G.W. Huber, Investigation into the shape selectivity of zeolite catalysts for biomass conversion, *J. Catal.* 279 (2011) 257–268. <https://doi.org/10.1016/j.jcat.2011.01.019>.
- [100] K. Nakajima, Y. Baba, R. Noma, M. Kitano, J. N. Kondo, S. Hayashi, M. Hara, Nb₂O₅·nH₂O as a heterogeneous catalyst with water-tolerant lewis acid sites, *J. Am. Chem. Soc.* 133 (2011) 4224–4227. <https://doi.org/10.1021/ja110482r>.
- [101] M. Choi, W. Heo, F. Kleitz, R. Ryoo, Facile synthesis of high quality mesoporous SBA-15 with enhanced control of the porous network connectivity and wall thickness Electronic supplementary information (ESI) available: structural parameters (Table 1) and N₂ adsorption/desorption isotherms at 7, *Chem. Commun.* 75 (2003) 1340. <https://doi.org/10.1039/b303696k>.
- [102] D. Margolese, J.A. Melero, S.C. Christiansen, B.F. Chmelka, G.D. Stucky, Direct syntheses of ordered SBA-15 mesoporous silica containing sulfonic acid groups, *Chem. Mater.* 12 (2000) 2448–2459. <https://doi.org/10.1021/cm0010304>.
- [103] P. Zhang, H. Wu, M. Fan, W. Sun, P. Jiang, Y. Dong, Direct and postsynthesis of tin-incorporated SBA-15 functionalized with sulfonic acid for efficient biodiesel production, *Fuel*. 235 (2019) 426–432. <https://doi.org/10.1016/j.fuel.2018.08.029>.

- [104] F. Su, Y. Guo, Advancements in solid acid catalysts for biodiesel production, *Green Chem.* 16 (2014) 2934–2957. <https://doi.org/10.1039/c3gc42333f>.
- [105] J. Dhainaut, J.P. Dacquin, A.F. Lee, K. Wilson, Hierarchical macroporous-mesoporous SBA-15 sulfonic acid catalysts for biodiesel synthesis, *Green Chem.* 12 (2010) 296–303. <https://doi.org/10.1039/b919341c>.
- [106] Z.Y. Wu, H.J. Wang, T.T. Zhuang, L.B. Sun, Y.M. Wang, J.H. Zhu, Multiple functionalization of mesoporous silica in one-pot: Direct synthesis of aluminum-containing plugged SBA-15 from aqueous nitrate solutions, *Adv. Funct. Mater.* (2008). <https://doi.org/10.1002/adfm.200700706>.
- [107] K. Szczodrowski, B. Pr elot, S. Lantenois, J.M. Douillard, J. Zajac, Effect of heteroatom doping on surface acidity and hydrophilicity of Al, Ti, Zr-doped mesoporous SBA-15, *Microporous Mesoporous Mater.* 124 (2009) 84–93. <https://doi.org/10.1016/j.micromeso.2009.04.035>.
- [108] S. Xing, P. Lv, J. Fu, J. Wang, P. Fan, L. Yang, Z. Yuan, Direct synthesis and characterization of pore-broadened Al-SBA-15, *Microporous Mesoporous Mater.* 239 (2017) 316–327. <https://doi.org/10.1016/j.micromeso.2016.10.018>.
- [109] S. Macko, P. H. E. Emmett, Brunauer, S., Emmett, P. H. & Teller, E. Adsorption of gases in multimolecular layers. *J. Am. Chem. Soc.* 60, 309–319, 1938. <https://doi.org/10.1021/ja01269a023>.
- [110] E.P. Barrett, L.G. Joyner, P.P. Halenda, The Determination of Pore Volume and Area Distributions in Porous Substances. I. Computations from Nitrogen Isotherms, *J. Am. Chem. Soc.* 73 (1951) 373–380. <https://doi.org/10.1021/ja01145a126>.
- [111] F. Pinna, Supported metal catalysts preparation, *Catal. Today.* (1998). [https://doi.org/10.1016/S0920-5861\(98\)00043-1](https://doi.org/10.1016/S0920-5861(98)00043-1).
- [112] P.B. Balbuena, K.E. Gubbins, Theoretical Interpretation of Adsorption Behavior of Simple Fluids in Slit Pores, *Langmuir.* 9 (1993) 1801–1814. <https://doi.org/10.1021/la00031a031>.
- [113] M. Manzoli, F. Menegazzo, M. Signoretto, G. Cruciani, F. Pinna, Effects of synthetic parameters on the catalytic performance of Au/CeO₂ for furfural oxidative esterification, *J. Catal.* (2015). <https://doi.org/10.1016/j.jcat.2015.07.030>.
- [114] V. Nichele, M. Signoretto, F. Menegazzo, I. Rossetti, G. Cruciani, Hydrogen production by ethanol steam reforming: Effect of the synthesis parameters on the activity of Ni/TiO₂ catalysts, *Int. J. Hydrogen Energy.* 39 (2014) 4252–4258. <https://doi.org/10.1016/j.ijhydene.2013.12.178>.
- [115] C. Pizzolitto, F. Menegazzo, E. Ghedini, G. Innocenti, A. Di Michele, G. Cruciani, F. Cavani, M. Signoretto, Increase of Ceria Redox Ability by Lanthanum Addition on Ni Based Catalysts for Hydrogen Production, *ACS Sustain. Chem. Eng.* 6 (2018) 13867–13876. <https://doi.org/10.1021/acssuschemeng.8b02103>.

- [116] N. Pinton, M. V. Vidal, M. Signoretto, A. Martínez-Arias, V. Cortés Corberán, Ethanol steam reforming on nanostructured catalysts of Ni, Co and CeO₂: Influence of synthesis method on activity, deactivation and regenerability, *Catal. Today*. 296 (2017) 135–143. <https://doi.org/10.1016/j.cattod.2017.06.022>.
- [117] A.M. Venezia, V. La Parola, L.F. Liotta, Structural and surface properties of heterogeneous catalysts : Nature of the oxide carrier and supported particle size effects, *Catal. Today*. 285 (2017) 114–124. <https://doi.org/10.1016/j.cattod.2016.11.004>.
- [118] O. Omoregbe, H.T. Danh, S.Z. Abidin, H.D. Setiabudi, B. Abdullah, Influence of Lanthanide Promoters on Ni / SBA-15 Catalysts for Syngas Production by Methane Dry Reforming, *Procedia Eng.* 148 (2016) 1388–1395. <https://doi.org/10.1016/j.proeng.2016.06.556>.
- [119] A. Ideris, E. Croiset, M. Pritzker, A. Amin, ScienceDirect Direct-methane solid oxide fuel cell (SOFC) with, *Int. J. Hydrogen Energy*. 42 (2017) 23118–23129. <https://doi.org/10.1016/j.ijhydene.2017.07.117>.
- [120] 1995 H. Idriss.pdf, (n.d.).
- [121] T. Siqueira, R. Crisostomo, R. Neto, M. Celso, L. Veiga, M. Kourtelesis, S. Ladas, X. Verykios, Applied Catalysis B : Environmental Ethanol conversion at low temperature over CeO₂ — Supported Ni-based catalysts . Effect of Pt addition to Ni catalyst, "Applied Catal. B, Environ. 181 (2016) 754–768. <https://doi.org/10.1016/j.apcatb.2015.08.044>.
- [122] F. Cavani, In Situ DRIFTS-MS Study of the Anaerobic Oxidation of Ethanol over Spinel Mixed Oxides, (2013). <https://doi.org/10.1021/jp409831t>.
- [123] W. Xu, Z. Liu, A.C. Johnston-peck, S.D. Senanayake, G. Zhou, D. Stacchiola, E.A. Stach, J.A. Rodriguez, Steam Reforming of Ethanol on Ni/CeO₂ : Reaction Pathway and Interaction between Ni and the CeO₂ Support, 2 (2013). <https://doi.org/10.1021/cs4000969>.
- [124] O. Seiferth, K. Wolter, B. Dillmann, G. Klivenyi, H. Freund, D. Scarano, A. Zecchina, IR investigations of CO adsorption on chromia surfaces : Cr O (0001) / Cr (110) versus polycrystalline a -Cr O, 421 (1999) 176–190.
- [125] G. Busca, catalysis by metal oxides : an introduction, 27 (1996) 323–352.
- [126] S. Collins, G. Finos, R. Alcántara, S. Bernal, A. Bonivardi, Applied Catalysis A : General Effect of gallia doping on the acid – base and redox properties of ceria, 388 (2010) 202–210. <https://doi.org/10.1016/j.apcata.2010.08.050>.
- [127] R. Zhang, K. Lu, L. Zong, S. Tong, X. Wang, G. Feng, Applied Surface Science Gold supported on ceria nanotubes for CO oxidation, *Appl. Surf. Sci.* 416 (2017) 183–190. <https://doi.org/10.1016/j.apsusc.2017.04.158>.

- [128] W.S. Dong, H.S. Roh, K.W. Jun, S.E. Park, Y.S. Oh, Methane reforming over Ni/Ce-ZrO₂ catalysts: Effect of nickel content, *Appl. Catal. A Gen.* 226 (2002) 63–72. [https://doi.org/10.1016/S0926-860X\(01\)00883-3](https://doi.org/10.1016/S0926-860X(01)00883-3).
- [129] J. Marrero-jerez, S. Larrondo, E. Rodríguez-castellón, P. Núñez, TPR, XRD and XPS characterisation of ceria-based materials synthesized by freeze-drying precursor method, *Ceram. Int.* 40 (2014) 6807–6814. <https://doi.org/10.1016/j.ceramint.2013.11.143>.
- [130] R. Mandapaka, G. Madras, Aluminium and rhodium co-doped ceria for water gas shift reaction and CO oxidation, *Mol. Catal.* 451 (2018) 4–12. <https://doi.org/10.1016/j.mcat.2017.10.001>.
- [131] D.E. Glass, V. Galvan, G.K.S. Prakash, *Electrochimica Acta* The Effect of Annealing Temperature on Nickel on Reduced Graphene Oxide Catalysts on Urea Electrooxidation, *Electrochim. Acta.* 253 (2017) 489–497. <https://doi.org/10.1016/j.electacta.2017.09.064>.
- [132] V.M. Gonzalez-delacruz, J.P. Holgado, R. Pereñíguez, A. Caballero, Morphology changes induced by strong metal – support interaction on a Ni – ceria catalytic system, 257 (2008) 307–314. <https://doi.org/10.1016/j.jcat.2008.05.009>.
- [133] G. Centi, S. Perathoner, Opportunities and prospects in the chemical recycling of carbon dioxide to fuels §, 148 (2009) 191–205. <https://doi.org/10.1016/j.cattod.2009.07.075>.
- [134] R. Molina, G. Poncelet, α -Alumina-supported nickel catalysts prepared from nickel acetylacetonate: A TPR study, *J. Catal.* 173 (1998) 257–267. <https://doi.org/10.1006/jcat.1997.1931>.
- [135] A.M. Diskin, R.H. Cunningham, R.M. Ormerod, The oxidative chemistry of methane over supported nickel catalysts, *Catal. Today.* 46 (1998) 147–154. [https://doi.org/10.1016/S0920-5861\(98\)00336-8](https://doi.org/10.1016/S0920-5861(98)00336-8).
- [136] V. Nichele, M. Signoretto, F. Pinna, E. Ghedini, M. Compagnoni, I. Rossetti, G. Cruciani, A. Di Michele, Bimetallic Ni-Cu Catalysts for the Low-Temperature Ethanol Steam Reforming: Importance of Metal-Support Interactions, *Catal. Letters.* 145 (2015) 549–558. <https://doi.org/10.1007/s10562-014-1414-2>.
- [137] P. Biswas, D. Kunzru, Steam reforming of ethanol for production of hydrogen over Ni/CeO₂-ZrO₂ catalyst: Effect of support and metal loading, *Int. J. Hydrogen Energy.* 32 (2007) 969–980. <https://doi.org/10.1016/j.ijhydene.2006.09.031>.
- [138] V. Santos, M. Zeni, C.P. Bergmann, J.M. Hohemberger, Correlation between thermal treatment and tetragonal/monoclinic nanostructured zirconia powder obtained by sol-gel process, *Rev. Adv. Mater. Sci.* 17 (2008) 62–70.
- [139] P.D.L. Mercera, J.G. Van Ommen, E.B.M. Doesburg, A.J. Burggraaf, J.R.H. Ross, Influence of ethanol washing of the hydrous precursor on the textural and structural properties of zirconia, *J. Mater. Sci.* 27 (1992) 4890–4898. <https://doi.org/10.1007/BF01105251>.

- [140] C. Li, M. Li, UV Raman spectroscopic study on the phase transformation of ZrO₂, Y₂O₃-ZrO₂ and SO₄²⁻/ZrO₂, *J. Raman Spectrosc.* 33 (2002) 301–308. <https://doi.org/10.1002/jrs.863>.
- [141] C. Morterra, G. Cerrato, F. Pinna, M. Signoretto, Crystal phase, spectral features, and catalytic activity of sulfate-doped zirconia systems, *J. Catal.* 157 (1995) 109–123. <https://doi.org/10.1006/jcat.1995.1272>.
- [142] I. Rossetti, C. Biffi, C.L. Bianchi, V. Nichele, M. Signoretto, F. Menegazzo, E. Finocchio, G. Ramis, A. Di Michele, Ni/SiO₂ and Ni/ZrO₂ catalysts for the steam reforming of ethanol, *Appl. Catal. B Environ.* 117–118 (2012) 384–396. <https://doi.org/10.1016/j.apcatb.2012.02.006>.
- [143] D. Wierzbicki, R. Baran, R. Dębek, M. Motak, M.E. Gálvez, T. Grzybek, P. Da Costa, P. Glatzel, Examination of the influence of La promotion on Ni state in hydrotalcite-derived catalysts under CO₂ methanation reaction conditions: Operando X-ray absorption and emission spectroscopy investigation, *Appl. Catal. B Environ.* 232 (2018) 409–419. <https://doi.org/10.1016/j.apcatb.2018.03.089>.
- [144] L. Zhang, X. Wang, C. Chen, X. Zou, W. Ding, X. Lu, Dry reforming of methane to syngas over lanthanum-modified mesoporous nickel aluminate/γ-alumina nanocomposites by one-pot synthesis, *Int. J. Hydrogen Energy.* 42 (2017) 11333–11345. <https://doi.org/10.1016/j.ijhydene.2017.03.140>.
- [145] M.S. Fan, A.Z. Abdullah, S. Bhatia, Catalytic technology for carbon dioxide reforming of methane to synthesis gas, *ChemCatChem.* 1 (2009) 192–208. <https://doi.org/10.1002/cctc.200900025>.
- [146] H.S. Bengaard, J.K. Nørskov, J. Sehested, B.S. Clausen, L.P. Nielsen, A.M. Molenbroek, J.R. Rostrup-Nielsen, Steam reforming and graphite formation on Ni catalysts, *J. Catal.* 209 (2002) 365–384. <https://doi.org/10.1006/jcat.2002.3579>.
- [147] C. Montero, A. Ochoa, P. Castaño, J. Bilbao, A.G. Gayubo, Monitoring Ni⁰ and coke evolution during the deactivation of a Ni/La₂O₃-αAl₂O₃ catalyst in ethanol steam reforming in a fluidized bed, *J. Catal.* 331 (2015) 181–192. <https://doi.org/10.1016/j.jcat.2015.08.005>.
- [148] Å. Björkman, Thermische Klärschlammbehandlung, *Schweizerische Zeitschrift Für Hydrol.* 31 (1969) 632–645. <https://doi.org/10.1007/BF02543692>.
- [149] J.H. Lehman, M. Terrones, E. Mansfield, K.E. Hurst, V. Meunier, Evaluating the characteristics of multiwall carbon nanotubes, *Carbon* N. Y. 49 (2011) 2581–2602. <https://doi.org/10.1016/j.carbon.2011.03.028>.
- [150] D. Zhao, J. Feng, Q. Huo, N. Melosh, G.H. Fredrickson, B.F. Chmelka, G.D. Stucky, Triblock copolymer syntheses of mesoporous silica with periodic 50 to 300 angstrom pores, *Science* (80-.). 279 (1998) 548–552. <https://doi.org/10.1126/science.279.5350.548>.
- [151] E. Casas, B. Paredes, R. Van Grieken, J.M. Escola, (nBuCp)₂ZrCl₂ supported over mesoporous

propyl sulfonic silica-alumina: A highly active heterogeneous catalyst for ethylene polymerization, *Catal. Sci. Technol.* 3 (2013) 2565–2570. <https://doi.org/10.1039/c3cy00461a>.

- [152] Z. Xue, H. Shang, Z. Zhang, C. Xiong, C. Lu, G. An, Efficient synthesis of polyoxymethylene dimethyl ethers on Al-SBA-15 catalysts with different Si/Al ratios and pore sizes, *Energy and Fuels.* 31 (2017) 279–286. <https://doi.org/10.1021/acs.energyfuels.6b02255>.
- [153] A.S. Cattaneo, C. Ferrara, D.C. Villa, S. Angioni, C. Milanese, D. Capsoni, S. Grandi, P. Mustarelli, V. Allodi, G. Mariotto, S. Brutti, E. Quartarone, SBA-15 mesoporous silica highly functionalized with propylsulfonic pendants: A thorough physico-chemical characterization, *Microporous Mesoporous Mater.* 219 (2016) 219–229. <https://doi.org/10.1016/j.micromeso.2015.08.011>.
- [154] K. Möller, J. Kobler, T. Bein, Colloidal suspensions of mercapto-functionalized nanosized mesoporous silica, *J. Mater. Chem.* 17 (2007) 624–631. <https://doi.org/10.1039/b611931j>.
- [155] H. Okabayashi, K. Izawa, T. Yamamoto, H. Masuda, E. Nishio, C.J. O'Connor, Surface structure of silica gel reacted with 3-mercaptopropyltriethoxysilane and 3-aminopropyltriethoxysilane: Formation of the S-S bridge structure and its characterization by Raman scattering and diffuse reflectance Fourier transform spectroscopic study, *Colloid Polym. Sci.* 280 (2002) 135–145. <https://doi.org/10.1007/s003960100585>.
- [156] K. Wilson, A.F. Lee, D.J. Macquarrie, J.H. Clark, Structure and reactivity of sol-gel sulphonic acid silicas, *Appl. Catal. A Gen.* 228 (2002) 127–133. [https://doi.org/10.1016/S0926-860X\(01\)00956-5](https://doi.org/10.1016/S0926-860X(01)00956-5).
- [157] N.A.S. Ramli, N.A.S. Amin, Thermo-kinetic assessment of glucose decomposition to 5-hydroxymethyl furfural and levulinic acid over acidic functionalized ionic liquid, *Chem. Eng. J.* 335 (2018) 221–230. <https://doi.org/10.1016/j.cej.2017.10.112>.
- [158] C. Tempelman, U. Jacobs, T. Hut, E. Pereira de Pina, M. van Munster, N. Cherkasov, V. Degirmenci, Sn exchanged acidic ion exchange resin for the stable and continuous production of 5-HMF from glucose at low temperature, *Appl. Catal. A Gen.* 588 (2019) 117267. <https://doi.org/10.1016/j.apcata.2019.117267>.
- [159] C. Morterra, G. Cerrato, G. Meligrana, Revisiting the use of 2,6-dimethylpyridine adsorption as a probe for the acidic properties of metal oxides, *Langmuir.* 17 (2001) 7053–7060. <https://doi.org/10.1021/la010707e>.
- [160] T. Onfroy, G. Clet, M. Houalla, Quantitative IR characterization of the acidity of various oxide catalysts, *Microporous Mesoporous Mater.* 82 (2005) 99–104. <https://doi.org/10.1016/j.micromeso.2005.02.020>.
- [161] C. Pirez, A.F. Lee, J.C. Manayil, C.M.A. Parlett, K. Wilson, Hydrothermal saline promoted grafting: A route to sulfonic acid SBA-15 silica with ultra-high acid site loading for biodiesel synthesis, *Green*

Chem. 16 (2014) 4506–4509. <https://doi.org/10.1039/c4gc01139b>.

- [162] D. Zhao, Q. Huo, J. Feng, B.F. Chmelka, G.D. Stucky, Nonionic triblock and star diblock copolymer and oligomeric surfactant syntheses of highly ordered, hydrothermally stable, mesoporous silica structures, *J. Am. Chem. Soc.* 120 (1998) 6024–6036. <https://doi.org/10.1021/ja974025i>.
- [163] C.A. Emeis, Determination of integrated molar extinction coefficients for infrared absorption bands of pyridine adsorbed on solid acid catalysts, *J. Catal.* (1993). <https://doi.org/10.1006/jcat.1993.1145>.
- [164] Z. Yang, W. Cai, J. Chou, Z. Cai, W. Jin, J. Chen, Z. Xiong, X. Ru, Q. Xia, Hydrothermal synthesis of plugged micro/mesoporous Al-SBA-15 from spent fluid catalytic cracking catalyst, *Mater. Chem. Phys.* 222 (2019) 227–229. <https://doi.org/10.1016/j.matchemphys.2018.10.026>.
- [165] A.J.J. Koekkoek, J.A.R. Van Veen, P.B. Gerttisen, P. Giltay, P.C.M.M. Magusin, E.J.M. Hensen, Brønsted acidity of Al/SBA-15, *Microporous Mesoporous Mater.* 151 (2012) 34–43. <https://doi.org/10.1016/j.micromeso.2011.11.019>.
- [166] V. Meynen, P. Cool, E.F. Vansant, Verified syntheses of mesoporous materials, *Microporous Mesoporous Mater.* 125 (2009) 170–223. <https://doi.org/10.1016/j.micromeso.2009.03.046>.
- [167] E.M. Johansson, A. Galarneau, H. Cambon, F. Di Renzo, R. Ryoo, M. Choi, F. Fajula, D. Zhao, J. Sun, Q. Li, G.D. Stucky, S. Barbara, R. van Grieken, J.M. Escola, J. Moreno, R. Rodríguez, J. Xu, T. Chen, J.-K. Shang, K.-Z. Long, Y.-X. Li, J. Wang, H. Ge, W. Bao, E.M. Björk, D. Zhang, A. Duan, Z. Zhao, X. Wang, G. Jiang, J. Liu, C. Wang, M. Jin, M. Kruk, M. Jaroniec, C.H. Ko, R. Ryoo, Controlling the Pore Size and Morphology of Mesoporous Silica, *New J. Chem.* (2015). <https://doi.org/10.1016/j.cej.2009.07.016>.
- [168] A. Vinu, V. Murugesan, M. Hartmann, Adsorption of lysozyme over mesoporous molecular sieves MCM-41 and SBA-15: Influence of pH and aluminum incorporation, *J. Phys. Chem. B.* 108 (2004) 7323–7330. <https://doi.org/10.1021/jp037303a>.
- [169] A.A. Gurinov, Y.A. Rozhkova, A. Zukał, J. Čejka, I.G. Shenderovich, Mutable Lewis and Brønsted acidity of aluminated SBA-15 as revealed by NMR of adsorbed pyridine-15N, *Langmuir.* 27 (2011) 12115–12123. <https://doi.org/10.1021/la2017566>.
- [170] B. Dragoi, E. Dumitriu, C. Guimon, A. Auroux, Acidic and adsorptive properties of SBA-15 modified by aluminum incorporation, *Microporous Mesoporous Mater.* 121 (2009) 7–17. <https://doi.org/10.1016/j.micromeso.2008.12.023>.
- [171] B. Girisuta, L.P.B.M. Janssen, H.J. Heeres, Green chemicals: A kinetic study on the conversion of glucose to levulinic acid, *Chem. Eng. Res. Des.* 84 (2006) 339–349. <https://doi.org/10.1205/cherd05038>.

Appendix

A1. Supplementary information of Chapter 3

In order to investigate if ethanol is the only reducing agent and that support doesn't contribute to the reduction of the active phase, blank test with pure support has been performed. (Spectrum is reported in Figure 4.3 in the Chapter 4)

At room temperature, ethanol is detected on CeO₂ surface as:

- Molecularly undissociated ethanol identified by $\delta(\text{OH})$ 1261 cm⁻¹
- Ethoxy whose presence is corroborated by $\nu_{\text{as}}(\text{CH}_3)$ 2969, $\nu(\text{CH}_2)$ 2927, $\nu_{\text{s}}(\text{CH}_3)$ 2877, $\nu(\text{CO})$ monodentate 1096 and, $\nu(\text{CO})$ bidentate 1054 cm⁻¹.
- Acetate whose identificative bands can be seen at 1562 $\nu_{\text{as}}(\text{OCO})$, 1423 $\nu_{\text{s}}(\text{OCO})$ 1340 $\delta(\text{CH}_3)$
- The band at 1017 cm⁻¹ assignable to bidentate carbonates points out carbonate presence.

At 150 °C a new small band is detected at 1659 cm⁻¹ assigned to crotonaldehyde $\nu(\text{CO})$. Crotonaldehyde band disappears at 350 °C while acetate ones vanish at 400 °C. The results reported are in good agreement with the literature. Acetate, carbonates and, crotonaldehyde were not detected at low temperature on NiO supported samples, corroborating a different reactivity towards ethanol activation on the surface. Moreover, the spectra baseline at high temperature (over 400 °C) is not drastically changed as in the case of NiO supported samples. Other differences can be found in the MS results. In fact ethanol start to be consumed, by the reaction, around 330 °C while in presence of NiO the reaction start at lower temperature (250 °C). Since H₂ is detected from 200 °C, it is possible to hypothesize that CeO₂ tends to adsorb H₂, releasing it at higher temperatures. The slope of H₂ trend sensibly increase after 350 °C according to the ethanol trend and the beginning of the reaction. Moreover, it is clear that among the main product with CeO₂ there is ethylene that was not clearly detected using the other two catalysts. Anyway, it is important to notice that this small amount of H₂ released before the H₂ consumption is not detected in the experiments carried out with NiO supported samples. This behaviour supports the hypothesis that ethanol itself is the reducing agent at low temperature since when it is oxidized to acetaldehyde some NiO can be reduced to Ni. Despite all, it is not possible to exclude the participation of H₂ in NiO reduction at high temperature.

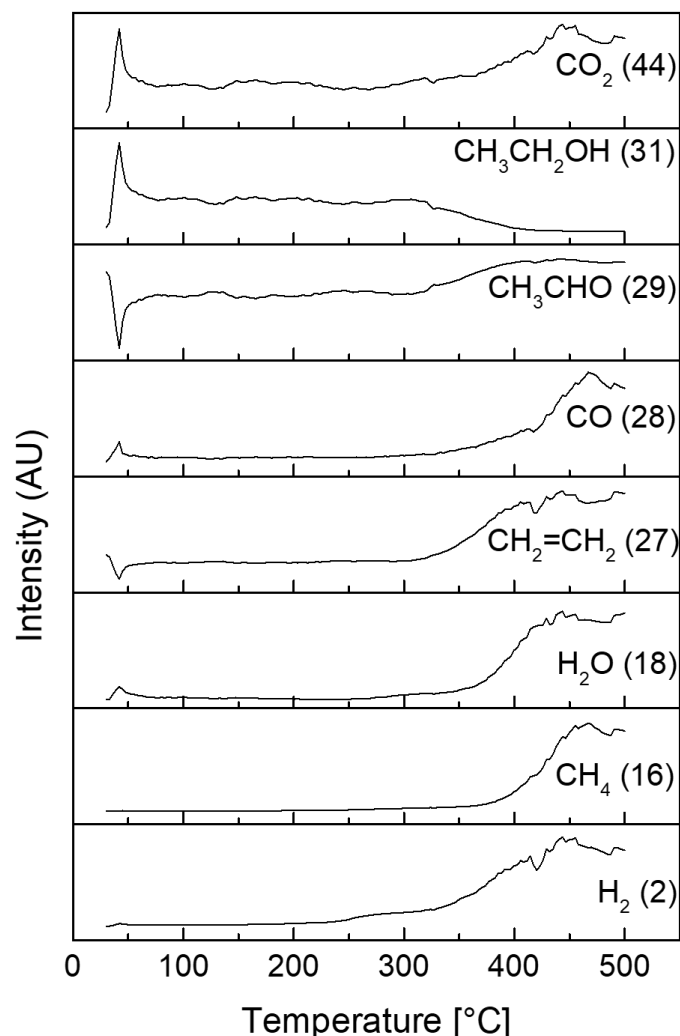


Figure A.1 Mass analysis of CeO_2 feeding ethanol.

Considering Ni-Ce and co-Ni-La-Ce samples, MS analysis of m/z product were monitoring in order to understand the reaction pathway involved. The results for both samples are reported in Figure A.2. As for the DRIFTS tests, the samples did not show any significant difference since they share the same reaction intermediates. The mass signal at temperature lower than $200\text{ }^\circ\text{C}$ were dominated by ethanol since it was continuously fed; this complicates interpretation of m/s signals at $T < 200^\circ\text{C}$. The acetaldehyde signal presented a descending slope that might be attributed to its surface adsorption since on both samples its infrared transitions were appreciated. At low temperature, H_2O signal showed the same trend of ethanol, its production probably was not due to ethanol dehydration to ethylene but to the interaction of the hydrogen released by the ethanol (adsorbed as ethoxy) with the

catalyst terminal OH. The reaction started at 200 °C as clearly shown by the ethanol drop down alongside the raising slope of acetaldehyde, CO, CH₄ and H₂. The H₂O diminution allowed us to hypothesize that the ethanol steam reforming reaction ($\text{CH}_3\text{CH}_2\text{OH} + 3 \text{H}_2\text{O} \rightleftharpoons 6 \text{H}_2 + 2 \text{CO}_2$ and $\text{CH}_3\text{CH}_2\text{OH} + \text{H}_2\text{O} \rightleftharpoons 4 \text{H}_2 + 2 \text{CO}$) might occur along with acetaldehyde steam reforming ($\text{CH}_3\text{CHO} + 3 \text{H}_2\text{O} \rightleftharpoons 5 \text{H}_2 + 2 \text{CO}_2$ and $\text{CH}_3\text{CHO} + \text{H}_2\text{O} \rightleftharpoons 3 \text{H}_2 + 2 \text{CO}$). Anyway, it was not possible to exclude the contribution of some acetaldehyde and ethanol decomposition reactions. At 250 °C, a maximum for acetaldehyde, H₂, CO, and CH₄ was detected, this observation was in good agreement with the DRIFTS analysis. In fact, at this temperature the acetaldehyde transitions vanished while the gas phase transitions of CO and CH₄ were detected. The IR analysis showed that some CO₂ was produced along with the other two products. It is possible that CO₂ was not detected by MS as soon as the others since it might have been physisorbed on the catalyst surface, since its slope was starting to raise at this temperature. A contribution to CH₄ trend might come from acetates oxidation to carbonates, reaction 7 in Figure A.3. It is that some ethylene traces were produced since its slope slightly decreased from 200 °C to 500 °C but it was not possible to hypothesize whether or not its production really started, due to the strong influence of the ethanol amount on the ethylene trend. At 300 °C, CH₄, H₂O and CO slopes decreased while the H₂ and CO₂ ones increased, this might suggest that methane steam reforming ($\text{CH}_4 + 2 \text{H}_2\text{O} \rightleftharpoons 4 \text{H}_2 + \text{CO}_2$) and water gas shift ($\text{CO} + \text{H}_2\text{O} \rightleftharpoons \text{CO}_2 + \text{H}_2$) started at this temperature. Anyway, it is not possible to exclude some contribution of the Boudouard reaction ($2 \text{CO} \rightleftharpoons \text{CO}_2 + \text{C}$). The surface reactions that started to contribute at this temperature were reactions 6, 7, 8, 9, 10 showed in Figure A.3. Till 400 °C, all the aforementioned reactions might continue to proceed simultaneously. From this temperature on, it is possible that some other side reactions started, leading to H₂ consumed ($\text{CO}_2 + 4 \text{H}_2 \rightleftharpoons \text{CH}_4 + 2 \text{H}_2\text{O}$ and $\text{CO}_2 + 2 \text{H}_2 \rightleftharpoons \text{C} + 2 \text{H}_2\text{O}$), as suggested by the diminution of H₂ and CO₂ slopes.

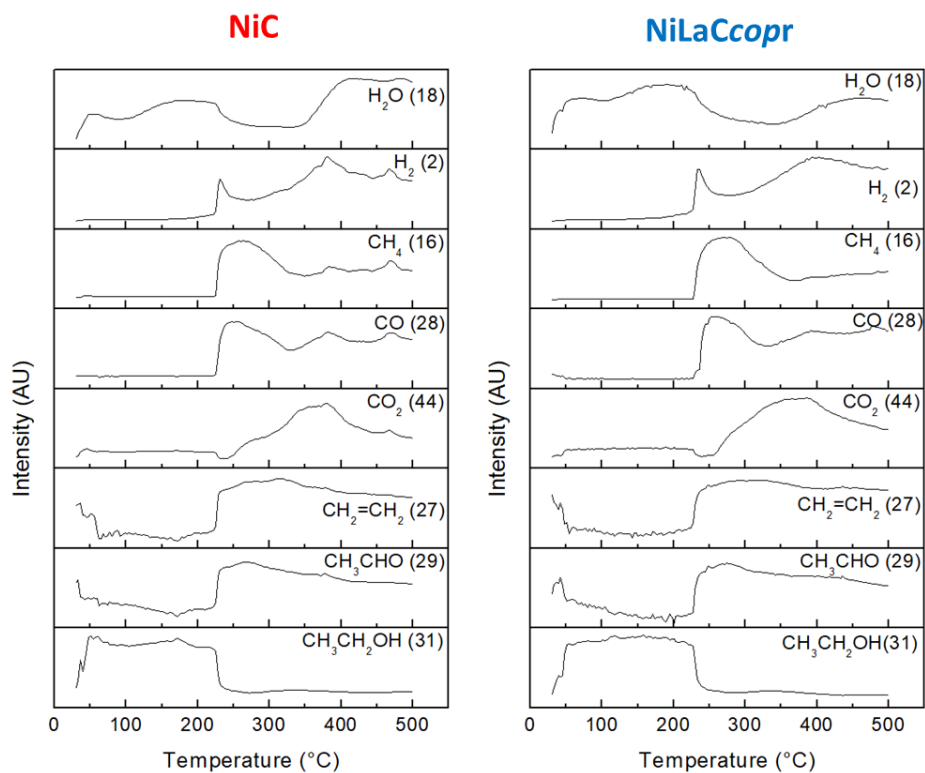


Figure A.2 MS analysis of NiC and NiLaCcopr feeding ethanol

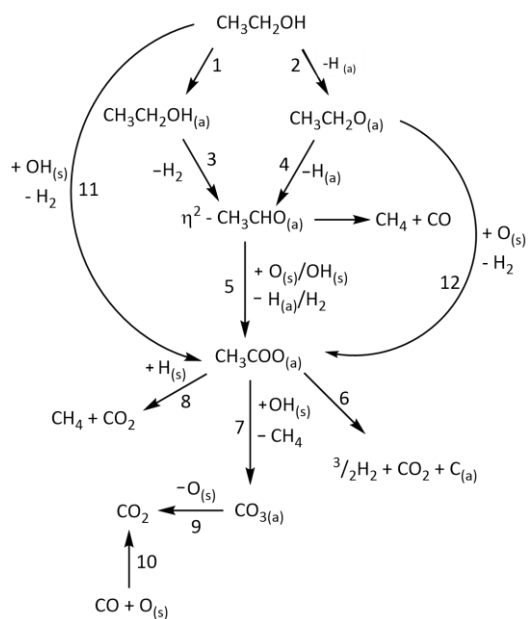


Figure A.3 Hypothesized surface pathways

A2. Supplementary information of Chapter 4

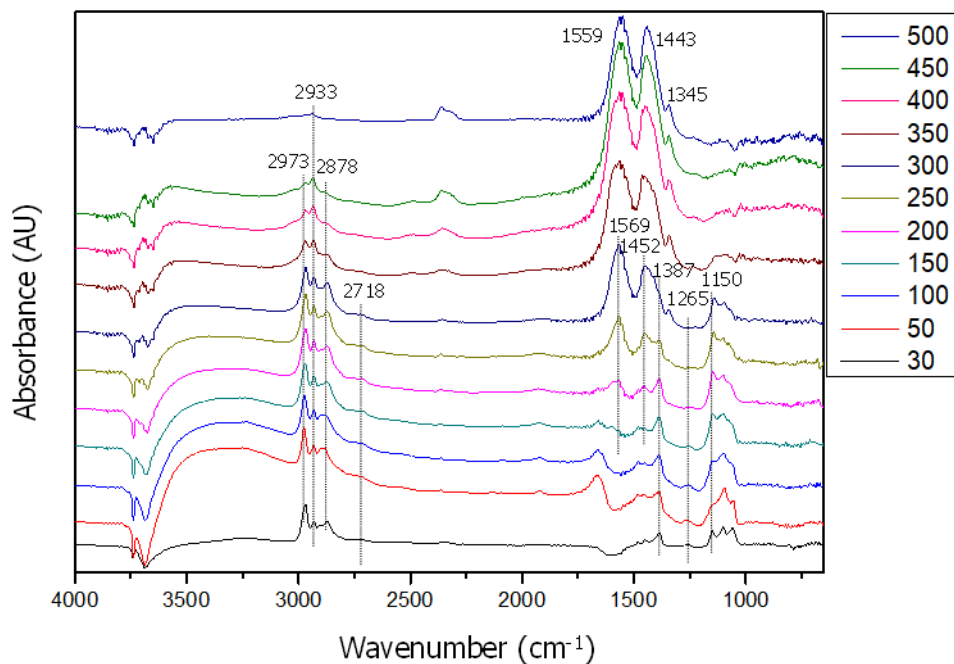


Figure A.4 DRIFTS feeding EtOH-H₂O mixture on NiLaZcopr.

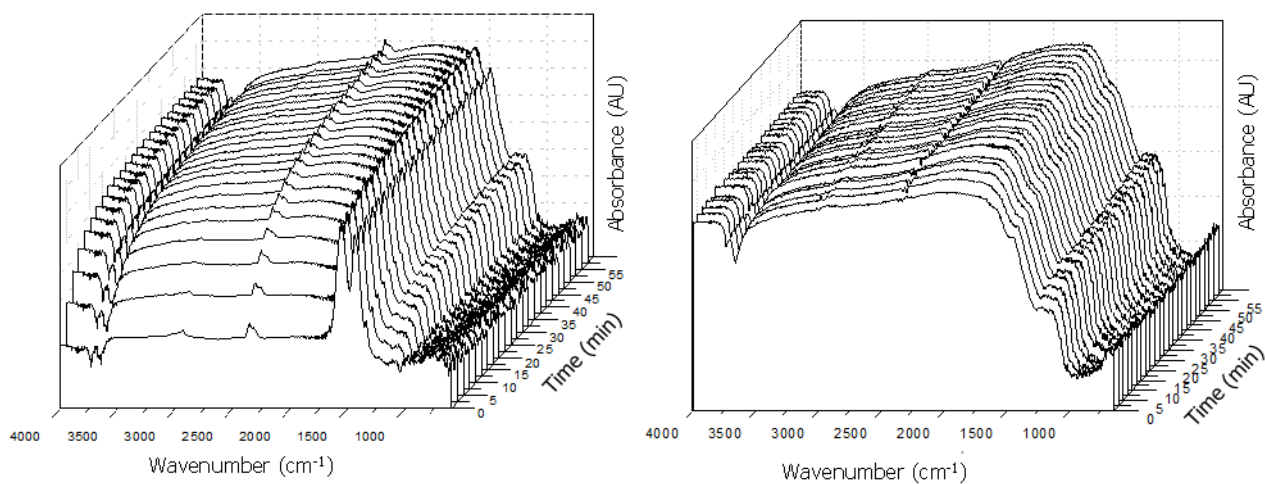


Figure A.5 DRIFTS at 500 $^{\circ}\text{C}$ feeding EtOH/H₂O (left) and EtOH (right) on NiLaZcopr catalyst.

Curriculum Vitae

Born in 1992, I graduated *cum laude* in Sustainable Chemistry and Technologies at Ca' Foscari University Venice in 2014, with a thesis regarding the preparation of hybrid matrixes for drug delivery systems. At the same University, I got the Master's Degree in Sustainable Chemistry and Technologies, curriculum Industrial Chemistry (110/110 cum laude) in 2016 with a thesis concerning the development of nanostructured catalysts based on nickel for hydrogen production. I won the best master thesis in Industrial Chemistry award 2017 by Industrial Division of Italian Chemical Society.

Since November 2017 I am working as PhD student at the University of Trieste. My work is focused on the development of heterogeneous catalysts for biomass valorisation. In particular, I'm working on nickel-based catalyst materials, their characterisation and their activity in ethanol steam reforming and methane dry reforming processes. Regarding this topic, I spent 3 months in Madrid (April-July 2018) at the Institute of Catalysis and Petrochemistry. Since the second year of PhD, I've been facing a new project concerning winery by-products valorisation to produce bio-based platform chemicals. In particular, I'm developing grafting strategies for the preparation of acid mesoporous silica. In this contest, I took part in an exchange program at Åbo Akademi University in Turku (February-April 2019) to deeply investigate these acid catalysts for LA production through glucose hydrolysis

My research activity is documented by some papers published on peer-reviewed international journals and national and international congresses memories.

I'm currently working in the Basic Research Department of R&D Division at Casale S.A.

List of publications and conference presentations based on this thesis

Chapter 2

Conference presentation

- C. Pizzolitto, M. Signoretto, F. Menegazzo, V. Cortés Corberán, “*Microemulsion vs. Precipitation: Selecting the support synthesis of nickel-ceria based catalysts for ethanol steam reforming*” Europacat 2019 (Aachen, 18-23 August 2019), poster communication, presenting author V. Cortés Corberán.

Chapter 3

Publications

- C. Pizzolitto, F. Menegazzo, E. Ghedini, G. Innocenti, A. Di Michele, G. Cruciani, F. Cavani, M. Signoretto, “*Increase of Ceria Redox Ability by Lanthanum Addition on Ni Based Catalysts for Hydrogen Production*”, ACS Sustainable Chem. Eng. 6 (2018) 13867-13876.

Conference presentation

- C. Pizzolitto; “*Development of nanostructured nickel based catalysts for hydrogen production*” proceeding of Congresso Nazionale della Società Chimica Italiana 2017 (Paestum, 10-14 Settembre 2017), oral communication, presenting author Cristina Pizzolitto.
- C. Pizzolitto, F. Menegazzo, M. Signoretto, G. Cruciani, “*Ethanol steam reforming process: lanthanum oxide effect in ceria and zirconia based catalysts*”, proceeding of National congress of Italian chemical society young 2017 (Milano Marittima, 13-15 November 2017), oral communication, presenting author Cristina Pizzolitto.
- C. Pizzolitto, F. Menegazzo, E. Ghedini, G. Innocenti, A. di Michele, G. Cruciani, F. Cavani, M. Signoretto, “*La₂O₃ EFFECT ON Ni/CeO₂ CATALYTIC PROPERTIES FOR DIR-SOFC APPLICATION*”, proceeding of EFCATS school on catalysis 2018 (Praga, 24-27 June 2018), oral communication, presenting author Cristina Pizzolitto.

Chapter 4

Publication

- C. Pizzolitto, F. Menegazzo, E. Ghedini, G. Innocenti, A. Di Michele, M. Mattarelli, G. Cruciani, F. Cavani, M. Signoretto* *“Limiting Coke deactivation of Ni-ZrO₂ in ethanol steam reforming by promoting effect of lanthanum” submitted.*

Conference presentations

- C. Pizzolitto, M. Signoretto, F. Menegazzo, G. Cruciani, A. D. Michele; *“Influence of lanthanum oxide on activity and stability of Ni/CeO₂ and Ni/ZrO₂ catalyst for hydrogen production”* proceeding of Europacat 2017 (Florence, 27-31 August 2017) poster communication, presenting author Cristina Pizzolitto.

Chapter 5

Publication

- C. Pizzolitto, E. Ghedini, F. Menegazzo, M. Signoretto, A. Giordana, G. Cerrato, G. Cruciani, *“Effect of grafting solvent in the optimisation of SBA-15 acidity for levulinic acid production”*, Catal. Today, doi.org/10.1016/j.cattod.2019.11.012, *in press.*

Conference presentations

- C. Pizzolitto, M. Signoretto, F. Menegazzo, E. Ghedini, A. Giordana, G. Cerrato, *“Optimization of grafting SBA-15 synthesis for Levulinic acid production”* proceeding of Merck and Elsevier Young Chemical Symposium, (Rimini, 19-21 November 2018), oral communication, presenting author Cristina Pizzolitto.
- C. Pizzolitto, E. Ghedini, F. Menegazzo, M. Signoretto, A. Giordana, G. Cerrato, G. Cruciani, *“Effect of grafting solvent in the optimisation of SBA-15 acidity for levulinic acid production”* proceeding of Jointly meeting of the AIZ-CIS-GIC, (Amantea, 11-14 June 2019), oral communication, presenting author Cristina Pizzolitto.
- G. Bortolomiol, S.Taghavi, E. Ghedini, C. Pizzolitto, G. Cruciani, F. Menegazzo, M. Signoretto, *“Development of mesoporous catalysts for valuable chemical production from*

- glucose*” proceeding of Jointly meeting of the AIZ-CIS-GIC, (Amantea, 11-14 June 2019), poster communication, presenting author S. Taghavi.
- C. Pizzolitto, M. Signoretto, F. Menegazzo, E. Ghedini, G. Cerrato, “*Implementation of SBA-15 acid properties for levulinic acid production*” proceeding of Making Business with Green Chemistry and Sustainable Energy, (Sarteano, 22-27 July 2019), oral communication, presenting author Cristina Pizzolitto.

Chapter 6

Conference presentation

- C. Pizzolitto, M- Signoretto, F. Menegazzo, G. Cruciani, M. Peurla, K. Eränen, A. Aho, N. Kumar, D. Y. Murzin, T. Salmi, “ *Influence of alumina content on acidic and hydrothermal properties of SBA-15 as a catalyst for levulinic acid production*” proceeding of CatBior V 2019 (Turku, 23-27 September 2019), poster communication, presenting author N. Kumar.

Other publications

- F. Menegazzo, C. Pizzolitto, D. Zanardo, M. Signoretto, C. Buyschaert, G. Bényb, A. D. Michele, *Hydrogen production by ethanol steam reforming on Ni-based catalysts: effect of the support and of CaO and Au doping*, Chemistry Select, 2 (2017) 9523-9531.
- F. Menegazzo, C. Pizzolitto, E. Ghedini, A. Di Michele, G. Cruciani, M. Signoretto, *Development of La doped Ni/CeO₂ for CH₄/CO₂ reforming*, C, 4 (2018) 60.
- C. Pizzolitto, E. Pupulin, F. Menegazzo, E. Ghedini, A. Di Michele, M. Mattarelli, G. Cruciani, M. Signoretto, *Nickel based catalysts for Methane Dry Reforming: effect of supports on catalytic activity and stability*, International Journal of Hydrogen Energy, 44 (2019) 28065-28076.
